

2-9-2010

Optical control and quantum information processing with ultracold alkaline-earth-like atoms

Iris Evelyn Nicole Reichenbach

Follow this and additional works at: https://digitalrepository.unm.edu/phyc_etds

Recommended Citation

Reichenbach, Iris Evelyn Nicole. "Optical control and quantum information processing with ultracold alkaline-earth-like atoms." (2010). https://digitalrepository.unm.edu/phyc_etds/57

This Dissertation is brought to you for free and open access by the Electronic Theses and Dissertations at UNM Digital Repository. It has been accepted for inclusion in Physics & Astronomy ETDs by an authorized administrator of UNM Digital Repository. For more information, please contact disc@unm.edu.

Iris Reichenbach

Candidate

Physics and Astronomy

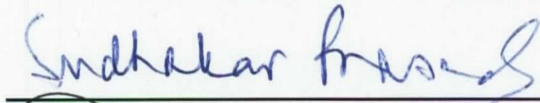
Department

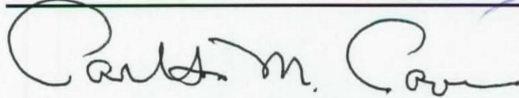
This dissertation is approved, and it is acceptable in quality and form for publication:


Approved by the Dissertation Committee:



, Chairperson









Optical Control and Quantum Information Processing with Ultracold Alkaline-Earth-like Atoms

by

Iris Reichenbach

Vordiplom, Julius Maximilians Universität Würzburg, 2002
M.S., Physics, University of New Mexico, 2005

DISSERTATION

Submitted in Partial Fulfillment of the
Requirements for the Degree of

Doctor of Philosophy
Physics

The University of New Mexico

Albuquerque, New Mexico

December, 2009

©2009, Iris Reichenbach

Dedication

To Birk

Acknowledgments

First and foremost, many thanks to my advisor Ivan Deutsch, who introduced me to the fascinating field of quantum optics. His enthusiasm and support has helped me to stay motivated and has helped me to develop the skills and confidence needed to be a scientist.

My thanks also go to Paul Julienne and Eite Tiesinga for teaching me much about collisional and atomic physics.

I also want to thank René Stock who has taught me quite a bit of scattering theory and who, together with Shohini Ghose always had valuable advise for me. Furthermore, many thanks to the whole Information Physics Group for many interesting discussions over the years, some of which were actually about physics. I made many friends on my way and I want to thank all of you. Most importantly, I want to thank my husband Birk for all his support. Thank you for always being there when I need you.

Optical Control and Quantum Information Processing with Ultracold Alkaline-Earth-like Atoms

by

Iris Reichenbach

ABSTRACT OF DISSERTATION

Submitted in Partial Fulfillment of the
Requirements for the Degree of

Doctor of Philosophy
Physics

The University of New Mexico
Albuquerque, New Mexico

December, 2009

Optical Control and Quantum Information Processing with Ultracold Alkaline-Earth-like Atoms

by

Iris Reichenbach

Vordiplom, Julius Maximilians Universität Würzburg, 2002

M.S., Physics, University of New Mexico, 2005

PhD, Physics, University of New Mexico, 2009

Abstract

Ultracold neutral atoms in optical lattices are rich systems for the investigation of many-body physics as well as for the implementation of quantum information processing. While traditionally alkali atoms were used for this research, in recent years alkaline-earth-like atoms have attracted considerable interest. This is due to their more complex but tractable internal structure and easily accessible transitions. Furthermore, alkaline-earth-like atoms have extremely narrow $^1S \rightarrow ^3P$ intercombination transitions, which lend themselves for the implementation of next generation atomic clocks.

In this dissertation, I show that exquisite control of alkaline-earth-like atoms can be reached with optical methods, and elucidate ways to use this controllability to further different aspects of research, mainly quantum information processing. Ad-

ditionally, the control of alkaline-earth-like atoms is very interesting in many-body physics and the improvement of atomic clocks.

Since heating usually degrades the performance of quantum gates, recoiling of qubits is a necessity for the implementation of large scale quantum computers. Laser cooling has advantages over the usually used sympathetic cooling, given that it requires no additional atoms, which have to be controlled separately. However, for qubits stored in hyperfine states, as usually done in alkali atoms, laser cooling leads to optical pumping and therefore to loss of coherence. On the other hand, in the ground state, the nuclear spin of alkaline-earth-like atoms is decoupled from the electronic degrees of freedom. As I show in this dissertation, this allows for the storage of quantum information in the nuclear spin and laser cooling on the electronic degrees of freedom. The recoiling protocol suggested here consists of two steps: resolved sideband cooling on the extremely narrow $^1S_0 \rightarrow ^3P_0$ clock transition and subsequent quenching on the much shorter lived 1P_1 state. A magnetic field is used to overcome the hyperfine interaction in this excited state and thus ensures decoupling of the nuclear spin degrees of freedom during the quenching. The application of this magnetic field also allows for photon scattering on the 1P_1 state, while preserving the nuclear spin, e. g. for electronic qubit detection.

The manipulation of the scattering properties of neutral atoms is an important aspect of quantum control. In contrast to alkali atoms, whose broad linewidths cause large losses, this can be done with purely optical methods via the implementation of an optical Feshbach resonance for alkaline-earth-like atoms. Here, the scattering length resulting from the application of an optical Feshbach resonance on the $^1S_0 \rightarrow ^3P_1$ intercombination line, including hyperfine interaction and rotation is calculated for ^{171}Yb . Due to their different parities, the p-wave scattering length can be controlled independently from the s-wave scattering length, thus allowing for unprecedented control over the scattering properties of neutral atoms. Furthermore, I also show how optical Feshbach resonances in alkaline-earth-like atoms can be used

together with the underlying quantum symmetry to implement collisional gates between nuclear-spin qubits over comparatively long ranges.

Contents

List of Figures	xiii
List of Tables	xv
1 Introduction	1
1.1 Cold Atoms in Optical Lattices	4
1.2 Quantum Information Processing	6
1.3 Alkaline-Earth-like Atoms	8
1.4 Overview of Thesis	11
2 Theoretical Background	13
2.1 Scattering Theory	14
2.2 Controlled Collisions in Quantum Information Processing	19
2.3 Molecular States	22
2.3.1 Hund's Cases	25
2.3.2 Including Nuclear Spin and Hyperfine Interaction	27

<i>Contents</i>	xi
2.3.3 Molecular States for Nuclear Rotation	28
2.3.4 Transformation between Basis States	31
3 Cooling Atomic Vibration without Decohering Qubits	37
3.1 Theoretical Background	37
3.1.1 Resolved Sideband Cooling	39
3.2 Description of the Proposed Cooling Scheme	44
3.2.1 Resolved Sideband Cooling on the Clock Transition	45
3.2.2 Quenching of a Metastable State via a Rapidly Decaying State	47
3.2.3 Decoupling the Nuclear Spin from the Electronic Degrees of Freedom in the Quenching Process	51
3.3 Results	53
3.4 Fluorescence while Preserving Nuclear Spin Coherences	55
4 Optical Feshbach Resonances for ^{171}Yb	66
4.1 Background	66
4.1.1 Feshbach resonances in controlling atom-atom interactions . .	67
4.1.2 Magnetic vs. Optical Feshbach resonances	68
4.1.3 Theory of optical Feshbach resonances	70
4.2 Calculation	72
4.2.1 Ground States	72
4.2.2 Excited States	74

<i>Contents</i>	xii
4.2.3 Channel Bases	76
4.3 Results	79
4.3.1 Selective Change of a for P-waves and S-waves	79
4.3.2 Purely Long-Range States	83
4.3.3 Excited-State Spectrum	86
4.3.4 Scattering Length	90
4.4 Application to QIP	93
4.5 Conclusions	96
5 Summary and Outlook	101
Appendices	107
A Programs	108
A.1 Calculation of the Breit-Rabi spectrum	108
A.2 Inclusion of the quadrupole part for Sr	117
A.3 Calculation of the multichannel Hamiltonian	124
A.4 Determination of the optically induced scattering length	138
References	149

List of Figures

2.1	Implementation of a state dependent controlled collision.	20
2.2	Optical lattice for alkaline-earth-like atoms	33
2.3	Schematics of Hund's case c) coupling	34
2.4	Schematics of Hund's case e) coupling	35
2.5	Schematics of Hund's case a) coupling	36
2.6	The classical motion of a symmetric top.	36
3.1	Schematics of resolved sideband cooling.	60
3.2	Schematic cooling and readout level-diagram for ^{171}Yb	61
3.3	Zeeman diagram of the 1P_1 manifold.	62
3.4	Field dependent expansion coefficients c_q for the m_f state of ^{171}Yb .	63
3.5	Fidelity for transfer of coherence for the proposed cooling scheme. .	64
3.6	Scattering rates for alternative cooling scheme.	65
4.1	Schematics of a Feshbach resonance.	67
4.2	S-wave ground state wave functions	72

4.3	The adiabatic potentials for s-wave collisions.	80
4.4	The adiabatic potentials for p-wave collisions.	81
4.5	Adiabatic purely long-range potentials for s-waves	83
4.6	Adiabatic purely long-range potentials for p-waves	84
4.7	Purely-long range states for p-waves	85
4.8	S-wave spectrum for ^{171}Yb	87
4.9	P-wave spectrum for ^{171}Yb	88
4.10	Multi-channel states for s-waves	91
4.11	Scattering length for s-wave optical Feshbach resonances	92
4.12	The optical Feshbach resonance leading to nuclear spin exchange. . .	99
4.13	The fidelity of a \sqrt{SWAP} gate	100

List of Tables

1.1	The stable isotopes of Yb and Sr	9
1.2	List of publications	12
4.1	The $ \epsilon\rangle$ basis for s-wave states	81
4.2	The $ \epsilon\rangle$ basis for p-wave states	82
4.3	Excited molecular bound states and resonance properties for s-waves	89
4.4	P-wave accessible excited molecular bound states.	98

Chapter 1

Introduction

Over the last decades, several different areas of research have driven a renewal in atomic, molecular and optical (AMO) physics. The quest for ever more accurate time standards caused investigations into improving the coherences of atoms for the use in atomic clocks, the advent of laser cooling and trapping made exquisite control over the states of atoms possible, and the prediction of the advantages of quantum information processing over classical information processing have spurred even more research on the coherent control of quantum systems. Due to the improvements in these interdependent areas of basic research, we have now excellent control over the positions, internal states and interactions of single atoms as well as of many-body states.

While measurement of time was important for practical purposes as well as for social and cultural reasons throughout human history, its relevance and the required accuracy has increased dramatically in the last centuries. With the advent of the industrial revolution, traveling times decreased and the communication over wide distances became possible, thus requiring a reliable standard of time. But even then, as during all of human history, time was measured with the help of astronomical observations. However, in the last century this way of measuring time was neither

practical nor accurate enough, given the further acceleration of our society and the technical progress that required more and more accurate timekeeping. This led to the development of atomic clocks, in which the natural oscillation frequency of atoms is used to measure time, which has several advantages over earlier methods. Since all atoms of a given isotope have the exact same oscillation frequency, atomic clocks are a much more universal time standard than other measurements. Furthermore, astronomical observations generally have a low frequency, requiring the division of one oscillation period, while the much higher frequency of atomic transitions merely requires counting of oscillations, which is much easier. These advantages lead to the adoption of the oscillation frequency of Cesium as international time standard in 1967, as well as to the redefinition of the meter in terms of the so defined second and the speed of light, c . Modern Cesium fountain clocks have a fractional instability, that is the error of the clock frequency divided by the frequency of the clock, of $\sigma = 1 \times 10^{-14} T^{-1/2}$ [1]. Generally, the fractional instability of an atomic clock is given by

$$\sigma = \frac{\Delta\nu}{\nu} \frac{C}{2\pi\sqrt{NT}}, \quad (1.1)$$

where C is a constant of order unity, T is the interrogation time, N is the number of interrogated atoms, and $\Delta\nu$ is the linewidth of the clock transition with frequency ν [2, 1]. This shows that the fractional instability can be decreased by interrogating more atoms or by choosing a transition with a longer lifetime or higher frequency. To take advantage of an increase of the number of atoms N or the interrogation time T , however, these atoms have to be coherent. Thus, the system has to be very well isolated from the environment, e.g. stray magnetic or electric fields as well as electromagnetic radiation have to be suppressed. Furthermore, to avoid effects due to the motion of the atoms, they have to be cooled to very low temperatures and/or tightly confined to traps.

During the 1980's, laser cooling and trapping of atoms was developed, which is continuing to have wide implications for several other fields of physics. Due to

the development of optical molasses, that is counterpropagating laser beams that exert a drag on atoms, by Chu and Hollberg in 1985, neutral atoms could be cooled to very low temperatures for the first time. A closely related technique, Sisyphus cooling, which was accidentally discovered in molasses experiments and theoretically explained in 1989 by Dalibard and Cohen-Tannoudji, makes it possible to cool neutral atoms to temperatures below the Doppler limit, which was before considered to be the absolute limit of laser cooling. Furthermore, the development of magneto-optical traps by Chu in 1987 made it first possible to trap these ultracold atoms with laser light. Additionally, a consequence of optical molasses and Sisyphus cooling is the realization of optical lattices, in which atoms are trapped in a periodic potential created by standing waves from counterpropagating laser beams, which was first realized in 1992 by Jessen *et al.*. An in-depth account of these achievements can be found in the Nobel lectures by Chu [3], Cohen-Tannoudji [4] and Phillips [5] from 1998, and references therein.

Cold atoms trapped in optical traps show coherences over long times and large distances, and allow for the control of their interactions, thus furthering atomic clocks, but also allowing for other basic research, e. g. the exploration quantum phase transitions and many-body effects. The goal of this thesis is to contribute to this young and rapidly developing field, by exploring possibilities of enhancing this control and applying it to the implementation of quantum information processing (QIP), another rapidly emerging field which harnesses the existence of superpositions and long range entanglement to process information more rapidly than possible with purely classical methods, as was shown in 1985 by D. Deutsch [6].

Alkaline-earth atoms are especially well suited for several of these applications, due to their interesting properties, e.g. the existence of narrow intercombination transitions. One of these transitions, the so-called clock transition, is particularly suitable for the use in atomic clocks, due to its narrow linewidth on the order of tens of mHz, and its oscillation frequency in the optical range. Thus, the quality factor

$Q = \nu/\Delta\nu$ of this transition is very high, promising a clock with very low fractional instability, as can be seen from (1.1). For the implementation of this clock, alkaline-earth atoms are trapped in an optical lattice and the clock transition is interrogated, allowing for the most accurate clock with neutral atoms to date. Considering the fact that it is possible to increase the number of atoms trapped in the optical lattice, this clock has the potential to surpass the accuracy of the most accurate clock to date, which is based on a single Hg^+ ion [7, 8]. Additionally, the absence of hyperfine interaction in the ground state allows for the storage of qubits in the nuclear spin of the atoms, rendering the qubits well isolated and causing extremely long coherence times. Furthermore, as I show in this dissertation, the narrow intercombination lines provide for excellent control over the two-body interactions that are at the heart of cold AMO physics, via optical Feshbach resonances. Additionally, I suggest a way of laser cooling alkaline-earths that enables the preservation of nuclear spin coherences and thus could prove very useful in the implementation of QIP.

In the following sections I will elucidate some background to AMO physics and QIP. In the final section of this chapter, I will give an overview over this thesis.

1.1 Cold Atoms in Optical Lattices

Over the last decades, quantum control of cold atoms has been employed in many different aspects of basic research. One major advancement was the trapping of atoms in optical lattices [9]. These artificial crystals of single atoms can be used to investigate the interactions between atoms as well as many-body effects and quantum phase transitions. Furthermore, there are several proposals for the implementation of quantum computation and quantum simulation in optical lattices [10, 11, 12, 13]. An optical lattice consists of two counterpropagating laser beams for each spatial trapping dimension, which form a superposition of standing waves with opposite

helicity given by

$$\mathbf{E}_L = \sqrt{2}E_0 (\cos(k_L z + \theta/2)\boldsymbol{\epsilon}_+ + \cos(k_L z - \theta/2)\boldsymbol{\epsilon}_-), \quad (1.2)$$

where θ is the angle between the polarizations of the laser beams, E_0 is the amplitude of the electric field of the lasers, k_L is the wavenumber of the lasers and z denotes the direction of the laser beams, here chosen to be along the z -axis. Atoms in such a standing wave experience a light shift of

$$U = -\frac{1}{4}\mathbf{E}_L^* \cdot \hat{\boldsymbol{\alpha}} \cdot \mathbf{E}_L, \quad (1.3)$$

where $\hat{\boldsymbol{\alpha}}$ is the atomic polarizability. While the atomic polarizability generally consists of a scalar, vector and second rank tensor part, for alkaline-earth-like atoms which have no hyperfine interaction in the ground state, only the scalar part is relevant. With more complicated laser configurations, it is possible to create much more complicated and controllable optical lattices, as shown by Sebby-Stradley *et al.* [14]. This allows for the lattice geometry to be changed such that atoms are moved from neighboring lattice sites into one double well or single well, where they can interact more strongly. Due to this controllability, optical lattices have proven to be an useful tool for basic research, in which many studies of scattering theory and phase transitions have been realized. Noteworthy are, among others, the Mott-insulator to superfluid transition, in which either the relative phase of the atoms or the number of atoms per lattice site are well defined, depending on the specific parameters of the optical lattice [15]. From a condensed matter physics perspective, ultracold atoms trapped in optical lattices provide an ideal system for studying tight-binding models such as the Hubbard model [9, 16, 17]. There are also interesting proposals for new applications such as quantum simulators and universal quantum computers using ultracold neutral atoms trapped in optical lattices [18].

1.2 Quantum Information Processing

Quantum computing utilizes long range entanglement and coherences to speed up some calculations compared to classical computers. To date, there are several known quantum algorithms whose large scale implementation would significantly change the world of computing, e.g. Grover's algorithm, which allows to search unordered datasets and Shor's algorithm, which allows to factor big numbers exponentially faster than any classical algorithm [6]. The latter is particularly important, since most of today's encryption is based on the fact that it is very hard to factor big numbers. However, the growing field of quantum cryptography, in which eavesdropping leads to detectable decoherence, offers the first and to date only encryption system that is safe on purely physical grounds. Another very important application of this is the simulation of quantum systems, which is hard classically, since the complexity of quantum systems scales exponentially in the size of the system, as opposed to the linear scaling in classical systems [6].

However, being based on quantum mechanical effects, quantum computing has several requirements that are much harder to fulfill than the requirements for classical information processing [6]. The first requirement for QIP is the existence of robust qubits, which will not decohere too quickly, necessitating a system that interacts only weakly with the environment. At the same time, we need the ability to subject the qubits to quantum gates, which have to be fast relative to the coherence times, to allow for many operations during the lifetime of the qubits. This requires the qubits to interact strongly with each other and with some external control field. These conditions are somewhat contradictory, since often the same interaction that allows for manipulation of qubits also causes decoherence. Additional requirements are the possibility of initialization of the qubits in a well-defined state, for which there are promising avenues for neutral atoms in optical lattices, e.g. using the Mott-insulator to superfluid transition [19] as well as readout of the qubits after the computation.

The latter also requires the ability to suddenly turn on a strong interaction with the environment. One possible realization for this is to use a fluorescence interaction on a strong line selectively on different basis states of the qubit for which I will also suggest an implementation.

Many different physical systems have been suggested for the implementation of quantum information [6], e.g. nuclear spins in NMR systems, trapped ions, superconducting qubits, solid state systems such as quantum dots as well as photons in cavities. As mentioned before, there are also several proposals for the use of neutral atoms in optical lattices [10, 11, 12, 13]. As of yet, there are no systems that accord truly scalable QIP, even though progress has been made in all of these systems.

In this thesis I will show that neutral alkaline-earth atoms in optical lattices as carriers of quantum information are a very promising system that allows to circumvent the earlier mentioned contradiction. The reason for this is that the neutral atoms in an optical lattice are well isolated from each other and from their environment. However, the rich possibilities of control and deformation of optical lattices and the possibility to significantly increase the interaction strength between neutral atoms due to Feshbach resonances, make strong interactions between selected atoms possible. Furthermore, such arrays of optical traps provide a scalable platform for storing many qubits, with parallel operations, applicable to the generation of cluster states for one-way quantum computing [20], quantum-cellular automata [11, 20], or more general quantum circuit operations [10], and fault-tolerance via topological encoding [21].

Traditionally, the research on neutral atoms for QIP and quantum control has focused on alkali atoms, owing to their good controllability after decades of research based on this system. However, recently group-II and group-II-like atoms like Yb have emerged as good candidates for the implementation of quantum information processing [13, 22]. This is due to their convenient optical transitions, and rich but tractable internal structure as well as the relative ease with which they can be

trapped and cooled. Furthermore, the distinguishing feature of alkaline-earth-like atoms is the fact that in the ground state the electron spins couple together to give an angular momentum of zero, causing the nuclear spin to be decoupled from the electronic degrees of freedom. As will be seen in this thesis, this allows for the storage of the quantum information in the nuclear spin, which in turn affords not only the optical recooling of qubits between and during the gates, but also very long coherence times in spite of strong interactions and therefore fast gates and our ability to control them with the mature tools of NMR [23].

The latter can be enhanced by the application of optical Feshbach resonances, which are possible in alkaline-earth-like atoms, due to their very narrow intercombination transitions. These optical Feshbach resonances have the potential to enhance basic research by adding another knob to the control of ultracold atoms, given their faster controllability and independence of hyperfine states compared to their magnetic equivalent.

1.3 Alkaline-Earth-like Atoms

Alkaline-earth atoms, that is, atoms in the second column of the periodic table, have two valence electrons. This is also true for Yb, the element 70, which is a rare-earth element with the ground state configuration $[Xe]4f^{14}6s^2$. Since 14 is the maximum number of electrons in the f shell, this shell is closed and the $6s^2$ electrons are the valence electrons interacting with the environment, causing Yb to behave in the same way as alkaline-earth atoms. Therefore, I will use the term alkaline-earth-like atoms to refer to Yb and alkaline-earth atoms. Most of the work in this thesis has been done on the example of Yb and Sr, however, in principle it is more general than that and also applicable to other alkaline-earth-like atoms. In the ground state, the spins of the two electrons couple together to give zero total electron spin. Since, in the ground state, the electronic orbital angular momentum is also zero, the total

angular momentum of the electrons also has to be zero and the ground state is 1S_0 , and the only relevant spin is the nuclear spin. For the bosonic isotopes of Sr and Yb, the nuclear spin is also zero, resulting in a completely spinless ground state. However, both Sr and Yb have a multitude of different stable isotopes, with different nuclear spins, including both fermions with finite nuclear spin and bosons. The stable isotopes of Yb and Sr are given in table 1.1.

atomic nr. (Yb)	i
168	0
170	0
171	1/2
172	0
173	3/2
174	0
176	0

atomic nr. (Sr)	i
84	0
86	0
87	9/2
88	0

Table 1.1: The stable isotopes of Yb and Sr, i denotes the nuclear spin. For the purposes of this thesis, the fermionic isotopes are relevant, specifically ^{171}Yb and ^{87}Sr .

In the excited states, the electron spins can be coupled together to give a finite electron spin of $s = s_1 + s_2 = 1$, giving rise to triplet excited states, as for example the $(nsnp) ^3P_j$ state, which is the lowest excited state, with $n = 5$ for Sr and $n = 6$ for Yb. Due to selection rules, direct coupling between singlet and triplet states is forbidden. However, these states are not pure spin-orbit LS coupling, causing an admixture of the higherlying $(nsnp) ^1P_1$ state, such that [7, 24]

$$|^3P_2\rangle = |^3P_2^0\rangle \tag{1.4a}$$

$$|^3P_1\rangle = \alpha|^3P_1^0\rangle + \beta|^1P_1^0\rangle \tag{1.4b}$$

$$|^3P_0\rangle = |^3P_0^0\rangle \tag{1.4c}$$

$$|^1P_1\rangle = -\beta|^3P_1^0\rangle + \alpha|^1P_1^0\rangle, \tag{1.4d}$$

where the states with the superscript 0 denote states with pure spin-orbit coupling.

Hence, the intercombination transition $^1S_0 \rightarrow ^3P_1$ is weakly allowed,

$$\langle ^3P_0 | \mathbf{d} \cdot \boldsymbol{\epsilon} | ^3P_1 \rangle = \alpha \langle ^3P_0^0 | \mathbf{d} \cdot \boldsymbol{\epsilon} | ^3P_1^0 \rangle + \beta \langle ^3P_0^0 | \mathbf{d} \cdot \boldsymbol{\epsilon} | ^3P_1^0 \rangle. \quad (1.5)$$

where the first part on the right side is zero. This results in a line width of 182 kHz for ^{171}Yb and 80 kHz for ^{87}Sr . The transition from the ground state to the 3P_0 and 3P_2 is additionally forbidden, since the selection rules for j require $\Delta j = 0, 1$ and $j = 0 \nrightarrow j = 0$, causing lifetimes on the order of 1000 years for the metastable 3P_0 state for the bosonic isotopes. For fermionic alkaline-earth-like elements, which have half-integer nuclear spin, however, the hyperfine interaction couples the states with equal total spin f and thus causes an additional admixture of the $|^3P_1\rangle$, $|^1P_1\rangle$ and $|^3P_2\rangle$ states to the $|^3P_0\rangle$ state, resulting in

$$|^3P_0\rangle = |^3P_0^0\rangle + \alpha_0|^3P_1\rangle + \beta_0|^1P_1\rangle + \gamma_0|^3P_2^0\rangle. \quad (1.6)$$

This reduces the lifetime of the clock transition, $^1S_0 \rightarrow ^3P_0$ to about 100 s for ^{87}Sr and to 10 s for ^{171}Yb with its larger hyperfine interaction [24]. It is also possible to induce a similar coupling with the application of a magnetic field or an additional laser and to thus reduce the lifetime of the clock state of the bosonic elements [25, 26]. These long lifetimes, in combination with easily accessible transition frequencies, have caused the alkaline-earth-like elements to emerge in different areas of quantum control, most notably in the implementation of atomic clocks, as pointed out in Section 1.

Due to the fact that their only spin is the nuclear spin, the Hamiltonian for the $|^3P_0\rangle$ and the $|^1S_0\rangle$ state in the presence of a weak magnetic field \mathbf{B} is given by

$$H_Z = g_S \mu_B \hat{\mathbf{S}} \cdot \mathbf{B} / h + g_L \mu_B \hat{\mathbf{L}} \cdot \mathbf{B} / h - g_I \mu_B \hat{\mathbf{I}} \cdot \mathbf{B} / h \quad (1.7)$$

Where μ_B is the Bohr magneton, $g_S \simeq 2$ and $g_L = 1$ are the g-factors for electron spin and electron orbital angular momentum respectively, and g_I is the nuclear g-factor. In the absence of the small admixture of the $|^3P_1\rangle$ state to the $|^3P_0\rangle$ state, Eq. (1.7) would reduce to $-g_I \mu_B \hat{\mathbf{I}} \cdot \mathbf{B} / h$ and the nuclear g-factor g_I of the $|^3P_0\rangle$ state would be exactly the same as for the $|^1S_0\rangle$ ground state. However, the coupling between the

two states causes a small admixture of the electron g-factor to the nuclear g-factor. This leads to a differential g-factor δg for the $|^3P_0\rangle$ state compared to the ground state. For ^{87}Sr , the difference in g-factors between the two states is about 60%. [24]. Furthermore, the quantum number for the Zeeman interaction for a magnetic field along the z -axis is not pure m_i any more, but m_f , due to the small admixture of the other states, causing the Zeeman shift to be $\delta g m_f \mu_B B / h$. This effect has to be taken into account for applications in optical clocks as well as for coherent transfer of population from different nuclear spin states in the ground state to the $|^3P_0\rangle$ state. On the other hand, together with the extremely narrow linewidth of the $|^3P_0\rangle$ state, this also allows for controlled excitation of different nuclear spin states independently from each other, which makes complete control over the nuclear spin submanifold of these states possible.

1.4 Overview of Thesis

This thesis aims to elucidate different aspects of control of ultracold atoms in optical lattices, focusing on controlled collisions and optical recooling while preserving internal coherences. All these aspects could be useful in the application of quantum information and, more generally, in basic research e.g. on many-body states. In Chapter 2, I will give the theoretical background behind many of the calculations done in this thesis. Chapter 3 will show the possibility of recooling of neutral alkaline-earth atoms, while preserving nuclear spin coherences. This makes neutral alkaline-earth-like atoms with nuclear-spin qubits the only system of neutral atoms that allows optical recooling of qubits between and during the implementation of quantum gates, ensuring high fidelity of subsequent gates. Chapter 4 will elaborate on the possibilities of using optical Feshbach resonances to control alkaline-earth-like atoms and to speed up quantum gates. Finally, in chapter 5, I will summarize and provide an outlook to open questions in the field.

Several parts of this dissertation have previously been published, as is shown in Table 1.2. Furthermore, I developed a quasi-Hermitian pseudopotential for the calculation of higher partial-wave collisions. While the pseudopotential proposed by R. Stock *et al.* [27, 28] is not Hermitian, it can still be used to calculate the eigenenergies of atoms colliding via higher partial waves. However, it does not give rise to a complete, orthogonal set of wave functions that can be used to expand possible additional parts of a Hamiltonian. The quasi-Hermitian pseudopotential on the other hand gives rise to a biorthonormal set of wave functions that can be applied to this purpose. This research was published in [29], but is not shown here.

Chapter	Publication
Chapter 3	I. Reichenbach and I. H. Deutsch Sideband Cooling while Preserving Coherences in the Nuclear Spin State in Group-II-like Atoms, Phys. Rev. Lett. 99 , 123001 (2007) [30]
Chapter 4	I. Reichenbach, P. S. Julienne and I. H. Deutsch Controlling nuclear spin exchange via optical Feshbach resonances in ^{171}Yb , accepted for Phys. Rev. A
–	I. Reichenbach, A. Silberfarb, R. Stock and I. H. Deutsch Quasi-Hermitian pseudopotential for higher partial wave scattering Phys. Rev. A 74 , 042724 (2006) [29]

Table 1.2: List of publications and the corresponding parts of this dissertation, if applicable.

Chapter 2

Theoretical Background

In this dissertation I consider the manipulation of ultracold alkaline-earth-like atoms trapped in optical lattices and their use in the implementation of quantum information processing. Here, I will give some of the theoretical background which is the basis of many of the calculations shown in later chapters.

At the fundamental level, quantum many-body systems are governed by their two-body interactions. In the case of ultracold neutral atoms, these consist of collisions determined by the diatomic molecular interaction potential. Therefore, in the first section of this Chapter, I will give a general overview of scattering theory, which is necessary to understand the scattering length, a very important parameter which is manipulated with Feshbach resonances and is at the heart of the control scheme proposed in Chapter 4.

In Section 2.2, I will show how ultracold collisions of atoms in optical lattices can be controlled and how these controlled collisions of ultracold atoms can be used to implement a quantum gate by utilizing the effects of symmetry and the Pauli-exclusion principle.

In the last section, the molecular basis states used for the calculation of the

optical Feshbach resonances in Chapter 4, as well as their transformations, will be derived.

2.1 Scattering Theory

Scattering theory, which describes the effects of collisions of two or more particles on their states, is a very important tool in theoretical physics. For this dissertation, it is the basis for both controlled collisions and Feshbach resonances as used in Chapter 4. For this reason, I will give a short overview of scattering theory, limited to two colliding particles in the center of mass frame or, equivalently, the scattering of one particle off a stationary target. For more information, see the textbook by Taylor [31].

Consider a scattering event that consists of two particles which interact via a potential $V(r)$ with finite range, colliding at time $t = t_0$. At time $t \rightarrow -\infty$ the incoming state $|\psi_{in}\rangle$ is outside of the range of the scattering potential $V(r)$. However, at time t_0 it has moved into the range of the potential and has become the state

$$|\psi\rangle = \hat{\Omega}_+ |\psi_{in}\rangle, \quad (2.1)$$

where Ω_+ is the Møller operator that embodies the evolution of the undisturbed incoming state and

$$|\psi\rangle = \hat{\Omega}_- |\psi_{out}\rangle \quad (2.2)$$

describes the evolution from time $t = t_0$ to the outgoing state $|\psi_{out}\rangle$ at time $t \rightarrow \infty$ that is again outside of the range of the interaction potential, with the corresponding Møller operator $\hat{\Omega}_-$ [31].

Since usually, only the incoming and the outgoing state are known, it is advantageous to cast the problem in terms of the so-called S -matrix, which describes the

evolution from the incoming state to the outgoing state

$$\hat{S} = \hat{\Omega}_-^\dagger \hat{\Omega}_+, \quad (2.3)$$

such that

$$|\psi_{out}\rangle = \hat{S}|\psi_{in}\rangle \quad (2.4)$$

Therefore, the S -matrix connects the outgoing state after the scattering event to the incoming state before the scattering event. Depending on the size of the relevant Hilbert space, it can have many channels, denoting different possible internal and external degrees of freedom of the two interacting particles.

It is also possible, and often more convenient, to describe the scattering process in a time-independent picture. To do this, we expand the scattering states into the basis of plane waves $|\mathbf{p}\rangle = e^{i\mathbf{p}\mathbf{r}}$, considering one of the colliding particles a stationary target. The Møller operators acting on a plane wave state then yield the stationary scattering states,

$$|\mathbf{p}\pm\rangle = \hat{\Omega}_\pm|\mathbf{p}\rangle. \quad (2.5)$$

These states are improper eigenstates of the time-independent Hamiltonian

$$H|\mathbf{p}\pm\rangle = E_p|\mathbf{p}\pm\rangle, \quad (2.6)$$

and their wave function in position space is given by

$$\langle \mathbf{x}|\mathbf{p}\pm\rangle \xrightarrow{r \rightarrow \infty} (2\pi)^{3/2} \left(e^{i\mathbf{r}\mathbf{p}} + f \frac{e^{i\mathbf{r}\mathbf{p}}}{r} \right), \quad (2.7)$$

where f is the scattering amplitude. This gives a natural connection to the wave mechanics of quantum theory, where the time-independent Schrödinger equation can be used to solve problems with time-independent potentials. The scattering process can now be described as a superposition of the incoming plane wave and a radial wave that is scattered from the target.

In many cases, the Hamiltonian and therefore the S -matrix are invariant under rotation. In this case, we can define the stationary basis states with energy E , total angular momentum l and projection of the angular momentum m in terms of the spherical harmonics and a radial part

$$|E, l, m\rangle = R_l(r)Y_l^m(\theta, \phi) \quad (2.8)$$

The S -matrix is diagonal in the $|E, l, m\rangle$ basis

$$\langle E', l', m' | \hat{S} | E, l, m \rangle = \delta(E' - E) \delta_{l'l} \delta_{m'm} s_l(p). \quad (2.9)$$

Here $s_l(p)$ is the S -matrix for a given “partial wave” with well-defined total angular momentum l . The radial part of the time independent Schrödinger equation (TISE) becomes

$$\left[\frac{\hbar^2}{2\mu} \frac{d^2}{dr^2} - \frac{l(l+1)}{r^2} + V(r) \right] R_l(r) = E_k R_l(r). \quad (2.10)$$

Ultracold atoms can have a very long deBroglie wavelength, on the order of microns, whereas the van der Waals interaction for alkali atoms is on the order of 1-10 Å[32]. In this case, the expansion in partial waves is very useful, due to the fact that the kinetic energies are very small compared to the centrifugal barriers $l(l+1)/r^2$ for higher l partial waves, which therefore do not interact and can be ignored. In fact, very often it is sufficient to only take the first few partial waves, namely s and p waves into account. This is due to the Wigner-threshold law, which states that for low energies, the phase shift scales as $\delta_l(k) \propto -k^{2l+1}$, where k is the deBroglie wave number for the relative motion. Here δ_l is the scattering phase shift, which in turn is given by

$$s_l = e^{i2\delta_l}. \quad (2.11)$$

For scattering from a short-range, radially symmetric potential, the effect of the interaction is to phase shift the radial wave function. The stationary scattering solutions are then given by

$$\psi_{l,p}(r) \xrightarrow{r \rightarrow \infty} j_l(pr) + p f_l(p) e^{i(pr - l\pi/2)}, \quad (2.12)$$

where j_l is a spherical Bessel function and f_l is the scattering amplitude for partial wave l , which can be written as

$$f_l(p) = \frac{1}{p} e^{i\delta_l} \sin(\delta_l). \quad (2.13)$$

The scattering phase shift δ_l denotes the amount by which a free stationary scattering state is phase shifted due to the interaction process, as can be seen by inserting Eq. (2.12) into Eq. (2.13), which yields

$$\psi_{l,p}(r) \xrightarrow{r \rightarrow \infty} e^{i\delta_l(p)} \sin(pr - l\pi/2 + \delta_l(p)). \quad (2.14)$$

In the context of cold atom scattering, the phase shift δ_l is often used to define the scattering length, which is given as [28]

$$a_l^{2l+1} = - \lim_{k \rightarrow 0} \frac{\tan(\delta_l)}{k^{2l+1}} \quad (2.15)$$

In the Wigner-threshold regime, the scattering length is thus independent of the energy. If the scattering potential $V(r)$ was modeled as a hard-sphere interaction, the scattering length gives the radius of the hard sphere. Its physical significance arises from the fact that the strength of the interaction and whether it is attractive ($a < 0$) or repulsive ($a > 0$) can be codified in a single parameter. Furthermore, it is possible to replace the potentially very complicated interaction potential $V(r)$ with a zero-range pseudo-potential, where the only free parameter is the scattering length, and obtain the same physical parameters [33, 28]. Even outside the Wigner-threshold regime the complicated potential $V(r)$ can often be replaced by a pseudopotential. However, then the scattering length is not independent of k and a self-consistent solution is needed [28, 34].

Generally, if all the different scattering states are accounted for, the S -matrix must be unitary, $\hat{S}^\dagger \hat{S} = 1$. Moreover, sometimes the scattering process only causes a phase shift between the different channels, thus the S -matrix is diagonal with a phase for every channel. In this case, the scattering process in the different channels is elastic, and the part of the wave function entering in one specific channel will stay

in this channel. The individual diagonal S -matrix elements therefore square to one, $|S_{\alpha,\alpha}|^2 = 1$. However, in some cases the scattering produces loss from one or more channels, and the diagonal elements of the S -matrix are not simple phases anymore. The loss rate out of the this channel is then given by

$$\mathcal{K} = \frac{2\pi\hbar}{\mu k} (1 - |S_{\alpha,\alpha}|^2), \quad (2.16)$$

with the diagonal matrix element of the S -matrix for channel α , $S_{\alpha,\alpha} = \langle \alpha | \hat{S} | \alpha \rangle$. Note that this is the loss rate for collisions of identical particles, for distinguishable particles the loss rate is half of the value given in Eq. (2.16) [35]. We can account for these losses by introducing a complex scattering phase shift, $\delta = \delta' + i\delta''$. There are different ways of defining the scattering length, which is also complex, and can be written as $a - ib$, where the real part a defines the coherent part of the interaction, while the imaginary part b is related to the loss rate. Assuming that δ is small, we can use $\tan \delta \approx \delta$, and therefore $a \approx \delta'/k$ and $b \approx -\delta''/k$. Then it is also possible to write

$$\hat{S} = e^{2i(\delta)} \approx 1 + 2i(\delta) \approx 1 + 2ika + 2kb. \quad (2.17)$$

This is the definition I will use in Chapter 4.

The scattering length can also be written in terms of the K -matrix, which is given by

$$\hat{K} = i \frac{1 - \hat{S}}{1 + \hat{S}} = \tan \delta \quad (2.18)$$

The scattering length becomes then

$$a - ib = \frac{i}{k} \hat{K}. \quad (2.19)$$

Deep in the Wigner regime, where a is independent of k , the resulting scattering length is the same. However, if the scattering length is not completely independent of k , its definition is not unique and depends on the application at hand.

2.2 Controlled Collisions in Quantum Information Processing

Usually, even though scattering events are coherent, as can be seen from the unitarity of the scattering matrix, collisions are viewed as inherently messy and intractable. This is due to the huge number of possible channels that can participate in the collision, even though all of the probability amplitude can emerge on one channel at long range. However, for ultracold atoms, the number of partial waves and with it the number of channels is greatly reduced, making it possible to keep track of the different channels [36]. Confining ultracold atoms to a trap and then moving them together in a controlled fashion, such that they can interact for a determined amount of time constitutes a controlled collision. Due to their interaction, the energy of the atoms is changed and causes the wave function to acquire a phase. This can be used for the implementation of quantum information processing, if the collision acts selectively on atoms in different states. There are several different ways of accomplishing this. One possibility, which has been suggested for alkalis, is to encode the qubits in different hyperfine states of ground state atoms, which are then trapped in a state-dependent optical lattice. Changing the angle between the polarization of the optical lattice beams then causes the atoms to move in the $+z$ or $-z$ direction, depending on their internal state, until they collide with their next neighbors in the other hyperfine state. A schematic of this process is shown in figure 2.1. This in turn can be used to implement an entangling gate conditional on the states of the qubit and thus to create a cluster state [28, 37].

Alkaline-earth-like atoms allow for a different scheme. As discussed in Section 1.3, in the ground state, their electronic degrees of freedom are decoupled from the nuclear spins, making it possible to store the quantum information in the nuclear spin, which leads to very long coherence times, due to the weak nuclear magnetic moment and resulting weak magnetic dipole interaction. It is, however, still possible

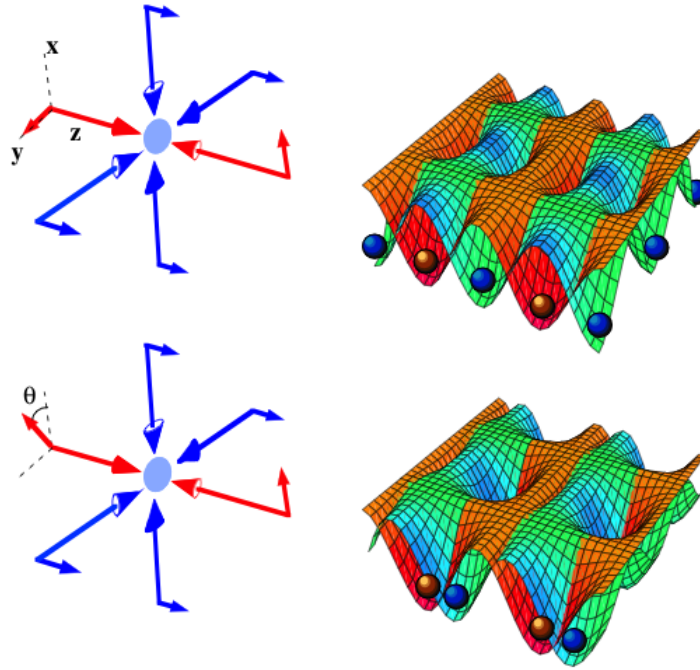


Figure 2.1: Schematics of the implementation of a state dependent controlled collision with alkalis. Depending on their internal (hyperfine) state, the atoms are trapped in optical lattices with different polarization. Changing the angle between the counterpropagating laser beams changes the relative position between the lattices and therefore the relative position of the atoms in different hyperfine states.

to accomplish relatively fast gates, by utilizing the effects of quantum statistics via the so-called “exchange blockade” [13]. Since the nuclear spins are the only spins in the ground state, they determine the quantum statistics of the system, allowing or forbidding the interaction between different atoms. Consider two fermionic alkaline-earth-like atoms, with a nuclear spin of $i = 1/2$ and quantum information stored in the polarization of the nuclear spin in the usual way, $|\uparrow\rangle = |0\rangle$ and $|\downarrow\rangle = |1\rangle$, trapped in two neighboring sites of an optical lattice. Now the atoms are brought together to allow them to interact via a controlled collision. If the nuclear spins of both atoms are up or down, they are in the spin triplet state. This state is symmetric

under parity. Since the overall wave function has to be antisymmetric for fermions, the overall spatial wave function has to be antisymmetric, requiring the atoms to interact with odd partial wave functions, that is, only via p-wave collisions for cold enough atoms

$$|0, 0\rangle = |\uparrow\uparrow\rangle|\Psi_-(x_1, x_2)\rangle = |\uparrow\uparrow\rangle|\Psi_{p\text{-wave}}\rangle \quad (2.20a)$$

$$|1, 1\rangle = |\downarrow\downarrow\rangle|\Psi_-(x_1, x_2)\rangle = |\downarrow\downarrow\rangle|\Psi_{p\text{-wave}}\rangle. \quad (2.20b)$$

However, if one of the atoms is in the nuclear spin up state and the other one in nuclear spin down, then they are in a superposition of spin triplet and singlet state,

$$\begin{aligned} |1, 0\rangle &= \frac{1}{\sqrt{2}} (|\Psi_-(x_1, x_2)\rangle\chi_T - |\Psi_+(x_1, x_2)\rangle\chi_S) \\ &= \frac{1}{\sqrt{2}} (|\Psi_{p\text{-wave}}\rangle\chi_T - |\Psi_{s\text{-wave}}\rangle\chi_S) \end{aligned} \quad (2.21a)$$

$$\begin{aligned} |0, 1\rangle &= \frac{1}{\sqrt{2}} (|\Psi_-(x_1, x_2)\rangle\chi_T + |\Psi_+(x_1, x_2)\rangle\chi_S) \\ &= \frac{1}{\sqrt{2}} (|\Psi_{p\text{-wave}}\rangle\chi_T + |\Psi_{s\text{-wave}}\rangle\chi_S). \end{aligned} \quad (2.21b)$$

Here $|\Psi_{\pm}(x_1, x_2)\rangle = |\Psi_A(x_1)\rangle|\Psi_B(x_2)\rangle \pm |\Psi_B(x_1)\rangle|\Psi_A(x_2)\rangle$, where the subscript A, B stands for the respective lattice site and the subscript 1, 2 stands for the respective atoms. $|\Psi_{s\text{-wave}}\rangle$ ($|\Psi_{p\text{-wave}}\rangle$) denotes that $|\Psi_{\pm}(x_1, x_2)\rangle$ interacts via s-wave (p-wave) collisions. Furthermore, $\chi_{T/S} = (|\uparrow\rangle|\downarrow\rangle \pm |\downarrow\rangle|\uparrow\rangle)/\sqrt{2}$. As shown by Hayes in [13], depending on the temperature and on the relative scattering lengths for p-waves and s-waves, the singlet nuclear spin part acquires a phase ϕ relative to the triplet in such a controlled collision. The nuclear spin wave functions become then

$$|1, 0\rangle \rightarrow \frac{1}{\sqrt{2}} (|\Psi_{p\text{-wave}}\rangle\chi_T - e^{-i\phi}|\Psi_{s\text{-wave}}\rangle\chi_S) \quad (2.22a)$$

$$|0, 1\rangle \rightarrow \frac{1}{\sqrt{2}} (|\Psi_{p\text{-wave}}\rangle\chi_T + e^{-i\phi}|\Psi_{s\text{-wave}}\rangle\chi_S). \quad (2.22b)$$

If now the acquired phase is $\phi = \pi$, this results in a *SWAP* gate for the atoms. Similarly, if the singlet wave function acquires a phase of $\pi/2$, the resulting gate is $\sqrt{\text{SWAP}}$, which is an entangling interaction. Thus it is possible to create entangling

gates for nuclear spin qubits, utilizing effects of quantum statistics, even though the nuclear spins never directly interact with each other [13]. As will be described in chapter 4, the application of optical Feshbach resonances allows for separate control of the p-wave scattering length relative to the s-wave scattering length and therefore the relative phase, even independently of the temperature, as long as the atoms are still cold enough to suppress higher partial waves.

2.3 Molecular States

The understanding of ultracold collisions and especially the modeling of optical Feshbach resonances hinges critically on the understanding of the relevant molecular potentials. To suppress higher partial waves, optical Feshbach resonances take place at very low energies, equivalent to temperatures of few nK to tens of μK . Furthermore, to achieve a large overlap with the ground state scattering wave function, only very long-range molecular states are considered. This results in molecules for which the physical properties of the constituent atoms, e.g. spin and orbital angular momentum of the electrons are still tractable. Additionally, spin-orbit coupling and even hyperfine interactions can be important on the energy scale of the molecular binding, whereas the chemical binding region for much shorter ranges and more deeply bound molecules does not have to be modeled in detail and can be approximated with Lennard-Jones potential [39, 40]. The different molecular states are then determined by the different couplings of the angular momenta of the atoms to each other.

Throughout this dissertation, I will use the following notation. Each atom has two electrons with a combined orbital angular momentum \mathbf{l} , electron spin \mathbf{s} , and nuclear spin \mathbf{i} . To differentiate between the angular momenta of the two atoms, each of these angular momenta will have a subscript $k = 1, 2$, denoting atom 1 or 2. Generally, lower case letters are used for angular momenta of single atoms, whereas

capital letters are used for coupled molecular angular momenta. For example, the two electron spins of the two atoms \mathbf{s}_1 and \mathbf{s}_2 can couple to the molecular electron spin $\mathbf{s}_1 + \mathbf{s}_2 = \mathbf{S}$. However, in another coupling scheme it is also possible that the electron spin and the electron orbital momentum of atom 1 are coupled to give the total electron angular momentum of atom 1, $\mathbf{s}_1 + \mathbf{l}_1 = \mathbf{j}_1$. An additional, very important angular momentum is the rotation of the nuclei \mathbf{R} , which is always perpendicular to the line connecting the two nuclei. Finally, all the angular momenta are added to yield a total angular momentum \mathbf{T} that, together with the parity p , is always a good quantum number. The details of the different couplings between the atoms depends on the relative strength of the competing interactions between the angular momenta and is summarized in the so-called Hund's cases, which will be described in the next section. Ignoring hyperfine interaction for the moment, there are only three relevant interactions between the atoms [41]. These are the electrostatic interaction, the spin-orbit interaction and the spin-rotation coupling. I will now summarize the effects of each of these, assuming homonuclear dimers. \hbar will be set to one in this section.

The *electrostatic* interaction constrains the electronic wave function to rotate with the nuclei. For two separated neutral atoms at large internuclear distances the dominant interaction is given by a dipole-dipole interaction

$$V_{dd} = \frac{1}{4\pi\epsilon_0} \frac{\hat{\mathbf{d}}_1 \cdot \hat{\mathbf{d}}_2 - 3\hat{d}_{1a}\hat{d}_{2a}}{R^3}, \quad (2.23)$$

where ϵ_0 is the permittivity of vacuum, $\hat{\mathbf{d}}_k$ is the dipole of the state atom k , while d_{ka} is the projection of the dipole along the internuclear axis \mathbf{a} . In the ground state, where both atoms are in a S state, the resonant-dipole interaction does not couple the atoms. However, in second order perturbation theory a coupling appears, giving rise to the C_6/r^6 van der Waals interaction. We also consider electronic excited states which, for infinite separation, consist of one atom in the ground state S and another one in an excited P state, e.g. the 3P_1 state for alkaline-earths. Neither of these states has a dipole moment, however, if the atoms are close enough together,

they will be in a superposition of $S + P$ state. These superpositions do have a dipole moment and will thus interact resonantly with each other, causing a C_3/r^3 potential, which is now dominant for large internuclear distances. The magnitude of the dipole d can be calculated from the linewidth of the excited atomic state, via

$$\Gamma = \left(\frac{\omega}{c}\right)^3 \frac{d^2}{3\pi\epsilon_0\hbar}. \quad (2.24)$$

Note that in the case mentioned above, there are four different possible configurations of the dipoles to each other (perpendicular to the a -axis and either parallel or antiparallel to each other or parallel to the a -axis and parallel or antiparallel to each other), thus leading to four different r^{-3} potentials. The strength of the electrostatic interaction is denoted by $|\Delta E_{dd}|$, which is the energy difference between two neighboring C_n/r^n potentials [41].

The *spin-orbit* interaction couples the electronic spin \mathbf{s} and the orbital angular momentum \mathbf{l} of each atom together, resulting in an effective interaction term

$$\mathcal{A}_{SO}(\hat{\mathbf{l}}_1 \cdot \hat{\mathbf{s}}_1 + \hat{\mathbf{l}}_2 \cdot \hat{\mathbf{s}}_2) = \mathcal{A}_{SO}/2(\hat{\mathbf{l}}_1^2 + \hat{\mathbf{s}}_1^2 - \hat{\mathbf{j}}_1^2 + \hat{\mathbf{l}}_2^2 + \hat{\mathbf{s}}_2^2 - \hat{\mathbf{j}}_2^2). \quad (2.25)$$

Therefore, the spin-orbit coupling causes the electron spin and electron orbital angular momenta of the single atoms to be coupled to a total electron angular momentum of the single atoms and its relative strength is given by the size of $|\mathcal{A}_{SO}|$.

The rotation of the nuclei gives rise to a magnetic field, which couples to the spin of the electrons and thus gives rise to the *spin-rotation* coupling. This can be expressed as $\mathcal{C}\mathbf{R} \cdot \mathbf{S}$, where \mathcal{C} is a constant whose value depends on the rotational constant $\mathcal{B} = \hbar^2/(2\mu r_0^2)$, with the reduced mass μ and the equilibrium distance between the nuclei r_0 . The relative importance of the spin-rotation coupling is given by the size of \mathcal{B} relative to $|\Delta E_{dd}|$ and $|\mathcal{A}_{SO}|$. Due to the long range interactions considered in this thesis and the big mass of both Sr and especially Yb, the rotational energy usually is small here.

2.3.1 Hund's Cases

The coupling of the different angular momenta of the two atoms depends on the relative strengths of the interactions explained above. F. Hund identified five different limiting cases, which are now labeled Hund's cases a) through e) [41]. However, for the classification of ultracold colliding atoms used in this thesis, only three of them are relevant. Since the relative strengths of the different coupling constants depend on the relative distance between the nuclei, one and the same molecule can be in different Hund's cases for different distances between the nuclei.

The most relevant Hund's case for this dissertation is Hund's case c), in which the relative sizes of the different coupling strengths is given by

$$|\mathcal{A}_{SO}| \gg |\Delta E_{dd}| \gg \mathcal{B} \quad (2.26)$$

The result is that first the electron spin and the electron orbital angular momentum for each atom are coupled together separately, that is, $\mathbf{s}_1 + \mathbf{l}_1 = \mathbf{j}_1$, $\mathbf{s}_2 + \mathbf{l}_2 = \mathbf{j}_2$. These total electron angular momenta are then coupled together such that $\mathbf{j}_1 + \mathbf{j}_2 = \mathbf{J}$. Finally, \mathbf{J} is coupled to the rotational angular momentum to give the total angular momentum, $\mathbf{J} + \mathbf{R} = \mathbf{T}$. Since \mathbf{R} is perpendicular to the internuclear axis, its projection is zero and the projection of \mathbf{T} on the internuclear axis is the same as the projection of \mathbf{J} on the internuclear axis, Ω . Both \mathbf{T} and Ω are good quantum numbers as is M_T , the projection of \mathbf{T} on a space-fixed axis \mathbf{z} , as will be explained in more detail in Section 2.3.3. Additionally, the states are even (gerade) or odd (ungerade) under inflection of all electrons through the center of charge. This symmetry is denoted by $\sigma = u/g$. The states with $\Omega \neq 0$ are doubly degenerate, whereas the states with $\Omega = 0$ are not degenerate and are even or odd under reflection of the electron wave function on a plane through the internuclear axis. Therefore, Hund's case c) states are labeled

$$\Omega_{\sigma}^{\pm}, \quad (2.27)$$

where the superscript \pm denotes the latter symmetry and is only applicable for states with $\Omega = 0$.

In the context of cold collisions, Hund's case e) is another important coupling case. Here the different coupling strengths can be ordered as

$$|\mathcal{A}_{SO}| \gg \mathcal{B} \gg |\Delta E_{dd}|. \quad (2.28)$$

In this case, the spin-orbit coupling dominates over the rotation, which in turn dominates over the resonant dipole interaction. The electron spin of each atom is again coupled with the orbital angular momentum of the electron to the total electron angular momentum, $\mathbf{s}_1 + \mathbf{l}_1 = \mathbf{j}_1$ and $\mathbf{s}_2 + \mathbf{l}_2 = \mathbf{j}_2$, followed by the coupling of \mathbf{j}_1 and \mathbf{j}_2 to $\mathbf{J} = \mathbf{j}_1 + \mathbf{j}_2$. Finally, \mathbf{J} and the orbital angular momentum of the nuclei are coupled together to give the total angular momentum $\mathbf{T} = \mathbf{J} + \mathbf{R}$. In contrast to Hund's case c), Ω is not a good quantum number in Hund's case e), because \mathbf{J} does not precess around the internuclear axis, due to the weak spin-rotation coupling. However, M_T , the projection of \mathbf{T} on a space-fixed axis is a good quantum number.

A third case, which I will describe for completeness because it is generally important for the description of ultracold atoms, even though it is not used in the calculations shown here, is the Hund's case a). This case is given by

$$|\Delta E_{dd}| \gg |\mathcal{A}_{SO}| \gg \mathcal{B}. \quad (2.29)$$

In this case, the electron spin of the two atoms is coupled together to give a total electron spin, $\mathbf{S} = \mathbf{s}_1 + \mathbf{s}_2$, and the electron orbital momentum is also coupled together to a molecular orbital electron angular momentum, $\mathbf{L} = \mathbf{l}_1 + \mathbf{l}_2$. Both of these angular momenta then precess around the internuclear axis, and the projection of \mathbf{S} and \mathbf{L} on the internuclear axis, Σ and Λ are therefore also good quantum numbers. Due to the spin-orbit coupling, \mathbf{L} and \mathbf{S} are now coupled to \mathbf{J} , whose projection on the internuclear axis, $\Omega = \Lambda + \Sigma$ is also a good quantum number. Finally, \mathbf{J} and \mathbf{R} are again coupled to give \mathbf{T} , whose projection is again equal to Ω . These states are

again symmetric under inflection of all electrons through the center of charge, which is denoted by $\sigma = \pm 1 = g/u$. Furthermore, the states with $\Lambda = 0$ have an additional symmetry, they are even or odd under inflection of the spatial component of the electron wave function on a plane including the internuclear axis. The molecular eigenstates are then labeled by

$${}^{2S+1}\Lambda_{\sigma}^{\pm}, \quad (2.30)$$

where the superscript \pm signifies the last mentioned symmetry and is only applicable in the case $\Lambda = 0$.

2.3.2 Including Nuclear Spin and Hyperfine Interaction

Since the main topic of this dissertation is the manipulation of nuclear spins with controlled collisions, the Hund's cases mentioned above have to be extended to include both the nuclear spin i_k of the atoms as well as the hyperfine interaction, which is given by

$$H_{HF} = A(\hat{\mathbf{j}}_1 \cdot \hat{\mathbf{i}}_1 + \hat{\mathbf{j}}_2 \cdot \hat{\mathbf{i}}_2) = A/2 \left(\hat{\mathbf{f}}_1^2 - \hat{\mathbf{i}}_1^2 - \hat{\mathbf{j}}_1^2 + \hat{\mathbf{f}}_2^2 - \hat{\mathbf{i}}_2^2 - \hat{\mathbf{j}}_2^2 \right). \quad (2.31)$$

The hyperfine interaction constant A is smaller than the spin-orbit coupling constant \mathcal{A}_{SO} . For the Hund's case c), there are thus several possibilities for the size of the hyperfine interaction relative to $|\Delta E_{dd}|$ and \mathcal{B} . For ${}^{171}\text{Yb}$, which has a large hyperfine interaction and a large mass, it makes sense to consider the case in which $|A| \gg \mathcal{B}$. This reduces the extension of Hund's case c) to two different possibilities, $|\mathcal{A}_{SO}| \gg |\Delta E_{dd}| \gg |A| \gg \mathcal{B}$ and $|\mathcal{A}_{SO}| \gg |A| \gg |\Delta E_{dd}| \gg \mathcal{B}$.

The first case,

$$|\mathcal{A}_{SO}| \gg |\Delta E_{dd}| \gg |A| \gg \mathcal{B}, \quad (2.32)$$

is the one relevant in this thesis. Here, a total nuclear spin $\mathbf{I} = \mathbf{i}_1 + \mathbf{i}_2$ is formed, which precesses around the internuclear axis \mathbf{a} and whose projection on that axis, ι ,

is a good quantum number. \mathbf{I} and \mathbf{J} are then coupled together to obtain the total angular momentum (absent rotation) \mathbf{F} , which is also precessing around \mathbf{a} with the projection $\Phi = \Omega + \iota$. Finally, the total angular momentum $\mathbf{T} = \mathbf{F} + \mathbf{R}$ is formed, with the same projection Φ along the internuclear axis. This is the extended Hund's case c) basis used in chapter 4, which can be written as

$$|\gamma\rangle = |J\Omega I\iota; T\Phi M_T\rangle = \sum_{(JI)F\Phi} \langle (JI)F\Phi | J\Omega I\iota \rangle | (JI)F\Phi \rangle \sqrt{\frac{2T+1}{4\pi}} \mathcal{D}_{\Phi, M_T}^{T*}. \quad (2.33)$$

where $\mathcal{D}_{\Phi, M_T}^{T*}$ is the symmetric top wave function as explained in the next section.

For Hund's case e), there are again several possibilities for the relative size of the hyperfine interaction compared to the other interactions. The case used in this dissertation is defined by

$$|\mathcal{A}_{SO}| \gg |A| \gg \mathcal{B} \gg |\Delta E_{dd}|, \quad (2.34)$$

causing the following coupling of angular momenta: $\mathbf{j}_1 + \mathbf{i}_1 = \mathbf{f}_1$, $\mathbf{j}_2 + \mathbf{i}_2 = \mathbf{f}_2$. These momenta are then coupled together to give $\mathbf{F} = \mathbf{f}_1 + \mathbf{f}_2$, which rotates around the internuclear axis with the projection Φ . Finally, \mathbf{F} and \mathbf{R} are again coupled to yield the total angular momentum \mathbf{T} .

2.3.3 Molecular States for Nuclear Rotation

So far, I have discussed the different coupling cases of the angular momenta and the resulting good quantum numbers, but not the effects of the rotation of the nuclei on the different other angular momenta. This will be explained in more detail in this Section.

To this end, it is first necessary to consider the relevant coordinate systems for diatomic molecules. One natural coordinate system for the manipulation of ultracold molecules in a laboratory is a space-fixed coordinate system, with the axis labeled

\mathbf{x} , \mathbf{y} and \mathbf{z} . This coordinate system is especially important for the description of external fields, which can be defined to be along one of these axes. An additional coordinate system is fixed relative to the molecule. Ignoring the small effects of the vibration of the nuclear spins, diatomic molecules can be described as rigid rotors and are cylindrically symmetric, with one of the three principal axes of inertia along the internuclear axis and the other two, with identical moments of inertia, perpendicular to the internuclear axis. These axes of inertia define a natural body-fixed coordinate system that is labeled \mathbf{a} , \mathbf{b} and \mathbf{c} , such that \mathbf{a} is along the internuclear axis. Without loss of generality, we can choose the origin of the coordinate systems to be at the same position, such they are simply rotated relative to each other. In the Born-Oppenheimer approximation, the angular momenta of the electrons are defined relative to the internuclear axis, thus we take the body-fixed coordinate system to be the unrotated one. The space-fixed coordinate system is then rotated by the Euler angles α, β, γ .

In the rigid-rotor approximation, the rotational eigenfunctions of the diatomic molecule can be determined by solving the Schrödinger equation $H_T\Psi = E_T\Psi$, with the Hamiltonian

$$H_T = \frac{\hat{\mathbf{J}}_a^2}{2I_a} + \frac{\hat{\mathbf{J}}_b^2}{2I_b} + \frac{\hat{\mathbf{J}}_c^2}{2I_c}. \quad (2.35)$$

Since the moments of inertia in the two directions perpendicular to the molecular axis are the same, the molecule can be described as a symmetric, prolate top with $I_a < I_b = I_c$ [42]. Thus, the Hamiltonian can be written as

$$H_T = \frac{\hat{\mathbf{J}}^2}{2I} + \hat{\mathbf{J}}_a^2 \left(\frac{1}{2I_a} - \frac{1}{2I} \right). \quad (2.36)$$

This Hamiltonian forms a mutually commutative set of operators with $\hat{\mathbf{J}}^2$ and the component of \mathbf{J} along the body-fixed a-axis $\hat{\mathbf{J}}_a = \partial/\partial\alpha$. Furthermore, H_T commutes with the component of \mathbf{J} along the space-fixed z-axis $\hat{\mathbf{J}}_z = \partial/\partial\phi$, due to the fact that $\hat{\mathbf{J}}_z$ acts on an angle independent of the one that $\hat{\mathbf{J}}_a$ acts upon. Thus, both the projection of \mathbf{J} along \mathbf{a} , which will be denoted with a Greek letter, Ω as well as its

projection along \mathbf{z} , which will be called M_J , are good quantum numbers. Figure 2.6 shows the orientation of \mathbf{J} relative the different axes for a symmetric top.

The set of $2J+1$ eigenfunctions of angular momentum $\Psi_{J,M}(0,0,0)$, where $(0,0,0)$ denote the Euler angles, which are all zero for the unrotated basis, can now be evaluated in the rotated coordinate system with the help of the rotation matrices [43]

$$D(\alpha, \beta, \gamma) = e^{-i\alpha\hat{J}_z} e^{-i\beta\hat{J}_y} e^{-i\gamma\hat{J}_z} \quad (2.37)$$

These matrices are unitary, $D^\dagger D = 1$. The magnitude J of the angular momentum \mathbf{J} is independent of the direction of the coordinate system. However, the value of the projection of \mathbf{J} on the \mathbf{a} axis, M depends on the direction of the coordinate system. Since both the rotated and the unrotated eigenfunctions form a complete basis, the unrotated eigenfunctions can be expressed as a superposition of the rotated eigenfunctions

$$\Psi_{J,M}(0,0,0) = \sum_{M'} \mathcal{D}_{M',M}^J(\alpha, \beta, \gamma) \Psi_{J,M'}(\alpha, \beta, \gamma), \quad (2.38)$$

where $\mathcal{D}_{M',M}^J(\alpha, \beta, \gamma)$ signify the matrix elements of the rotation matrices $D(\alpha, \beta, \gamma)$,

$$\langle J, M' | D(\alpha, \beta, \gamma) | J, M \rangle = \mathcal{D}_{M',M}^J(\alpha, \beta, \gamma). \quad (2.39)$$

Since the rotation matrices are unitary, this can be solved for the rotated wave functions $\Psi_{J,M'}(\alpha, \beta, \gamma)$,

$$\Psi_{J,M'}(\alpha, \beta, \gamma) = \sum_M \mathcal{D}_{M',M}^{J*}(\alpha, \beta, \gamma) \Psi_{J,M}(0,0,0). \quad (2.40)$$

The eigenfunctions $|J, \Omega, M_J\rangle$ of the symmetric top can now be expressed given in terms of the rotation matrix elements, $\mathcal{D}_{\Omega, M_J}^{J*}$ [44]

$$\langle \alpha, \beta, \gamma | J, \Omega, M_J \rangle = \sqrt{\frac{2J+1}{4\pi}} \mathcal{D}_{\Omega, M_J}^{J*}(\alpha, \beta, \gamma) \quad (2.41)$$

This is used for the molecular basis states for Hund's case c), as seen in Eq. (2.33).

2.3.4 Transformation between Basis States

To obtain the transformation between the Hund's case c) and e) basis states, I first transform $|FRTM_T\rangle$ into the symmetric top wave functions in the following way. First consider an uncoupled state with $|F, M_F\rangle|R, M_R\rangle$ in the space fixed basis state, which can be expressed as

$$|F, M_F\rangle_\omega |R, M_R\rangle_\omega = \sum_{\Phi, \nu} \mathcal{D}_{M_F, \Phi}^F(\omega) |F, \Phi\rangle_0 \mathcal{D}_{M_R, \nu}^R(\omega) |R, \nu\rangle_0 \quad (2.42)$$

where the coordinate system of the different states is denoted with a subscript and the Euler angles for the body-fixed coordinate system α, β, γ are abbreviated as ω , while the Euler angles for the space-fixed coordinate system are $0, 0, 0$, which is abbreviated with 0 . Using now the properties of the Y_l^m and [43, 45]

$$|R, \nu\rangle_0 = Y_R^\nu(0) = \sqrt{\frac{2R+1}{4\pi}} \delta_{\nu,0}, \quad (2.43)$$

I obtain

$$|F, M_F\rangle_\omega |R, M_R\rangle_\omega = \sum_{\Phi} |F\Phi\rangle_0 \mathcal{D}_{M_F, \Phi}^F(\omega) \mathcal{D}_{M_R, 0}^R(\omega) \sqrt{\frac{2R+1}{4\pi}}. \quad (2.44)$$

The two rotation matrix elements can be contracted to yield [43]

$$\begin{aligned} |F, M_F\rangle_\omega |R, M_R\rangle_\omega &= \sum_{\Phi} \sum_T \sqrt{\frac{2R+1}{4\pi}} \langle FM_FRM_R|TM_T\rangle \\ &\times \langle F\Phi R0|T\Phi\rangle \mathcal{D}_{M_T, \Phi}^{T*} |F\Phi\rangle_0 \end{aligned} \quad (2.45)$$

Now I want to couple $|F, M_F\rangle_\omega |R, M_R\rangle_\omega$ to $|FRT'M'_T\rangle_\omega$ via the Clebsch Gordan coefficients.

$$|FRT'M'_T\rangle_\omega = \sum_{M_F, M_R} \langle FM_FRM_R|T'M'_T\rangle |F, M_F\rangle_\omega |R, M_R\rangle_\omega. \quad (2.46)$$

Inserting Eq. (2.44) into Eq. (2.46) and using the properties of the Clebsch Gordan coefficients [45]

$$\sum_{M_F, M_R} \langle FM_FRM_R|T'M'_T\rangle \langle FM_FRM_R|TM_T\rangle = \delta_{T, T'} \delta_{M_T, M'_T} \quad (2.47)$$

I obtain

$$|(f_1 f_2) F R T M_T\rangle_\omega = \sum_{\Phi} \langle F \Phi R 0 | T \Phi \rangle \sqrt{\frac{2R+1}{4\pi}} \mathcal{D}_{M_T, \Phi}^{T*} |(f_1 f_2) F \Phi\rangle_\omega. \quad (2.48)$$

Using now the definition of the normalized eigenfunction

$$|F T \Phi M_T\rangle = \sqrt{\frac{2T+1}{4\pi}} \mathcal{D}_{M_T, \Phi}^{T*} |F \Phi\rangle, \quad (2.49)$$

analogous to Eq. (2.41), finally yields the transformation between the eigenstates along the space-fixed \mathbf{z} axis and the symmetric top eigenfunctions

$$|(f_1 f_2) F R T M_T\rangle_\omega = \sum_{\Phi} \langle F \Phi R 0 | T \Phi \rangle \sqrt{\frac{2R+1}{2T+1}} |(f_1 f_2) F T \Phi M_T\rangle_0. \quad (2.50)$$

Here the notation $(f_1 f_2) F$ serves as a reminder that in Hund's case e) the atomic angular momenta are coupled in the following way. $\mathbf{j}_1 + \mathbf{i}_1 = \mathbf{f}_1$, $\mathbf{j}_2 + \mathbf{i}_2 = \mathbf{f}_2$ and finally $\mathbf{f}_1 + \mathbf{f}_2 = \mathbf{F}$. In the extended Hund's case c) basis, on the other hand, $\mathbf{j}_1 + \mathbf{j}_2 = \mathbf{J}$, $\mathbf{i}_1 + \mathbf{i}_2 = \mathbf{I}$ and $\mathbf{I} + \mathbf{J} = \mathbf{F}$. Additionally using the fact that for alkaline-earth-like atoms $j_2 = 0$, such that $\mathbf{J} = \mathbf{j}_1$ and $\mathbf{f}_2 = \mathbf{i}_2$, the transformation between $|(f_1 f_2) F \Phi\rangle$ and $|(I J) F \Phi\rangle$ is given by a Wigner 6j symbol [45]

$$\begin{aligned} \langle (f_1 f_2) F \Phi | (I J) F' \Phi' \rangle &= \delta_{F, F'} \delta_{\Phi, \Phi'} (-1)^{j_1 + i_1 + i_2 + F} \sqrt{(2f_1 + 1)(2I + 1)} \\ &\quad \left\{ \begin{array}{ccc} j_1 & i_1 & f_1 \\ i_2 & F & I \end{array} \right\}. \end{aligned} \quad (2.51)$$

Combining Eqs. 2.33, 2.50 and 2.51 with identity

$$|J \Omega I \iota\rangle = \sum_{F \Phi} \langle F \Phi | J \Omega I \iota \rangle |F \Phi\rangle \quad (2.52)$$

finally yields the desired transformation between $|\gamma\rangle$ and $|\epsilon\rangle$

$$\begin{aligned} \langle \gamma | \epsilon \rangle &= \langle F \Phi R 0 | T \Phi \rangle \sqrt{\frac{2R+1}{2T+1}} \langle J \Omega, I \iota | F \Phi \rangle \\ &\quad (-1)^{j_1 + i_1 + i_2 + F} \sqrt{(2f_1 + 1)(2I + 1)} \left\{ \begin{array}{ccc} j_1 & i_1 & f_1 \\ i_2 & F & I \end{array} \right\}. \end{aligned} \quad (2.53)$$

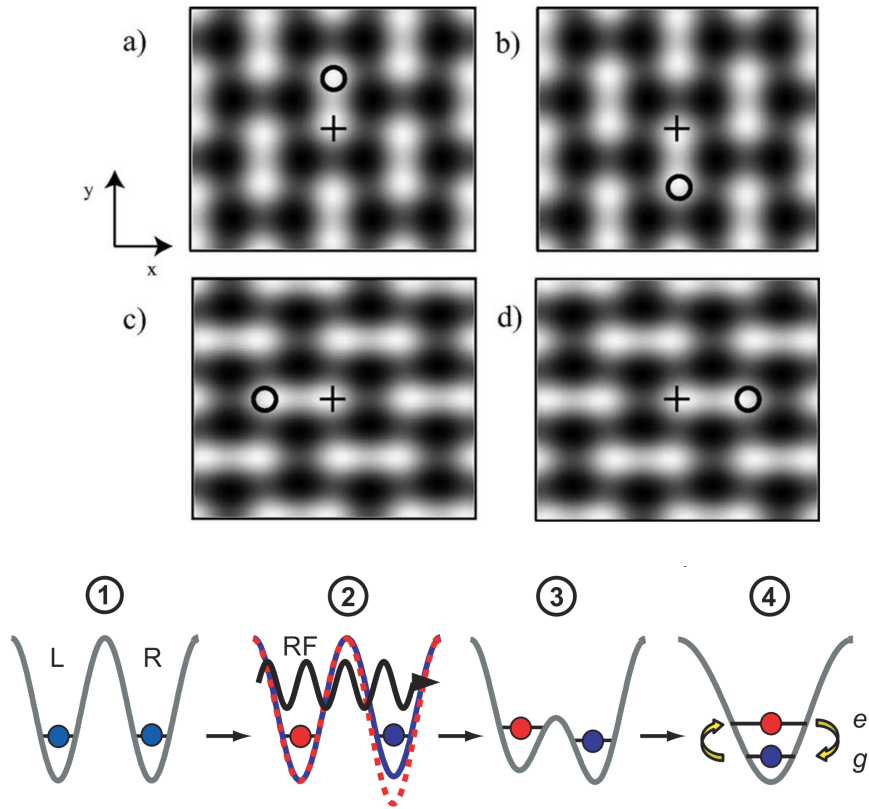


Figure 2.2: State-independent optical lattices for the manipulation of neutral atoms. Plot of flexible optical lattices used in experiments at NIST. The single wells can be transformed into double wells, a) to d) show different configurations for the different double wells. The pictures 1-4 show how two atoms in neighboring wells can be moved together in one lattice site, by first merging the two wells to a double well and then transforming the double well to a single well. Figures are taken from [38] and [14], respectively.

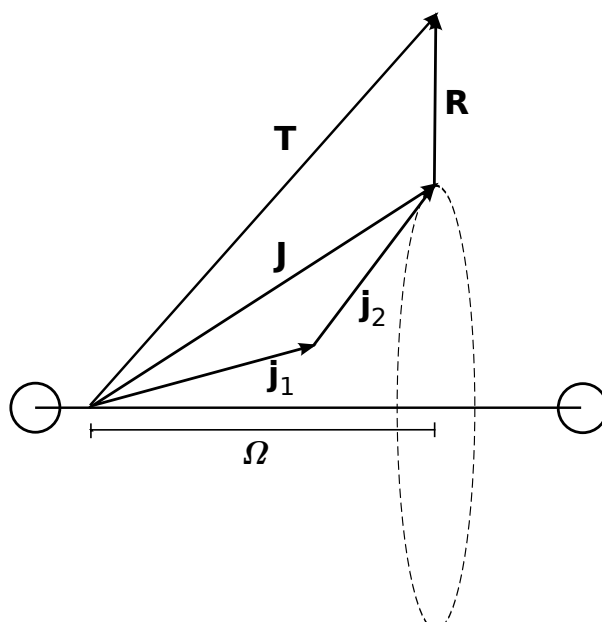


Figure 2.3: Schematics of Hund's case c) coupling. \mathbf{j}_1 and \mathbf{j}_2 are coupled to give \mathbf{J} , which precesses around the internuclear axis and couples together with \mathbf{R} to give the total angular momentum \mathbf{T} . The projection of \mathbf{J} and \mathbf{T} on the internuclear axis, Ω , is a good quantum number.

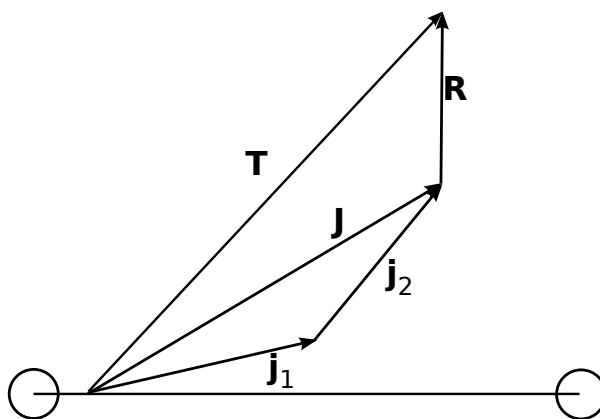


Figure 2.4: Schematics of Hund's case e) coupling. \mathbf{j}_1 and \mathbf{j}_2 are coupled to give \mathbf{J} , which couples together with \mathbf{R} to give the total angular momentum \mathbf{T} . The difference between case e) and case c) is that \mathbf{T} is not constrained to process around the internuclear axis, thus its projection Ω on the internuclear axis is not a good quantum number. However, its projection on a space fixed axis, M_T , is a good quantum number.

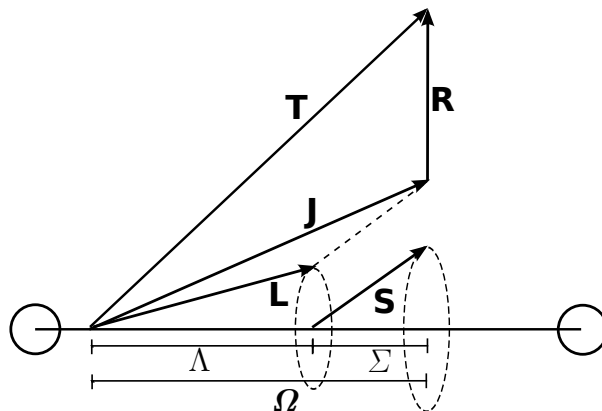


Figure 2.5: Schematics of Hund's case a) coupling. \mathbf{L} and \mathbf{S} are constrained to precess around the internuclear axis, due to the strong spin-rotation coupling. They couple together to give \mathbf{J} , which therefore also precesses around the internuclear axis and couples together with \mathbf{R} to give the total angular momentum \mathbf{T} . The projections of \mathbf{L} , \mathbf{S} , \mathbf{J} and \mathbf{T} on the internuclear axis, Λ , Σ , Ω and Ω , respectively, are all good quantum numbers.

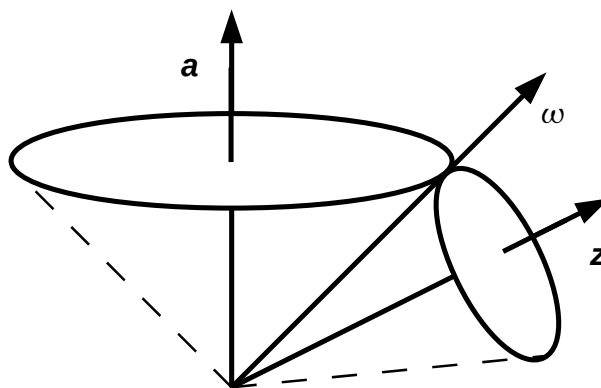


Figure 2.6: The classical motion of a prolate symmetric top, where \mathbf{a} is the body-fixed axis while \mathbf{z} denotes the space-fixed axis. The two cones rotate around each other without slipping, while the top rotates with angular momentum ω . Compare to [42].

Chapter 3

Cooling Atomic Vibration without Decohering Qubits

3.1 Theoretical Background

From the perspective of storing and manipulating quantum information, nuclear spins in atoms are attractive given their long coherence times, the mature techniques of NMR [23] and the collisional gate based on the exchange blockade as described in Section 2.2. However, as is typical in atomic quantum logic protocols, heating of atomic motion degrades performance and coherence times. Since qubits usually experience heating in the process of quantum gates, a truly scalable quantum computer, requiring many such gates necessitates the ability to recool qubits between or during quantum gates, without disturbing their coherence.

In atoms with group-I-like electronic structures, the qubits are usually stored in hyperfine levels or other electronic spin states. Therefore, laser cooling cannot be used to re-initialize atomic vibration in the course of quantum evolution because this is accompanied by optical pumping that erases the qubit stored in these internal

degrees of freedom. One must therefore resort to sympathetic cooling with another species. This cooling mechanism has been successfully used for trapped ions, in which case two or more ions (one cooling ion and one or more qubit-storing ions) are in a collective motional mode, and the cooling ion is then laser cooled. Due to the coupling of the motional mode, the qubit ion(s) are also cooled [46]. Preservation of the coherence of the qubit(s) can be achieved by either focusing the cooling beam enough to only illuminate the cooling ion, or by using another species of ions, whose cooling linewidth is sufficiently detuned from transitions in the qubit species, for the cooling ion. The lack of long range interactions in neutral atoms, while increasing their coherence times, also make this form of sympathetic cooling impossible. A way of implementing sympathetic cooling is to immerse the neutral atoms in a BEC of another species that acts as a bath, dissipating vibrational motion via the excitation of phonons [47]. However, this requires the addition and control of a BEC to the experiment, thus complicating the setup.

For alkaline-earth-like atoms, on the other hand, one can continuously refrigerate atomic motion while simultaneously maintaining quantum coherence stored in nuclear spins, as I will show in this Chapter. The proposed protocol is based on resolved-sideband laser cooling [48] of group-II-like atoms, tightly trapped in the Lamb-Dicke regime, as in optical lattices currently under consideration for next-generation atomic clocks based on optical frequency standards [49]. The cooling scheme will be explained in detail using two example species, ^{171}Yb and ^{87}Sr , both of which are actively studied in the laboratory for application to optical clocks [50, 51]. The $i = 1/2$ nucleus of ^{171}Yb is a natural qubit for storing quantum information. In the case of ^{87}Sr , whose nucleus has spin $i = 9/2$, two sublevels in the 10-dimensional manifold can be chosen to encode a qubit. Exquisite optical control of the nuclear spin of ^{87}Sr has recently been demonstrated by Boyd *et al.* [52, 24].

In order to preserve the quantum state of a qubit encoded in a nuclear spin while laser cooling, the spin coherences must be coherently transferred in both excitation

and spontaneous decay. Optical fields interacting with atoms via the electric dipole couple directly to the electrons, affecting nuclear spin states only indirectly via the hyperfine interaction. A key requirement of our protocol is, therefore, to excite states with negligible hyperfine coupling, and/or to decouple electrons from nuclear spin through the application of a sufficiently strong magnetic field that the Zeeman effect on the electrons dominates over the hyperfine interaction (Paschen-Back regime [53]). Moreover, we seek to recool atoms in traps to near the ground vibrational state which requires resolvable motional sidebands, as will be reviewed in the next section.

3.1.1 Resolved Sideband Cooling

In this section, I will give an overview of the well known [54, 55] and frequently used [56, 57] resolved sideband cooling, which is at the heart of our cooling scheme. Consider a two-level atom, that is tightly confined in a harmonic oscillator with the trap frequency ω , which is identical for both the excited state $|e\rangle$ and the ground state $|g\rangle$, achievable by trapping the atom in a deep optical lattice at the “magic wavelength”, such that the two states see the same optical potential. The overall state is then a product state between the internal state of the atom, $|g\rangle$ or $|e\rangle$, and the vibrational state of the trap, $|n\rangle$. Under the condition that $\omega \gg \Gamma$, where Γ is the linewidth of $|e\rangle$, the different vibrational states of the trap, that is the sidebands, are resolved.

Assuming a one dimensional trap and an incoming plane wave in the same direction \mathbf{x} , the overall Hamiltonian is given by

$$H = H_A + H_{AL} + H_T, \quad (3.1)$$

where H_A is the Hamiltonian describing the internal states of the two-level atom, H_{AL} is the Hamiltonian of the atom-laser interaction and H_T gives the harmonic

oscillator trap. The atomic Hamiltonian can be written as

$$H_A = \omega_g |g\rangle\langle g| + \omega_e |e\rangle\langle e| \quad (3.2)$$

Shifting the zeropoint of energy by $-\hbar(\omega_e + \omega_g)/2$, and defining $\omega = (\omega_e - \omega_g)/2$, we obtain

$$H_A = \hbar \frac{\omega}{2} (|e\rangle\langle e| - |g\rangle\langle g|) = \hbar \frac{\omega}{2} \sigma_z, \quad (3.3)$$

where σ_z is the Pauli matrix [58]. The trapping Hamiltonian is a harmonic oscillator with oscillation frequency ν , where the \hat{a} and \hat{a}^\dagger are the annihilation and creation operators for vibrational excitation in the trap,

$$H_T = \hbar \nu \left(\hat{a}^\dagger \hat{a} + \frac{1}{2} \right). \quad (3.4)$$

The incoming plane wave can be written as

$$\mathbf{E}(x, t) = E_0 \boldsymbol{\epsilon}_L \left[e^{i(k\hat{x} - \omega_L t + \phi)} + e^{-i(k\hat{x} - \omega_L t + \phi)} \right], \quad (3.5)$$

where $\boldsymbol{\epsilon}_L$ is the polarization direction of the incoming wave, while E_0 , ω_L and ϕ are its amplitude, frequency and phase. In the dipole approximation, the interaction Hamiltonian H_{AL} can then be written as $H_{AL} = -(\hat{\mathbf{d}} \cdot \boldsymbol{\epsilon}_L) E_0 [\exp(kx - \omega_L t + \phi) + c.c.]$, which can be expanded in terms of the atomic eigenstates as

$$(\hat{\mathbf{d}} \cdot \boldsymbol{\epsilon}_L) = \langle e | \hat{\mathbf{d}} \cdot \boldsymbol{\epsilon}_L | g \rangle |e\rangle\langle g| + \langle g | \hat{\mathbf{d}} \cdot \boldsymbol{\epsilon}_L | e \rangle |g\rangle\langle e| = -d_{eg} (|e\rangle\langle g| + |g\rangle\langle e|), \quad (3.6)$$

where $d_{eg} = \langle e | \hat{\mathbf{d}} \cdot \boldsymbol{\epsilon}_L | g \rangle = \langle g | \hat{\mathbf{d}} \cdot \boldsymbol{\epsilon}_L | e \rangle^* = \langle g | \hat{\mathbf{d}} \cdot \boldsymbol{\epsilon}_L | e \rangle$ is the dipole matrix element. Defining now the Rabi frequency $\Omega = 2d_{eg}E_0/\hbar$ and using the identity of the Pauli matrices, $|e\rangle\langle g| = \hat{\sigma}_+$ and $|g\rangle\langle e| = \hat{\sigma}_-$, the interaction Hamiltonian becomes

$$H_{AL} = -\frac{\hbar\Omega}{2} (\sigma_+ + \sigma_-) \left(e^{i(k\hat{x} - \phi)} e^{-i\omega_L t} + e^{-i(k\hat{x} - \phi)} e^{i\omega_L t} \right). \quad (3.7)$$

To further simplify this Hamiltonian, it is useful to go to a rotating frame, transforming the Hamiltonian with

$$\tilde{H} = \hat{D}^\dagger H \hat{D} + i\hbar \frac{\partial \hat{D}^\dagger}{\partial t} \hat{D}, \quad (3.8)$$

where $\hat{D} = \exp[-(i/\hbar)(H_T + H_A)t] = \exp[-i(\omega\sigma_z t/2 + \nu(\hat{a}^\dagger\hat{a} + 1/2))]$. For the interaction Hamiltonian, this yields

$$\begin{aligned} \tilde{H}_{AL} = D^\dagger H_{AL} D &= -\frac{\hbar\Omega}{2} e^{-i(\omega/2)\sigma_z t} (\sigma_+ + \sigma_-) e^{i(\omega/2)\sigma_z t} \\ &\times e^{(i/\hbar)H_T t} (e^{i(k\hat{x}-\phi)} e^{-i\omega_L t} + e^{-i(k\hat{x}-\phi)} e^{i\omega_L t}) e^{-(i/\hbar)H_T t}. \end{aligned} \quad (3.9)$$

Now we use that $e^{i(\omega/2)t\sigma_z}\sigma_\pm e^{-i(\omega/2)t\sigma_z} = e^{\pm i\omega t}\sigma_\pm$. Furthermore, since the atom is trapped, $\hat{x} = x_0(\hat{a} + \hat{a}^\dagger)$ and the second part of the transformation amounts to going to the Heisenberg picture with

$$e^{(i/\hbar)H_T t}\hat{a}e^{-(i/\hbar)H_T t} = \hat{a}e^{-\nu t}. \quad (3.10)$$

Therefore, the interaction Hamiltonian in the rotating frame is given by

$$\begin{aligned} \tilde{H}_{AL} = &-\frac{\hbar\Omega}{2} [\sigma_+ e^{-i(\omega-\omega_L)t} \exp[ikx_0(\hat{a}e^{(-i\nu t)} + \hat{a}^\dagger e^{(i\nu t)})] e^{-i\phi} \\ &\sigma_+ e^{-i(\omega+\omega_L)t} \exp[-ikx_0(\hat{a}e^{(-i\nu t)} + \hat{a}^\dagger e^{(i\nu t)})] e^{i\phi}] + H.c. \end{aligned} \quad (3.11)$$

The two parts of the Hamiltonian have very different resonance frequencies, the first part oscillates slowly with the detuning of the laser from the resonance frequency $\delta = \omega - \omega_L$, while the second part oscillates rapidly with $\omega + \omega_L$. In the rotating wave approximation the second part can be neglected, so that the interaction Hamiltonian finally becomes [55]

$$\tilde{H}_{AL} = \frac{\hbar\Omega}{2} \sigma_+ \exp(i\eta(\hat{a}e^{-i\omega t} + \hat{a}^\dagger e^{-i\omega t})) e^{i(\phi-\delta t)} + H.c., \quad (3.12)$$

where

$$\eta = kx_0 = \sqrt{\frac{E_R}{\hbar\nu}} \quad (3.13)$$

is the Lamb-Dicke parameter with the recoil energy $E_R = (\hbar k)^2/2m$. In the Lamb-Dicke regime, where the confinement is tight and $\eta \ll 1$, this Hamiltonian can be expanded in lowest order in η and be written in the form [55]

$$\tilde{H}_{AL} = H_{car} + H_{rsb} + H_{bsb}, \quad (3.14)$$

where the zeroth-order part of the Hamiltonian,

$$H_{car} = \frac{\hbar\Omega}{2} (\sigma_+ e^{i\phi} + \sigma_- e^{-i\phi}) \quad (3.15)$$

describes the *carrier resonance*, which couples the atomic excited and ground state to each other, without changing the vibrational frequency of the trap, $|g\rangle|n\rangle \leftrightarrow |e\rangle|n\rangle$. The first-order part of the Hamiltonian consists of two different parts, the first of which is the red sideband Hamiltonian

$$H_{rsb} = \frac{\hbar\Omega}{2} \eta (\hat{a}\sigma_+ e^{i\phi} + \hat{a}^\dagger\sigma_- e^{-i\phi}), \quad (3.16)$$

which describes transitions from ground to excited state, reduced by one quantum of vibration, $|g\rangle|n\rangle \leftrightarrow |e\rangle|n-1\rangle$. It gives rise to a resulting Rabi frequency of

$$\Omega_{n,n-1} = \Omega\eta\sqrt{n}. \quad (3.17)$$

The second first order term of the Hamiltonian is the blue sideband Hamiltonian

$$H_{bsb} = \frac{\hbar\Omega}{2} \eta (\hat{a}^\dagger\sigma_+ e^{i\phi} + \hat{a}\sigma_- e^{-i\phi}), \quad (3.18)$$

which gives rise to transitions $|g\rangle|n\rangle \leftrightarrow |e\rangle|n+1\rangle$, with a Rabi frequency of

$$\Omega_{n,n+1} = \Omega\eta\sqrt{n+1}. \quad (3.19)$$

If the Rabi frequency and the linewidth are now small enough, such that the sidebands are resolved during the excitation, $\Omega_{n,m}, \Gamma \ll \omega$, it is possible to resonantly excite the atoms on the first red sideband, $|g\rangle|n\rangle \rightarrow |e\rangle|n-1\rangle$ while not exciting the carrier or other sidebands. However, to the degree to which the system is in the Lamb-Dicke regime where $\eta \ll 1$, decay from the excited state will predominantly be on the carrier, $|e\rangle|n-1\rangle \rightarrow |g\rangle|n-1\rangle$, which is zeroth order in η . Since the resulting transition yields $|g\rangle|n\rangle \rightarrow |g\rangle|n-1\rangle$, this can be used to cool the vibrational state of the trapped atoms by repeating this cycling transition. The rate R_n for this process is found by determining the probability of the atom to be in the excited electronic state

multiplied with the decay rate. This can be calculated using the master equation in Lindblad form for the two levels of the atom, which has the following form

$$\dot{\rho} = -\frac{i}{\hbar} [H, \rho] + \mathcal{L}\rho. \quad (3.20)$$

The first part of the equation, $-\frac{i}{\hbar} [H, \rho]$ describes the unitary evolution while $\mathcal{L}\rho$ describes spontaneous emission and can be expressed as [59]

$$\mathcal{L}\rho = -\frac{\tilde{\Gamma}}{2}(\sigma_+\sigma_-\rho + \rho\sigma_+\sigma_- - 2\sigma_-\rho\sigma_+), \quad (3.21)$$

where $\tilde{\Gamma}$ is a general linewidth. Using a general Hamiltonian, similar to (3.15), but with a detuning δ and a general Rabi frequency $\tilde{\Omega}$, the resulting equations for the density matrix are

$$\dot{\rho}_{ee} = -\dot{\rho}_{gg} = -\tilde{\Gamma}\rho_{ee} + i\frac{\tilde{\Omega}}{2}\mathfrak{Im}\rho_{ge} \quad (3.22a)$$

$$\dot{\rho}_{ge} = \left(-i\delta - \frac{\tilde{\Gamma}}{2}\right)\rho_{ge} - \tilde{\Omega}(\rho_{ee} - \rho_{gg}) \quad (3.22b)$$

In the steady state, in which $\dot{\rho} = 0$, we can solve for the populations

$$\rho_{ge} = -\frac{i\tilde{\Omega}/2}{i\delta + \tilde{\Gamma}/2}(\rho_{ee} - \rho_{gg}) \quad (3.23a)$$

$$\rho_{ee} = -\frac{\tilde{\Omega}}{\tilde{\Gamma}}\mathfrak{Im}\rho_{ge} = \frac{-\tilde{\Omega}^2/4}{\delta^2 + \tilde{\Gamma}^2/2}(2\rho_{ee} - 1) = \frac{\tilde{\Omega}^2}{\tilde{\Gamma}^2 + 2\tilde{\Omega}^2 + \delta^2} \quad (3.23b)$$

For excitation on the red sideband, the general Rabi frequency $\tilde{\Omega}$ from (3.23b) becomes $\Omega_{n,n-1} = \Omega\sqrt{n}\eta$ (see Eq. (3.17)), the general linewidth $\tilde{\Gamma}$ becomes the natural linewidth of the excited state Γ , and the detuning $\delta = 0$. Therefore, the rate R_{cool} for this process is given by

$$R_{cool} = \tilde{\Gamma}\rho_{ee} = \Gamma\frac{\Omega_{n,n-1}^2}{\Gamma^2 + 2\Omega_{n,n-1}^2} = \Gamma\frac{\Omega^2 n \eta^2}{\Gamma^2 + 2\Omega^2 n \eta^2} \approx \frac{\Omega^2 n \eta^2}{\Gamma}. \quad (3.24)$$

It can be seen that the ground vibrational state is a dark state.

Heating of the ground state is possible in two different ways, the first of which is off-resonant excitation ($\delta = \omega$) on the carrier with $\tilde{\Omega} = \Omega_{0,0}$, followed by decay

on the blue sideband. Since this decay changes the vibrational state of the atom, the linewidth is reduced by the square of the Lamb-Dicke factor and is therefore $\tilde{\Gamma} = \tilde{\eta}^2\Gamma$ (where $\tilde{\eta}$ is the Lamb-Dicke parameter for decay, slightly different from η for geometrical reasons [55]). Again using $R = \Gamma\rho_{ee}$, the rate for this heating process is

$$R_{heat,1} = \tilde{\Gamma} \frac{\Omega_{0,0}^2}{\tilde{\Gamma}^2 + 2\Omega_{0,0}^2 + 4\delta^2} \approx \tilde{\eta}^2\Gamma \frac{\Omega^2}{4\omega^2}. \quad (3.25)$$

The other heating process is off-resonant excitation ($\delta = 2\omega, \tilde{\Omega} = \Omega_{0,1}$) on the blue sideband and decay on the carrier, for which the rate is [55]

$$R_{heat,2} = \Gamma \frac{\Omega_{0,1}^2}{\Gamma^2 + 2\Omega_{0,1}^2 + 4\delta^2} \approx \Gamma \frac{(\eta\Omega)^2}{4(2\omega)^2}. \quad (3.26)$$

All other heating mechanisms are of higher order in the Lamb-Dicke parameter and can therefore be neglected. Since the overall heating rate $R_{heat} = R_{heat,1} + R_{heat,2}$, the resulting rate equations for the ground and first excited vibrational state are given by

$$\dot{p}_0 = p_1 R_{cool} - p_0 R_{heat} = p_1 \frac{(\eta\Omega)^2}{\Gamma} - p_0 \left[\left(\frac{\Omega}{2\omega} \right)^2 \tilde{\eta}^2\Gamma + \left(\frac{\eta\Omega}{4\omega} \right)^2 \Gamma \right], \quad (3.27)$$

$$\dot{p}_1 = -\dot{p}_0.$$

This results in an average excitation number of

$$\langle n \rangle \approx p_1 \approx \left(\frac{\Gamma}{2\omega} \right)^2 \left[\left(\frac{\tilde{\eta}}{\eta} \right)^2 + \frac{1}{4} \right], \quad (3.28)$$

assuming the system to be in steady state and using $\omega \gg \Gamma$. The factor in brackets is of order one. Eq.(3.28) shows that resolved sideband cooling can lead to very low temperatures for forbidden lines, which will be used in the cooling scheme.

3.2 Description of the Proposed Cooling Scheme

The dual requirement of very narrow linewidths and small hyperfine coupling leads us to consider cooling on the weakly allowed intercombination “clock” transition $^1S_0 \rightarrow$

3P_0 in a “magic wavelength” optical lattice [49]. Cooling to the ground vibrational state can proceed by coherent excitation of a π pulse on the first red sideband, $|^1S_0, n\rangle \rightarrow |^3P_0, n-1\rangle$, where n is the vibrational quantum number, followed by recycling to the ground state with Lamb-Dicke suppression of recoil.

3.2.1 Resolved Sideband Cooling on the Clock Transition

Our concern is to carry out this cooling while maintaining nuclear spin coherence. To good approximation, the 3P_0 state has total electron angular momentum $j = 0$, and under this condition, there is no interaction between electrons and nuclear spin, as in the ground state, $|^1S_0\rangle$. However, the clock transition is $j = 0 \rightarrow j = 0$, and laser excitation is only allowed because in the excited state, the hyperfine interaction leads to a small admixture of the higher-lying P states as described in 1.3. The nuclear spin projection m_i is thus not an exact quantum number for the magnetic sublevels in $|^3P_0\rangle$; a very small admixture of electronic angular momentum renders m_f a good quantum number. This leads to two effects which we must address in the context of transferring the nuclear spin state. While the clock transition is only allowed due to the hyperfine interaction, it is still the case that the sublevels of $|^3P_0\rangle$ are almost pure m_i , and a π -polarized pulse will preserve nuclear spin projections in excitation on the clock transition [24]. More importantly, even a small admixture of electron angular momentum can strongly affect the magnetic moment, so that the g -factor of the excited state differs from that of the ground state [52]. This implies that in a bias magnetic field, the π -transitions $|^1S_0, n\rangle \otimes |m_i\rangle \rightarrow |^3P_0, n-1\rangle \otimes |m_f = m_i\rangle$ will have different resonant frequencies for different values of m_i . The protocol for the transfer of nuclear spin coherence from the ground state to the clock state will thus depend on the details of the experimental conditions, i.e., the relative size of the differential Zeeman splitting in the given bias field when compared to the vibrational spacing in the trap. Under any operating condition, these coherences can be transferred due to the extremely narrow linewidth of the clock transition, be it through sequential

addressing of each sublevel in a series of narrow band pulses [52], or in a short pulse that does not resolve the differential Zeeman shift but does resolve the sidebands. Finally, in this step, one must also take into account that the differential g -factor leads to differential relative phases between the sublevels; this is a unitary transformation which can be reversed.

Once the atom is transferred to the clock state 3P_0 , the cooling cycle must be completed through a spontaneous event that returns the atom to its ground electronic state 1S_0 , with Lamb-Dicke suppression of recoil. Of importance in our protocol is that this occurs without decoherence of the nuclear spin state. The key requirement for spontaneous transfer of coherences is that the decay paths of the different sublevels are *indistinguishable*, i.e. the decay channels cannot be distinguished by their polarization or frequency. Under circumstances in which the nuclear spin and electronic degrees of freedom of an excited state are decoupled (no hyperfine interaction), in a product state with zero projection of electron angular momentum, $|e\rangle \approx |i, m'_i\rangle \otimes |j', m'_j = 0\rangle$, all decay channels to the ground state are indistinguishable. To see this, note that the selection rules dictate that the electric dipole matrix element satisfies, $\langle e|d_q|g\rangle = \langle j', m'_j = 0|d_0|j = 0, m_j = 0\rangle \delta_{q,0} \delta_{m_i, m'_i}$. Only π -transitions are allowed and all decay channels have the same polarization without change of nuclear spin projection. Moreover, in the $m'_j = 0$ manifold, the g -factor is solely nuclear, g_I , equivalent to that in the ground state. Thus, the Zeeman splitting in excited and ground states will be equal and decay channels will not be distinguished by frequency. Deviations of the excited state from a nuclear-electron product state (due to residual hyperfine interaction) will lead to decoherence when there are nuclear spin changing decays (polarization distinguishable) and/or when the different channels are frequency resolvable (i.e. have a frequency difference that is not negligible compared to the decay linewidth).

In the case of the clock state 3P_0 , spontaneous decay is completely due to the admixture of higher P states and the decay channels with different polarizations

occur with a probability proportional to the respective Clebsch Gordan coefficients. Therefore, the nuclear spin is not preserved during spontaneous decay. Moreover, the long lifetime makes the cooling cycle too long for practical purposes. We thus consider quenching the clock state by pumping to the short lived 1P_1 state (see Fig. 3.2) [60, 61]. This level decays with very high probability to the ground state 1S_0 and has a very broad linewidth, $\Gamma/(2\pi) > 10$ MHz. Direct excitation $^3P_0 \rightarrow ^1P_1$, is weakly magnetic-dipole-allowed, and has been considered in the context of electromagnetically induced transparency [26]. Alternatively, we can quench the clock state via a two-photon $^3P_0 \rightarrow ^3S_1 \rightarrow ^1P_1(m_j = 0)$ transition, off resonance from the intermediate state. This has the advantage that, though one leg is an intercombination line, all transitions are electric-dipole allowed, leading to larger depopulation rates for the same intensity.

3.2.2 Quenching of a Metastable State via a Rapidly Decaying State

For the aforementioned reasons, the proposed cooling scheme requires quenching with a rapidly decaying state. Therefore, in this section, I will discuss different schemes to quench a metastable excited state $|2\rangle$ with a rapidly decaying excited state $|3\rangle$, which has a very large decay rate Γ and decays only to the ground state $|1\rangle$. The energy of state $|i\rangle = \hbar\omega_i$, where the ground state energy is set to zero, $\omega_1 = 0$. For our purposes, $|1\rangle = |^1S_0\rangle$, $|2\rangle = |^3P_0\rangle$ and $|3\rangle = |^1P_1\rangle$. There are two different ways of achieving quenching, one can either dress the metastable state via a continuous-wave laser with the excited state $|3\rangle$, thus broadening its lifetime, or one can coherently transfer the population from $|2\rangle$ to $|3\rangle$ and let $|3\rangle$ decay back to the ground state. Here I want to elucidate these different schemes if the Rabi frequency Ω with which we can couple $|2\rangle$ and $|3\rangle$ is small compared to Γ , and to estimate required intensities for implementation of the processes.

Continuous wave

Consider the excited subspace consisting of states $|2\rangle$ and $|3\rangle$, which are magnetic-dipole coupled to each other with a laser resulting in the Rabi frequency $\Omega = |\langle 3|\hat{\mu}|2\rangle|B_0/\hbar$, where B_0 is the magnetic field and $\hat{\mu}$ is the magnetic dipole moment. For Sr, $\hat{\mu} = 0.022\mu_B$ [26], while the value for Yb has not been determined, but is expected to be of similar magnitude. The Hamiltonian of this system in the rotating frame, after applying the rotating wave approximation is similar to the Hamiltonian for the carrier, Eq. (3.15)

$$H = \frac{\hbar\Omega}{2} (\sigma_+ e^{i(\phi-i\delta)t} + \sigma_- e^{-i(\phi-\delta)t}). \quad (3.29)$$

where δ is the detuning of the dressing laser. Following [26], the resulting equations of motion are

$$\dot{c}_2(t) = -\frac{i\Omega}{2} e^{i\delta t} c_3(t) \quad (3.30a)$$

$$\dot{c}_3(t) = -\frac{i\Omega}{2} e^{i\delta t} c_2(t) - i\frac{\Gamma}{2} c_3(t), \quad (3.30b)$$

This causes some admixture of the state $|3\rangle$ to $|2\rangle$ and conversely, the state $|2\rangle$ is dressed with the state $|3\rangle$. In leading order in $\Omega/(\delta + i\Gamma/2)$ this gives

$$|\tilde{2}\rangle = [|2\rangle e^{-i\omega_2 t} + b|3\rangle e^{-i(\omega_3+\delta)t}] e^{-i\beta t} \quad (3.31)$$

with $b = \frac{\Omega}{2(\delta+i\Gamma)}$ and $\beta = \frac{1}{2}\Omega b$. On resonance with $\delta = 0$, the decay rate of $|\tilde{2}\rangle$ is

$$\tilde{\Gamma} = \frac{\Omega^2}{\Gamma}. \quad (3.32)$$

Assuming a linewidth of $\Gamma/(2\pi) = 28$ MHz for the excited state, an intensity of $I = 1.1\text{kW}/\text{cm}^2$ is required to achieve a effective decay rate of $\tilde{\Gamma} = 1$ kHz, fast compared to the coherence times of nuclear spins of alkaline-earth-like atoms, which can be up to a second [52].

Note that $\tilde{\Gamma}$ is inversely proportional to Γ , so the faster $|3\rangle$ decays, the smaller the resulting linewidth of the dressed state. This is an example of the Zeno effect,

in that the decay of $|3\rangle$ probes whether or not the population from state $|2\rangle$ was pumped out [62]. Therefore, quenching via states with smaller linewidths can be advantageous under certain circumstances.

Pulsed scheme

An alternative approach to quenching is to use pulses of light to transfer the population from the metastable state to the rapidly decaying state. Here I will examine a scheme where we have several pulses with duration $\tau_1 < 1/\Gamma$ separated by a time $\tau_2 > 1/\Gamma$ to answer the question whether it is possible to achieve a higher pumpout rate than with a cw pulse with duration t , assuming that the energy input of the laser is held constant. To this end, I use again the master equation in Lindblad form, given in Eq. (3.20).

In this case, we assume that there is no coupling between states $|3\rangle$ and $|1\rangle$, which is a good approximation, given that $\Gamma = \Gamma_3$ is six orders of magnitude bigger than Γ_2 . Furthermore, $|3\rangle$ also decays predominantly to $|2\rangle$ and we ignore spontaneous decay from $|3\rangle$ to $|2\rangle$, such that $\sigma_+ = |3\rangle\langle 1|$. The Hamiltonian that governs the dynamics of this process is given in (3.29). Putting this all together yields the following set of coupled differential equations for the relevant populations and coherences of the density matrix

$$\dot{\rho}_{11} = \Gamma\rho_{33} \tag{3.33a}$$

$$\dot{\rho}_{22} = \Omega\mathfrak{Im}(\rho_{23}) \tag{3.33b}$$

$$\dot{\rho}_{33} = -\Omega\mathfrak{Im}(\rho_{23}) - \Gamma\rho_{33} \tag{3.33c}$$

$$\dot{\rho}_{23} = \frac{i\Omega}{2}(\rho_{33} - \rho_{22}). \tag{3.33d}$$

For small times τ this can simply be integrated to give

$$\rho_{11} = \Gamma\tau\rho_{33} \quad (3.34a)$$

$$\rho_{22} = \Omega\tau\mathfrak{Im}(\rho_{23}) + \rho_{22}(0) = \Omega\tau\mathfrak{Im}(\rho_{23}) + 1 \quad (3.34b)$$

$$\rho_{33} = -\Omega\tau\mathfrak{Im}(\rho_{23}) - \Gamma\tau\rho_{33} \quad (3.34c)$$

$$\rho_{23} = \frac{i\Omega\tau}{2}(\rho_{33} - \rho_{22}), \quad (3.34d)$$

where $\rho_{22}(0) = \rho_{33}(0) = 0$. For small τ most of the population is still in the metastable state, $\rho_{22} \approx 1$ and $\rho_{22} \gg \rho_{33}$, as can be seen by solving for these populations, which leads to

$$\rho_{11} = \Gamma\Omega^2\tau^3 \quad (3.35a)$$

$$\rho_{22} = 1 - \Omega^2\tau^2. \quad (3.35b)$$

We assume that the time for the experiment $t \gg \tau_2 \gg \tau_1$, such that there will be many pulses that transfer population. The original intensity is I_0 , the intensity of the short pulses is then $I_1 = (\tau_1 + \tau_2)/\tau_1 I_0$. The Rabi frequency scales with the square root of the intensity, therefore the Rabi frequency for the pulses is given by $\Omega_1 = \sqrt{(\tau_1 + \tau_2)/\tau_1} \Omega$. The population which is pumped out of ρ_{22} with $n = t/(\tau_1 + \tau_2)$ pulses is $\rho_{22}(0)(1 - c)^n = (1 - c)^n$. According to the equations above c is given by $\Omega_1^2\tau_1^2 = \Omega^2\tau_1^2(\tau_1 + \tau_2)/\tau_1 \approx \Omega^2\tau_1\tau_2$. For small τ_1 it follows that $n \approx t/\tau_2$. Putting it all together gives

$$\rho_{22}(t) \approx (1 - \Omega^2\tau_1\tau_2)^{t/\tau_2}. \quad (3.36)$$

It can be seen that for $\tau_1 \rightarrow 0$ all the population stays in the ρ_{22} state. Therefore, using a pulsed scheme to pump the population out of the metastable state does not necessarily improve the decay rate if $\Gamma \gg \Omega$, as long as the intensity times the time of the pulses is held constant.

3.2.3 Decoupling the Nuclear Spin from the Electronic Degrees of Freedom in the Quenching Process

In order to obtain the product states of nuclear-electron spin degrees of freedom in 1P_1 as required for preserving nuclear spin coherence, we employ a magnetic field. The 1P_1 subspace is then governed by the Hamiltonian including Zeeman interaction, magnetic spin coupling and quadrupole effects,

$$\begin{aligned} \hat{H} = A\hat{\mathbf{i}} \cdot \hat{\mathbf{j}} + Q \frac{3(\hat{\mathbf{i}} \cdot \hat{\mathbf{j}})^2 + 3/2\hat{\mathbf{i}} \cdot \hat{\mathbf{j}} - i(i+1)j(j+1)}{2ij(2i-1)(2j-1)} \\ + g_J\mu_B\hat{\mathbf{j}} \cdot \mathbf{B} - g_I\mu_N\hat{\mathbf{i}} \cdot \mathbf{B}, \end{aligned} \quad (3.37)$$

where g_J and g_I are the relevant electron and nuclear g -factors. If now the energy shift due to the magnetic field is large compared to the hyperfine splitting, such that we are in the Paschen-Back regime, m_i and m_j become good quantum numbers once again. The magnetic hyperfine constants are $A/h = -216$ Mhz and $A/h = -3.4$ MHz for ^{171}Yb and ^{87}Sr respectively [52, 24, 63].

For ^{171}Yb , because $i = 1/2$, the quadrupole constant $Q = 0$ and we can analytically solve for the energy spectrum and eigenstates. By using $A\hat{\mathbf{j}} \cdot \hat{\mathbf{i}} = A((\hat{i}_+\hat{j}_- + \hat{i}_-\hat{j}_+)/2 + \hat{i}_z\hat{j}_z)$, it can be seen that the above Hamiltonian is blockdiagonal in the basis $|i = 1/2, m_i = 1/2, j, m_f + 1/2\rangle, |i = 1/2, m_i = -1/2, j, m_f - 1/2\rangle$ and the blocks with constant m_f can be written as

$$\begin{pmatrix} \frac{A}{2}(m_{f-} + B[g_J\mu_B(m_{f-}) - \frac{1}{2}g_I\mu_N]) & \frac{A}{2}\sqrt{j(j+1) - m_{f+}m_{f-}} \\ \frac{A}{2}\sqrt{j(j+1) - m_{f+}m_{f-}} & -\frac{A}{2}(m_{f+}) + B[g_J\mu_B(m_{f+}) + \frac{1}{2}g_I\mu_N] \end{pmatrix}, \quad (3.38)$$

where $m_{f\pm} = m_f \pm 1/2$. Solving these blocks leads to a modified Breit-Rabi formula,

$$E_{m_j, m_i}(B) = -\frac{E_{\text{HF}}}{2(2j+1)} + g_J\mu_B B m_f \pm \frac{E_{\text{HF}}}{2} \sqrt{1 - \frac{4m_f x}{2j+1} + x^2}, \quad (3.39)$$

where $x = (g_I\mu_B + g_J\mu_N)B/E_{\text{HF}}$, $m_f = m_i + m_j$ and $E_{\text{HF}} = A(j + 1/2)$. This differs from the standard Breit-Rabi formula, in which $j = 1/2$ and i is arbitrary, in that i is replaced by j and the second term as well as the second term in the square root have opposite signs. The resulting Zeeman diagram can be seen in Fig. 3.3. The eigenstates are specified by

$$|m_f\rangle = \sum_q c_{q,m_f} |m_i = m_f - q\rangle |m_j = q\rangle, \quad (3.40)$$

for $q = 0, 1, -1$, with field dependent expansion coefficients c_{q,m_f} . For high magnetic fields, in the subspace of interest, $c_{0,m_f} \rightarrow 1$, as can be seen in Fig. 3.4, and the states are in a product state $|m_i\rangle \otimes |m_j = 0\rangle$. Deviations from this limit lead to the residual differential g -factor.

Since ^{87}Sr has a large quadrupole constant $Q/h = 39$ MHz [64], the Breit-Rabi formula does not apply. Diagonalizing Eq. (3.37) numerically gives the Zeeman diagram shown in Fig. 3.3 (for an analytic form, see [24]). Each of the three subspaces for $m_j = 1, 0, -1$ consists of 10 sublevels which asymptote to the $2i + 1$ projections associated with the nuclear spin of this isotope, $i = 9/2$. For fields of order 10 mT or greater the Zeeman effect dominates over the hyperfine coupling and the sublevels approach product states of electron and nuclear spin. However, the residual quadrupole interaction leads to a complex spectrum that is not described by a linear Zeeman shift with an effective g -factor. For B-fields between 50 and 120 mT, the subspace with $m_j=0$ is nearly flat. Additionally, due to the quadrupole symmetry, the states with equal $|m_i|$ are paired and very close in energy (less than 2 MHz), whereas the energy splitting between the pairs is on the order of tens of megahertz, nearly as big as the linewidth. Given the near degeneracy of the sublevels $\pm m_i$, we will consider preserving nuclear spin coherence in a qubit encoded in one of these two-dimensional subspaces, thereby ensuring that the frequencies of the different decay channels are not resolvable.

3.3 Results

In the following, I quantitatively study the transfer of nuclear spin-coherence via spontaneous emission. Consider a qubit in the excited state $\alpha|e, \uparrow\rangle + \beta|e, \downarrow\rangle$ which decays to the ground state $|g\rangle$. We wish to transfer the qubit into the superposition $\alpha|g, \uparrow\rangle + \beta|g, \downarrow\rangle$. Here $|e, \uparrow(\downarrow)\rangle = |^1P_1, m_f = \pm m_i\rangle$ and $|g, \uparrow(\downarrow)\rangle = |^1S_0, \pm m_i\rangle$. The evolution of the atom can be described by a master equation in Lindblad form,

$$\dot{\rho} = -\frac{i}{\hbar}[H, \rho] - \frac{1}{2} \sum_q (L_q^\dagger L_q \rho + \rho L_q^\dagger L_q - 2L_q \rho L_q^\dagger), \quad (3.41)$$

where

$$L_q = \sqrt{\Gamma} \sum_{m_f} c_q(m_f) |g, m_i = m_f - q\rangle \langle e, m_f| \quad (3.42)$$

(with c_q defined above in (3.40)) are the “jump operators” for the spontaneous emission of a photon with polarization π, σ^+, σ^- , ($q = 0, +1, -1$). Spin coherences, described by off-diagonal matrix elements, satisfy

$$\dot{\rho}_{\uparrow, \downarrow}^{(e)} = (-i\Delta_e - \Gamma)\rho_{\uparrow, \downarrow}^{(e)} \quad (3.43a)$$

$$\dot{\rho}_{\uparrow, \downarrow}^{(g)} = -i\Delta_g \rho_{\uparrow, \downarrow}^{(g)} + \Gamma' \rho_{\uparrow, \downarrow}^{(e)} \quad (3.43b)$$

where $\Delta_{e(g)}$ are the Zeeman splittings of the excited and ground qubits and $\Gamma' = \Gamma c_0(m_f)c_0(-m_f)$. Solving for the ground state coherences in the limit $t \gg 1/\Gamma$, when all population and coherence resides in the ground states,

$$\rho_{\uparrow, \downarrow}^{(g)}(t) = \rho_{\uparrow, \downarrow}^{(e)}(0) \frac{\Gamma'}{\Gamma - i\delta} e^{i\Delta_g t}, \quad (3.44)$$

where $\delta = \Delta_g - \Delta_e$ is the differential energy shift. The parameters δ and $\Gamma' - \Gamma$ are functions of applied magnetic field, both approaching zero in the perfect Paschen-Back limit. For finite fields, imperfect decoupling of electron and nuclear spin results in imperfect transfer of coherences, characterized by the “fidelity”

$$\mathcal{F} = |\rho_{\uparrow, \downarrow}^{(g)}(t)|^2 / |\rho_{\uparrow, \downarrow}^{(e)}(0)|^2 = \Gamma'^2 / (\Gamma^2 + \delta^2). \quad (3.45)$$

The resulting transfer of coherence as a function of the magnetic field can be seen in Fig. 3.5. For ^{171}Yb , a magnetic field of 1 T is required to reach a fidelity of 99%, whereas for the $\pm m_i$ qubit in ^{87}Sr a magnetic field of order 10 mT is sufficient to obtain this threshold.

Relatively large vibrational frequencies of $\nu/2\pi = 90(260)$ kHz have already been realized for Yb (Sr) in an optical lattice in 1D [25, 65]. In principle, given these tight confinements and the tiny linewidth Γ of the clock transition (few mHz), the motional sidebands are very well resolved, and extremely cold temperatures can be reached with a steady state mean vibrational excitation on the order of $\langle n \rangle \approx \Gamma^2/(2\nu)^2 = 10^{-15} (10^{-18})$ [48]. Of course, the true achievable temperature will depend strongly on the suppression of the different heating mechanisms.

Although I have argued throughout this chapter that one needs to decouple nuclear and electronic degrees of freedom in order to preserve nuclear spin coherence during laser cooling, we still require an interaction that allows for final readout of the nuclear spin state via resonance fluorescence. Consider first ^{171}Yb . According to Eq. (3.37), the splitting between the $|m_j, m_i = \pm 1/2\rangle$ states is given by $\Delta E = g_I \mu_N B + A m_j$, where A is the hyperfine constant for the 1P_1 state. Given ^{171}Yb in a magnetic field of 1 T, the splitting between the $|m_j \neq 0, m_i = \pm 1/2\rangle$ states is on the order of 200 MHz. The splitting between $|\uparrow\rangle$ and $|\downarrow\rangle$ in the 1S_0 ground state arises solely due to the Zeeman interaction with the nuclear spin, equal to 7 MHz for the applied field ($g_I \approx 1$). The higher the magnetic field, the closer $g_I \mu_N B$ is to $A m_j$ and the closer the different splittings are to each other. However, due to the big hyperfine interaction of ^{171}Yb , huge magnetic fields of tens of T are required for the two terms to be of the same order. Even more importantly for the purposes of the readout, the large hyperfine constant causes the difference in the splittings to be much bigger than the linewidth Γ of the transition. This makes it possible to selectively drive the transition $|^1S_0, m_i = +1/2\rangle \rightarrow |^1P_1, m_j = -1, m_i = +1/2\rangle$ as shown in Fig. 3.2 for readout. Furthermore, the states with different m_i are decoupled due

to the magnetic field, as can be seen in Fig. 3.4, thus making a decay process which switches the sign of m_i very unlikely, as in the cooling process. It follows that many fluorescence cycles can be realized before the nuclear spin of the atom is flipped, allowing for readout on this line.

For ^{87}Sr in a magnetic field of few mT, the splitting between neighboring substates in $m_j = \pm 1$, dominated by the hyperfine interaction, is on the order of the linewidth and therefore not well resolved. Thus we cannot selectively excite a given m_i level in the same way as described for ^{171}Yb , since invariably both nuclear spin polarizations that form the basis of the qubit would be excited. We can, however, take advantage of the difference in the g-factors of the 1S_0 and 3P_0 states in Sr in order to manipulate population in the individual magnetic sublevels. Consider a robust control pulse that transfers all population from 1S_0 to 3P_0 level. The difference in Zeeman splitting implies that a narrow-band π -pulse can selectively return population in a chosen m_i level to the ground state, leaving the remaining sublevels shelved in the metastable clock state. The occupation of level m_i can then be probed via fluorescence on the $^1S_0 \rightarrow ^1P_1$ transition. The procedure of shelving and activating the state of interest m_i , thus allows us to sequentially measure population in each sublevel.

3.4 Fluorescence while Preserving Nuclear Spin Coherences

In the resolved sideband cooling scheme discussed above, a large magnetic field caused decoupling between the nuclear spin and the electronic degrees of freedom that were optically pumped in the process, thus preserving the coherence of the nuclear spins. However, it is also possible to achieve effective decoupling by virtual coupling to the excited state using a detuning Δ , which is large compared to the hyperfine splitting, $\Delta \gg \delta E_{HF}$. In this case, the hyperfine splitting is not resolved and thus the photon

scattering is completely elastic, not causing any decoherence, as will be described in the next paragraph. The disadvantage of this approach is the high intensity required to excite with a detuning large compared to the hyperfine splitting. This is especially pronounced for ^{171}Yb , with its large hyperfine splitting. It is also possible to combine magnetic fields and large detuning to achieve nuclear-spin preserving scattering with much more relaxed requirements on both the intensity and the required magnetic fields, as will be shown in this section. This is particularly true when working on the strong $^1S_0 \rightarrow ^1P_1$ transition, where off resonance excitation can still lead to rapid scattering rates. If one is interested solely in fluorescence of the excited state, eg. for electronic qubit detection, rather than cooling, such an approach will be useful. This would for example be the case in the proposal by Gorshkov [66]. The proposal elucidated here was developed in discussions between S. Rolston from the University of Maryland and the Joint Quantum Institute (JQI), J. V. Porto from NIST and the JQI and my advisor I. H. Deutsch and me.

Consider first off-resonant scattering from an excited hyperfine manifold in the absence of a magnetic field. To find the scattering rate corresponding to absorption of a laser photon followed by spontaneous emission between magnetic sublevels within one hyperfine manifold, we use the Kramers-Heisenberg formula

$$\gamma_{fm_1 \rightarrow fm_2} = \frac{\Omega^2 \Gamma}{4} \sum_q \left| \sum_{f'} o_{j'f'jf} \frac{\langle fm_2 | (\mathbf{e}_q^* \cdot \mathbf{D}_{f'f}) (\boldsymbol{\epsilon} \cdot \mathbf{D}_{ff}^\dagger) | fm_1 \rangle}{\Delta_{f'f} - i\Gamma/2} \right|^2. \quad (3.46)$$

As usual, Ω is the Rabi frequency, Γ is the linewidth of the excited state and q is the angular momentum of the photon. Furthermore, $\boldsymbol{\epsilon}$ and \mathbf{e} are the polarization of the laser photon and the spontaneously emitted photon, respectively, while

$$\mathbf{D}_{f'f}^\dagger = \sum_{q,mf} \mathbf{e}_q^* \langle f'm_f + q | fm_f; 1q \rangle | f'm_f + q \rangle \langle fm_f | \quad (3.47)$$

is the raising operator for the absorption of one photon, and

$$o_{j'f'jf} = (2j' + 1)(2f + 1) \left| \left\{ \begin{array}{ccc} f' & i & j' \\ & j & 1 & f \end{array} \right\} \right|^2 \quad (3.48)$$

is the relative oscillator strength for the different $f \rightarrow f'$ transitions, with the six-j symbol $\{\dots\}$. For ^{171}Yb , $o_{1,1/2,0,1/2} = o_{1,1/2,0,3/2} = 1$. Since we want to preserve the direction of the nuclear spin and avoid decoherence, only π -polarized light with $q = 0$ is used for the excitation, however, spontaneous decay can be either via π, σ^+ or σ^- light, yielding the scattering rates

$$\gamma_{fm \rightarrow fm-q} = \frac{\Omega^2 \Gamma}{4} \left| \sum_{f'} \frac{\langle f'm | fm - q; 1q \rangle \langle f'm | fm; 10 \rangle}{\Delta_{f'f} - i\Gamma/2} \right|^2. \quad (3.49)$$

Inserting the numerical value of the respective Clebsch-Gordan coefficients yields explicit expressions for spin preserving and spin flipping transitions for Yb,

$$\gamma_{1/2 \rightarrow 1/2} = \frac{\Omega^2 \Gamma}{4} \left| \frac{1}{3(\Delta - i\Gamma/2)} + \frac{2}{3(\Delta - \delta E_{HF} - i\Gamma/2)} \right|^2 \quad (3.50a)$$

$$\gamma_{1/2 \rightarrow -1/2} = \frac{\Omega^2 \Gamma}{4} \left| \frac{-\sqrt{2}}{3(\Delta - i\Gamma/2)} + \frac{\sqrt{2}}{3(\Delta - \delta E_{HF} - i\Gamma/2)} \right|^2. \quad (3.50b)$$

Here, Δ is the detuning of the laser from the $f' = 1/2$ state, while $\delta E_{HF} \approx 300$ MHz for the 1P_1 state of ^{171}Yb , denotes the splitting between the different hyperfine states. Thus, for detuning large compared to the hyperfine splitting, the resulting scattering rates go to

$$\gamma_{1/2 \rightarrow 1/2} \rightarrow \frac{\Omega^2 \Gamma}{4} = \gamma_s \quad (3.51a)$$

$$\gamma_{1/2 \rightarrow -1/2} \rightarrow 0, \quad (3.51b)$$

where γ_s is the scattering rate for unit oscillator strength. The equations for $m = -1/2$ differ only by a sign, yielding the same results for large detuning. Therefore, as stated before, in the limit of large detuning, coherences are preserved.

In the presence of an intermediate magnetic field, both the energy splitting between the different states as well as their composition changes. As can be seen in the Breit-Rabi diagram, Fig. 3.3, the states that approach the $|m_j = 0\rangle \otimes |m_i\rangle$ states in the Paschen-Back regime, are separated by an energy much smaller than the bare hyperfine splitting, even for relatively small magnetic fields. Now the laser can be

tuned relatively close to this manifold, but still with a detuning large compared to the splitting between the two states, and with a much larger detuning to the other manifolds with different m_j . Excitation to the states in other manifolds is then negligible. Thus, the detuning required to preserve nuclear-spin coherences is much smaller in the presence of magnetic fields, as is the required intensity for a given scattering rate. Note that the scattering rates in the presence of a magnetic field deviate from (3.49), in that the Clebsch-Gordan coefficients in the nominator are replaced by the c-factors from Eq. (3.40), such that Eqs. (3.50a) and (3.50b) become

$$\gamma_{1/2 \rightarrow 1/2} = \frac{\Omega^2 \Gamma}{4} \left| \frac{c_{0,1/2} c_{0,1/2}}{\Delta_{1/2,0}(B) - i\Gamma/2} + \frac{c_{-1,1/2} c_{-1,1/2}}{\Delta_{1/2,-1}(B) - i\Gamma/2} \right|^2 \quad (3.52a)$$

$$\gamma_{1/2 \rightarrow -1/2} = \frac{\Omega^2 \Gamma}{4} \left| \frac{c_{0,1/2} c_{0,-1/2}}{\Delta_{-1/2,0}(B) - i\Gamma/2} + \frac{c_{-1,1/2} c_{1,-1/2}}{\Delta_{-1/2,1}(B) - i\Gamma/2} \right|^2. \quad (3.52b)$$

where $\Delta_{m_i, m_j}(B) = \Delta - g_I \mu_N m_i B - E_{m_j, m_i}(B)$, is an abbreviation for the detuning from the respective line, where $E_{m_j, m_i}(B)$ is the relevant solution from the modified Breit-Rabi formula (3.39), while $g_I \mu_N m_i B$ gives the Zeeman shift in the ground state.

To avoid causing decoherence in the scattering process, the elastic scattering rate for $m_i = 1/2$ has to equal the elastic scattering rate for $m_i = -1/2$, otherwise each scattering process constitutes a weak measurement of the state and causes decoherence. For sufficiently large magnetic fields $B \gtrsim 50\text{mT}$, the states asymptoting to $|m_j = 0\rangle \otimes |m_i\rangle$ are separated by less than the linewidth of the excited state. When the laser is then tuned in the middle between them, an equal superposition of those two states will be excited, while excitation to other states is negligible. Decay from this equal superposition will preserve coherences of the nuclear spin, and the elastic scattering rates for the two processes will be identical. The scattering rates for spin preserving and spin flip transitions as functions of detuning for different magnetic fields, at the saturation intensity at which $\Omega = \Gamma/\sqrt{2}$, are shown in Fig. 3.6. The ratio between the nuclear-spin-preserving scattering rate and the nuclear-spin-flipping scattering rate is several orders of magnitude, allowing for many scattering

processes before a spin flip occurs. This scattering process can therefore be used for readout via fluorescence or for the quenching process in resolved sideband cooling as discussed above.

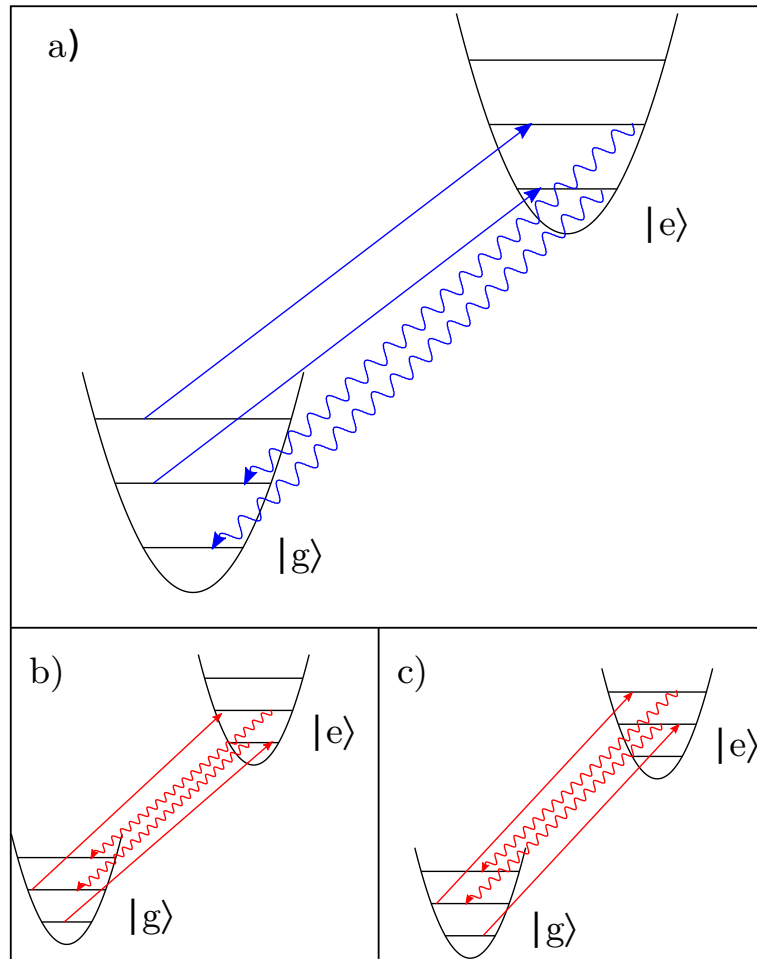


Figure 3.1: Schematics of resolved sideband cooling a) shows the cooling process, while b) shows heating via excitation on the carrier, followed by decay on the blue sideband. c) shows heating by excitation on the blue sideband followed by decay on the carrier.

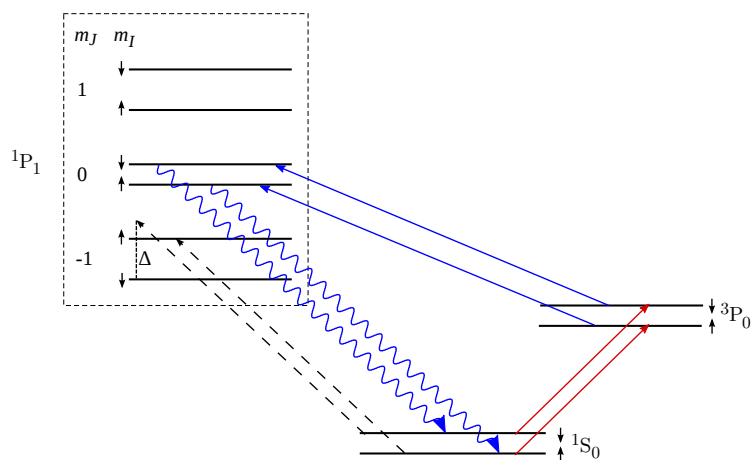


Figure 3.2: Schematic cooling and readout level-diagram for ^{171}Yb (analogous for ^{87}Sr). Sideband cooling in a trap occurs via excitation on the $^1S_0 \rightarrow ^3P_0$ clock transition (vibrational levels not shown), quenched by coupling to the 1P_1 state. An external magnetic field splits the 1S_0 and 3P_0 nuclear sublevels (spin-up and spin-down shown) and ensures preservation of the nuclear spin during resonant excitation and repumping. The dashed arrows demonstrate a possible readout scheme by resonance fluorescence.

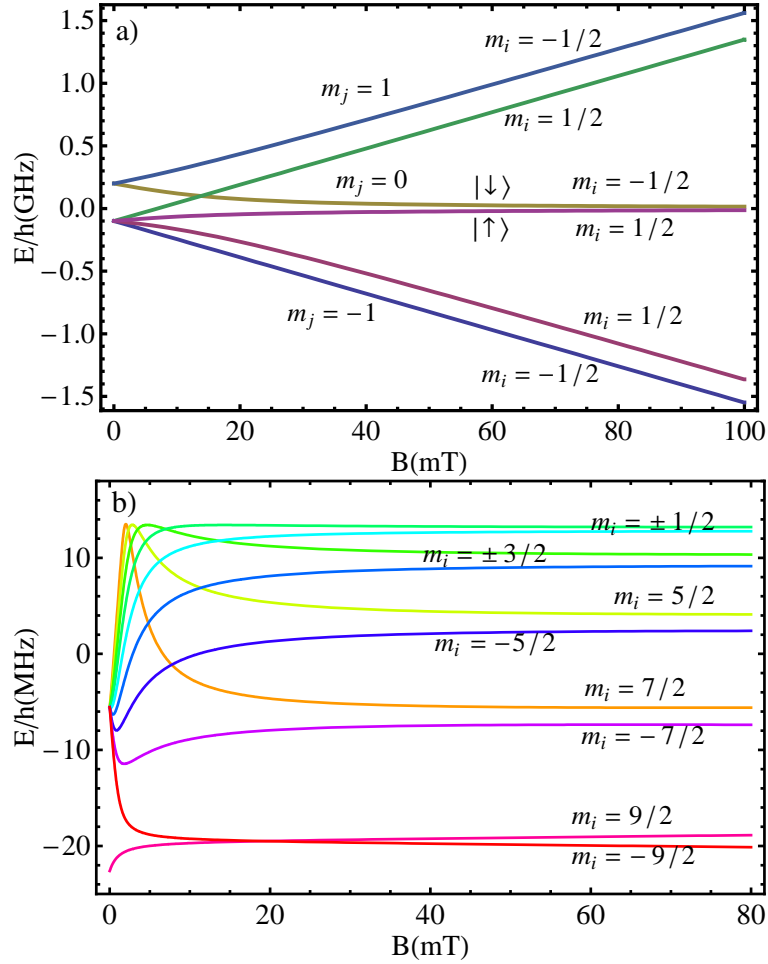


Figure 3.3: Zeeman diagram of the 1P_1 manifold. (a) In ^{171}Yb a slightly modified version of the Breit-Rabi formula applies. The hyperfine sublevels decouple to product states of electron and nuclear spin (Paschen-Bach) with modified linear Zeeman shift. The qubit is encoded in the states $|\uparrow\rangle$ and $|\downarrow\rangle$ in the $m_j = 0$, subspace. (b) ^{87}Sr Zeeman diagram for the $2i + 1 = 10$ sublevels that asymptote to the $m_j = 0$ subspace in the Paschen-Bach regime (other subspaces not shown). Because of the large quadrupole effect, pairs with $\pm m_i$ are closely spaced for magnetic fields between 50 and 120 mT. Qubits can be encoded in these pairs without losing coherence in spontaneous emission.

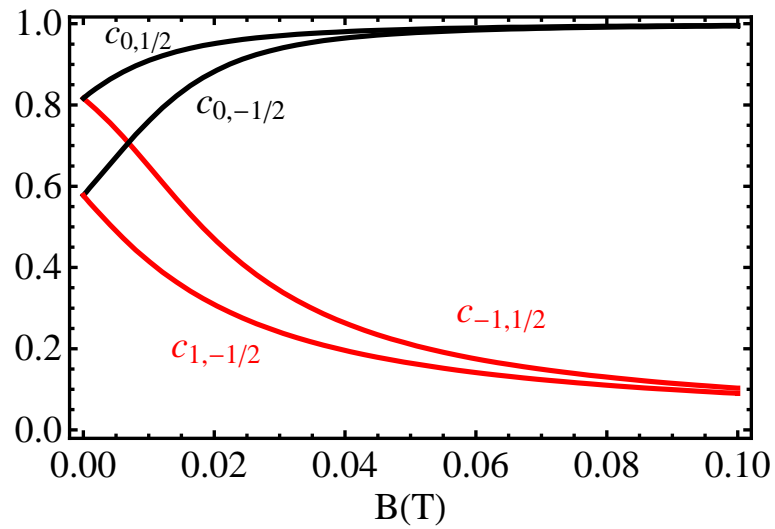


Figure 3.4: Field dependent expansion coefficients c_q for the m_f state of ^{171}Yb . For zero magnetic fields, these are the well known Clebsch-Gordan coefficients, however, for high magnetic fields, the coefficients $c_{0,\pm 1/2}$ go to one, while the coefficients $c_{1,\pm 1/2}$ go to zero. In the limit of infinite magnetic fields, both the spin-flip probability $c_{1,\pm 1/2}^2$ and the differential g-factor δg go to zero.

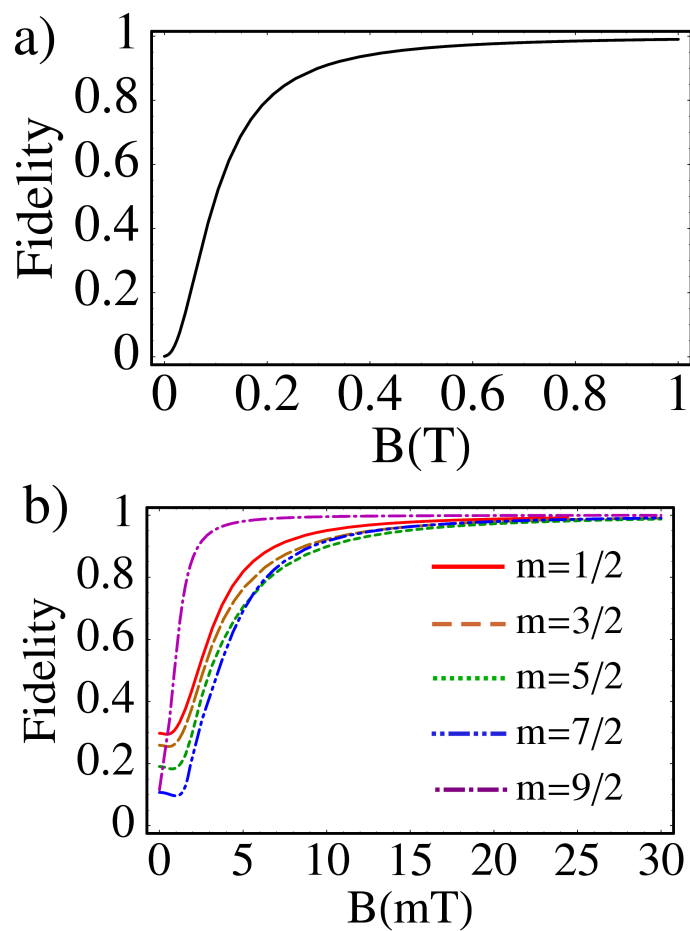


Figure 3.5: Fidelity for transfer of coherence, $\mathcal{F} = \Gamma'^2/(\Gamma^2 + \delta^2)$ (see text), as a function of magnetic field. (a) The spin-1/2 qubit of ^{171}Yb . (b) Different choices of qubit encoding as $\pm m_i$ in ^{87}Sr .

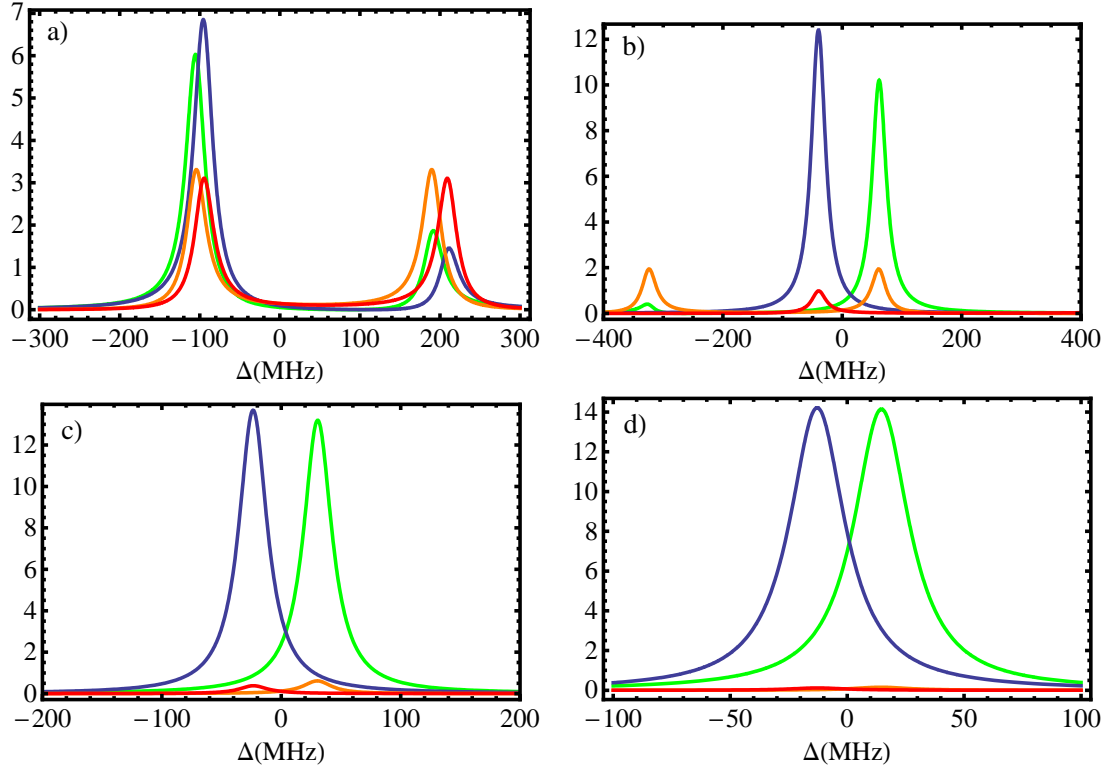


Figure 3.6: Scattering rates (arbitrary units) for the cooling scheme utilizing intermediate magnetic fields and large detuning to achieve decoupling of the nuclear spin from the electronic degrees of freedom. Shown are the scattering rate $\gamma_{1/2 \rightarrow -1/2}$ (blue), $\gamma_{-1/2 \rightarrow -1/2}$ (green), $\gamma_{1/2 \rightarrow 1/2}$ (red) and $\gamma_{-1/2 \rightarrow 1/2}$ (orange), as a function of the detuning relative to the middle between the two states asymptoting to $|m_j = 0\rangle \otimes |m_i\rangle$. The different panels are for different magnetic fields, a) is for a magnetic field of 1 mT, b) for 25 mT, c) for 50 mT and d) for 100 mT. For the higher magnetic fields the ratio between the spin-conserving scattering rates to the spin-changing scattering rates is large.

Chapter 4

Optical Feshbach Resonances for ^{171}Yb

4.1 Background

Feshbach resonances, which were first described by Feshbach [67] and Fano [68], are a very important tool for the manipulation of the scattering properties of two interacting atoms [35]. They occur when a bound state of one molecular potential, a closed channel, is energetically close to the threshold of another molecular potential, an open channel, of the same system (see Fig. 4.1). Under these circumstances, a scattering state of the second potential can easily be coupled to the molecular bound state, thus changing its scattering properties and causing the scattering length of the open channel to go through a pole. Here, the scattering length reaches the unitary limit, $a \rightarrow \infty$. (See also section 2.1.) Off-resonantly, there is still some admixture of the closed-channel wave function to the open-channel wave function, which is sufficient to change the scattering length.

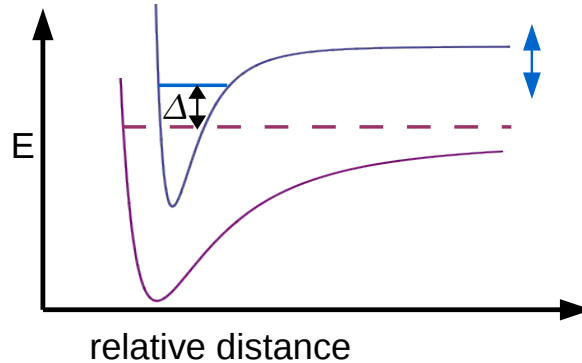


Figure 4.1: Schematics of a Feshbach resonance. There are two potentials, one of which has a bound state energetically close to the threshold of the other one. It is possible to change the relative energy of the two potentials and thus changing the detuning Δ between the scattering state and the bound state. For $\Delta = 0$, the open channel is resonant with the closed channel and the scattering length diverges.

4.1.1 Feshbach resonances in controlling atom-atom interactions

There is a multitude of applications which are only feasible due to the presence of Feshbach resonances and the resulting tunability of the scattering interaction between two atoms. One example is the production of cold molecules via Feshbach resonances [69], which has been successfully applied for several different species of alkalis [35]. To this end, the atoms are brought together and then the parameters of the experiment are slowly changed, such that the atoms are adiabatically swept through the Feshbach resonance. The resulting molecules are only weakly bound, however, they can then be optically transferred to more deeply bound ultracold molecular states. This is particularly interesting, since it is not possible to laser-cool molecules, due to the absence of cycling transitions. Additionally, it allows for the creation of cold polar molecules, whose strong isotropic interaction might

allow for novel quantum effects [70]. Furthermore, there have been proposals to use Feshbach resonances in the implementation of quantum information processing in optical lattices, either by using them to facilitate the interaction between marker atoms in a superlattice and the memory atoms stored in another lattice [12] or to create a polar molecule on each lattice site and use these for QIP [71].

Since two-body interactions are the basis of all many-body phenomena, it is not surprising that Feshbach resonances have also been used to investigate a broad range of more complex effects, such as the BEC-BCS crossover, where fermionic atoms form a BCS state on one side of the Feshbach resonance and bosonic molecules form a BEC on the other [72]. Additionally, Feshbach resonances are useful in controlling the superfluid-Mott-insulator transition, and they also allow one to change dilute ultracold gases from being repulsive to being attractive, thus allowing to investigate the resulting changes of the many-body states of such systems in real time [15, 73].

4.1.2 Magnetic vs. Optical Feshbach resonances

To date, most applied Feshbach resonances were induced through the application of an external magnetic field. Here the two different channels are different hyperfine levels in the ground state of alkali atoms, which have different magnetic moments. Changing the magnetic field therefore changes the position of the bound state relative to the scattering state, and the resulting scattering length a can be parameterized as [35]

$$a = a_{bg} \left(1 - \frac{\Delta_B}{B - B_0} \right), \quad (4.1)$$

where Δ_B is the width of the Feshbach resonance, while B_0 is its position and a_{bg} is the background scattering length in the absence of a magnetic field.

However, it is also possible to realize *optical* Feshbach resonances, by using a laser to couple a scattering ground state to an excited molecular bound state [74, 75].

This is particularly relevant for alkaline-earths, which do not have different hyperfine states in their 1S_0 ground state and thus do not have magnetic Feshbach resonances. Furthermore, lasers can be controlled much more easily and faster than magnetic fields, allowing for unprecedented control over the two-body interactions, including spatially and temporally varying scattering lengths. On the other hand, big admixtures and therefore large changes of the scattering length require a large Condon factor, that is, good overlap between the bound molecular wave function and the ground state scattering wave function. To accomplish this, it is necessary to couple the ground state wave function to long-range states which are very close to dissociation, where the density of states is high. However, to now control the scattering length without causing large losses due to photoassociation and spontaneous emission, the detuning has to be big relative to the linewidth of the state. For alkalis, due to their relatively broad optical transitions, it is not possible to fulfill all these conditions at once, leading to substantial losses due to rapid spontaneous emission [76, 77, 78]. Fortunately, the very narrow intercombination transition of alkaline-earths allows for their simultaneous fulfillment [79, 80].

In this chapter, I study optical Feshbach resonances for the $^1S_0 \rightarrow ^3P_1$ transition of ^{171}Yb . The underlying models are generally applicable to other alkaline-earths, however, ^{171}Yb was chosen since its nuclear spin $i = 1/2$ forms a natural qubit for quantum information processing. Optical effects in collisions of alkaline-earth-like atoms have been demonstrated in recent experiments, including photoassociation spectroscopy in ^{171}Yb [81] and ^{88}Sr [82] and optical Feshbach resonances of the bosonic isotopes with zero nuclear spin, including ^{172}Yb , ^{176}Yb [80] and ^{88}Sr [83]. I describe here the first multichannel calculation of Feshbach resonances in fermionic alkaline-earth-like atoms, including excited-state hyperfine structure, and the resulting modification to nuclear-exchange processes that can be controlled through off-resonant laser excitation.

4.1.3 Theory of optical Feshbach resonances

Consider a pair of colliding atoms, just above threshold in their ground state interaction potential V_S . These atoms are illuminated by a laser with energy $\hbar\omega_L$ which is slightly detuned from an excited bound state E_b in an excited bound state potential V_B , such that the detuning $\Delta = E_b/\hbar - \omega_L$, causing coupling between the two potentials V_B and V_S with the optical coupling potential

$$V_{opt}(I_L) = d_A E = \hbar\Gamma_A \sqrt{\frac{I_L}{2I_{sat}}}, \quad (4.2)$$

where d_A is the atomic dipole moment, while $E = \sqrt{2I_L/(c\epsilon_0)}$ is the electric field of the laser with the permittivity of vacuum ϵ_0 , the intensity of the laser I_L and the speed of light c . Furthermore, $I_{sat} = (2\pi^2\hbar\Gamma_A c)/(3\lambda^3)$ is the atomic saturation intensity, which is 0.13 mW/cm^2 for the intercombination transition in ^{171}Yb , and Γ_A and λ are the linewidth and wavelength of the atomic transition, respectively [84, 79].

Bohn and Julienne [84] started with this coupling to derive a semianalytic formula for the scattering length for optical Feshbach resonances. The scattering matrix resulting from this ansatz is given by

$$S = e^{2i\delta_{bg}} \frac{\Delta - i(\Gamma_{stim} - \Gamma_M)/2}{\Delta + i(\Gamma_{stim} + \Gamma_M)/2}, \quad (4.3)$$

with the background phase shift δ_{bg} in the absence of laser light. Here Γ_M is the natural molecular linewidth and Γ_{stim} is the linewidth at a finite collision energy, broadened by stimulated emission to be

$$\Gamma_{stim}(I) = \frac{\pi}{2\hbar} |\langle b|\mathbf{d} \cdot \mathbf{E}|E\rangle|^2 = \pi V_{opt}^2 |\langle b|E\rangle|^2 = \frac{\pi}{2} \left(\frac{I}{I_{sat}} \right) \hbar\Gamma_A^2 f_{FC}. \quad (4.4)$$

where f_{FC} is the Franck-Condon factor that measures the overlap between the spatial wave function of the scattering electronic ground state $|E\rangle$ at energy E and the bound excited state $|b\rangle$, see Eq. (4.36). Note that this definition of the Franck-Condon factor includes the spin parts of the wave functions, thus it equals $f_{FC}f_{rot}$ from [79].

From Eq. (4.3), I want to obtain the optical scattering length, which is generally of the form

$$a(\Delta, I) = a_{bg} + a_{opt}(\Delta, I) - ib_{opt}(\Delta, I), \quad (4.5)$$

where a_{bg} is the background scattering length in the absence of the radiation, and both the real part of the optically induced scattering length, $a_{opt}(\Delta, I)$ and the imaginary part $b_{opt}(\Delta, I)$ are functions of the intensity of the radiation I and the detuning Δ . Inserting Eq. (4.3) into (2.17) with $\delta \rightarrow \delta - \delta_{bg}$, where δ_{bg} is the background scattering phase shift, which is small for ^{171}Yb , the optically induced parts of the scattering length are given by

$$a_{opt}(I, \Delta) = l_{opt}(I) \left(\frac{\Delta \Gamma_M}{\Delta^2 + (\Gamma_M + \Gamma_{stim}(I))^2/4} \right) \approx l_{opt}(I) \frac{\Gamma_M}{\Delta} \quad (4.6)$$

and

$$b_{opt}(I, \Delta) = \frac{l_{opt}(I)}{2} \left(\frac{\Gamma_M^2}{\Delta^2 + (\Gamma_M + \Gamma_{stim}(I))^2/4} \right) \approx \frac{1}{2} l_{opt}(I) \left(\frac{\Gamma_M}{\Delta} \right)^2. \quad (4.7)$$

The latter form of the equations is only valid in a regime in which $\Delta \gg \Gamma_M$ and $\Delta \gg \Gamma_{stim}$, where Γ_M is the molecular spontaneous decay rate calculated from the multichannel wave function. The optical length $l_{opt}(I)$, which is a key parameter determining the strength of the influence of the laser is given by [85]

$$l_{opt}(I) = \Gamma_{stim}(I)/(2k_r \Gamma_M), \quad (4.8)$$

where k_r is the relative coordinate wave number for the reduced mass μ .

As Eqs. (4.6) and (4.7) show, the scattering length can only be changed without the introduction of large losses if $\Delta \ll \Gamma_M$, which, as mentioned before, is the reason for the inherent advantage of alkaline-earths over alkalis for the implementation of optical Feshbach resonances.

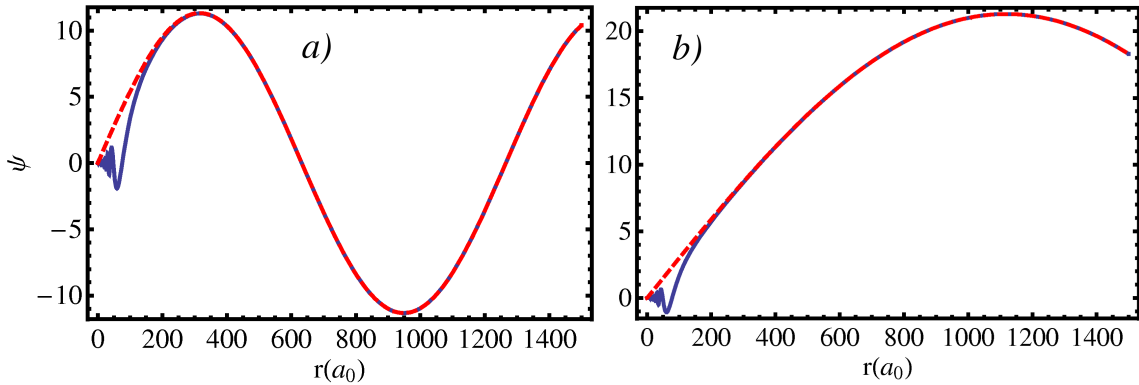


Figure 4.2: S-wave ground state wave functions calculated with the formula by Bo Gao [86], for a temperature of a) $25\mu\text{K}$ and b) $2\mu\text{K}$. The dashed red line is a sine function, shifted by the known scattering length of $-2.83 a_0$. It can be seen that the agreement is excellent.

4.2 Calculation

The prediction of the optical Feshbach scattering length as a function of the laser intensity and detuning requires a good understanding of both the ground state scattering wave functions and the excited molecular wave functions. This in turn requires a good understanding of the molecular potentials, including the nuclear spin and the hyperfine interaction, as well as magnetic fields and rotation.

4.2.1 Ground States

For alkaline-earths, the $^1S_0 + ^1S_0$ ground state is comparatively simple, in the absence of nuclear spin there is only one single potential. For isotopes with finite nuclear spin, these potentials have a multiplicity, however, owing to the lack of hyperfine interaction they are not coupled to each other and can therefore be treated as single channels. For alkaline-earth-like atoms in the ground state, the only nonzero quantum number are the nuclear spin \mathbf{i} and the orbital angular momentum of the

two nuclei, \mathbf{R} that defines the partial wave of the states. ^{171}Yb , with its nuclear spin of $1/2$ is a fermion, thus the total wave function has to be antisymmetric. Since the parity of the spatial wave function is given by $p = (-1)^R$, it follows that the only allowed spin state for even partial waves is given by the antisymmetric singlet state χ_S .

$$\frac{1}{\sqrt{2}} (|\downarrow\rangle_A |\uparrow\rangle_B - |\uparrow\rangle_A |\downarrow\rangle_B) \otimes |R, m_R\rangle = \chi_S \otimes |R, m_R\rangle, \quad (4.9)$$

where $|\uparrow\rangle = |i = 1/2, m_i = 1/2\rangle$ and $|\downarrow\rangle = |i = 1/2, m_i = -1/2\rangle$, while A and B label the two different nuclei. For odd partial waves, on the other hand, the spin state is in one of the triplet states, that is

$$\begin{aligned} \frac{1}{\sqrt{2}} (|\downarrow\rangle_A |\uparrow\rangle_B - |\uparrow\rangle_A |\downarrow\rangle_B) \otimes |R, m_R\rangle &= \chi_T \otimes |R, m_R\rangle \\ |\downarrow\rangle |\downarrow\rangle |R, m_R\rangle & \\ |\uparrow\rangle |\uparrow\rangle |R, m_R\rangle &. \end{aligned} \quad (4.10)$$

where the magnitude of $\mathbf{I} = \mathbf{i}_1 + \mathbf{i}_2$, $I = 1$, $p = -1$ and the magnitude of the total angular momentum in the ground state $\mathbf{T} = \mathbf{R} + \mathbf{I}$. For p-waves, where $R = 1$, $T = 0, 1$ or 2 .

Because the bulk of the probability amplitude of these wave functions lies away from the chemical binding region, only the long-range part of the potential, which can be modeled with a van der Waals C_6/r^6 potential, influences the shape of the ground state wave functions. Therefore, we can use the semi-analytic solutions to such a C_6/r^6 potential found by Gao [86] to determine these functions. This yields two linearly independent solutions, $g(r)$ and $f(r)$. The energy-normalized ground state wave function is then given by

$$\Psi_{gao}(r) = \sqrt{\frac{2\mu}{\pi\hbar^2k}} (f(r) - K_0g(r)). \quad (4.11)$$

Here K_0 is calculated from the scattering length of the ground state potential of ^{171}Yb , via

$$-ka = \frac{K_0 Z_{gg} - Z_{fg}}{Z_{ff} - K_0 Z_{gf}}, \quad (4.12)$$

where Z_{gg} , Z_{fg} , Z_{ff} and Z_{gf} are parameters determined by the energy and the C_6 coefficient, as described in detail in [86]. The s-wave scattering length for the ground state of ^{171}Yb was determined by Kitagawa *et al.* [87] to be $a = -0.15 \text{ nm} = -2.83 a_0$, where a_0 is the Bohr radius. In the same paper, the C_6 coefficient was found to be $C_6 = 1932(30) \text{ au}$.

For large r , outside of the range of the van der Waals potential, the wave function becomes a phase-shifted free scattering state,

$$\Psi_{gao}(r) \xrightarrow{r \rightarrow \infty} \sqrt{\frac{2\mu}{\pi \hbar^2 k}} (\sin(kr) - ka \cos(kr)) \quad (4.13)$$

Plots of the resulting s-wave ground state wave functions for $2\mu\text{K}$ and $25\mu\text{K}$ can be seen in Fig. 4.2, together with the long-range wave functions calculated from the scattering length for the ground state potential. For sufficiently large internuclear distance r , the agreement is excellent. For p-waves, the scattering length was determined from a fit to a numerical calculation with the Numerov method to be $a_{bg}^p = (\tan[\delta_{bg}^p]/k^3)^{1/3} = -116a_0$.

4.2.2 Excited States

The excited $^1S_0 + ^3P_1$ molecular states are much more complicated, giving rise to a multitude of different coupled potentials, and thus requiring a full multichannel calculation. That is, the different scattering channels are coupled to each other, and diagonalizing the potential part of the Hamiltonian at each internuclear distance r will not capture all the interactions. Physically, the scattering interaction can be seen as a beamsplitter, where the incoming scattering state is split into the different channels, interacts there with different interaction amplitudes and the different channels interfere [39]. Thus, the resulting wave functions will have components of more than one channel and is discussed in more depth in Section 4.3.4. Fully accounting for this requires diagonalizing the Hamiltonian for all the channels and internuclear distances at the same time, and is done with a DVR method, as described later.

We find the overall Hamiltonian by starting with the Born-Oppenheimer potentials, that is, the potentials formed by electrostatic interaction and relativistic spin-orbit interactions. Since we are interested in the hyperfine structure, including rotation and magnetic fields, the relevant Hamiltonians are added to the Hund's case c) Hamiltonian, such that

$$H = H_c + H_{HF} + H_{rot} + H_{mag}. \quad (4.14)$$

The first term represents the radial kinetic energy of the nuclei $p_r^2/2\mu$ plus the electronic Born-Oppenheimer potentials that asymptote to the $^1S_0 + ^3P_1$ scattering channel and define potential curves $V_{\Omega\sigma}(r)$, where $\sigma = p(-1)^l$. These potentials are modeled through a Lennard-Jones plus dipole-dipole potential,

$$V_{\Omega\sigma}(r) = \frac{C_{12}}{r^{12}} - \frac{C_6}{r^6} - \sigma \frac{C_3^\Omega}{r^3}, \quad (4.15)$$

where the parameters are known reasonably well from fits to experimental data as $C_6 = 2810$ au, $C_{12} = 1.862 \times 10^8$ au and $C_3^1 = -C_3^0/2 = 0.09695$ au [40]. The hyperfine interaction between the electron and nuclear spin is described by

$$H_{HF} = A(\mathbf{i}_1 \cdot \mathbf{j}_1 + \mathbf{i}_2 \cdot \mathbf{j}_2) \quad (4.16)$$

with the hyperfine constant A , using the fact that $j_1 = 1, i_1 = 1/2$ and $j_2 = 0$. The nuclear mechanical rotational part of the Hamiltonian is given by $H_{rot} = \frac{\hbar^2}{2\mu r^2} R(R+1)$, with the reduced mass μ , radius r and rotational angular momentum quantum number R . Finally, in the limit of small magnetic fields, ($|\mu_B g_f \mathbf{B}| \ll A\hbar$) such that we are in the Zeeman regime where the projections of \mathbf{f}_1 and \mathbf{f}_2 are good quantum numbers, the magnetic field part of the Hamiltonian is given by $H_{mag} = \mu_B g_f \hat{\mathbf{f}}_1 \cdot \mathbf{B} + \mu_B g_f \hat{\mathbf{f}}_2 \cdot \mathbf{B}$ where B is the strength of the magnetic field, g_f is the Landé g-factor and μ_B is the Bohr magneton. Due to the large hyperfine constant of 3.958 GHz of the 3P_1 state of ^{171}Yb , the above condition is fulfilled to a good approximation for magnetic fields up to several tesla. We neglect the small magnetic dipole-dipole interactions between nuclei.

For the given Hamiltonian, the good quantum numbers are the total angular momentum quantum number T , its projection on the space-fixed quantization axis M_T , and parity due to inversion of all particles p . Here $\mathbf{T} = \mathbf{F} + \mathbf{R}$, with $\mathbf{F} = \mathbf{J} + \mathbf{I}$, where \mathbf{J} is the electronic angular momentum (spin and orbital, $\mathbf{J} = \mathbf{L} + \mathbf{S}$), \mathbf{R} is the nuclear orbital angular momentum describing mechanical rotation of the dimer, and \mathbf{I} is the nuclear spin angular momentum. In addition, by Fermi statistics, the total wave function must be antisymmetric under exchange of the nuclei, and by exchange of all particles. In the absence of a magnetic field, F is also a good quantum number. Other quantum numbers are approximate, depending on the dominant forces. Any basis of states that is specified by these eigenvalues is constrained by the overall symmetries. For example, for a separable basis of electron and nuclear orbitals, $(-1)^{l_1+l_2+R} = p$, where $l_1 = 0, l_2 = 1$ are the individual atomic electron angular momenta for the S+P collision.

4.2.3 Channel Bases

As discussed in Sec. 2.3, the overall Hamiltonian matrix can be calculated by defining several bases, defined by different couplings of the angular momenta of the atoms, in which the different parts of the Hamiltonian are diagonal. Finding the overall Hamiltonian matrix then reduces to the application of basis transformations. The uncoupled atoms have $|nl_s j m_j i m_i\rangle$ as good quantum numbers, where $j = 0$ for the 1S_0 ground state. In the excited 3P_1 state, \mathbf{j} and \mathbf{i} are coupled to give \mathbf{f} , the total angular momentum of the atom. While there are many different ways in which these angular momenta can be coupled to each other and to the rotation \mathbf{R} of the two nuclei, only the following three bases are relevant here. Most of the calculation is done in the $|\epsilon\rangle$ basis, which is a Hund's case e) basis, extended to include the nuclear spin

$$|\epsilon\rangle = |((f_1 f_2)FR)TM_T p\rangle. \quad (4.17)$$

For the excited $^1S_0 + ^3P_1$ state, we chose the atom with label 2 to be in the ground state, such that $\mathbf{j}_2 = 0$, $\mathbf{f}_2 = \mathbf{i}_2$, for alkaline-earths. $\mathbf{F} = \mathbf{f}_1 + \mathbf{f}_2$ is the total angular momentum of the coupled atoms, with magnitude $f_1 = 1/2, 3/2$ and $f_2 = 1/2$ for the possible individual atomic angular momenta. This basis is used for the calculation of the hyperfine part of the Hamiltonian, which is diagonal in this basis and can be expressed as

$$\begin{aligned} H_{HF} &= A(\mathbf{i}_1 \cdot \mathbf{j}_1 + \mathbf{i}_2 \cdot \mathbf{j}_2) = A/2 [f_1(f_1 + 1) - i_1(i_1 + 1) - j_1(j_1 + 1)] \\ &= A/2 [f_1(f_1 + 1) - 11/4], \end{aligned} \quad (4.18)$$

where in the last step the fact that $i_1 = 1/2$, $j_1 = 1$ and $j_2 = 0$ was used. Additionally, the magnetic field Hamiltonian, H_B is also diagonal in this basis and becomes $H_B = g_f m_{f_1} \mu_B$, for a magnetic field along the z-axis of the space fixed coordinate system.

Another important basis is the uncoupled $|\pi\rangle = |f_1 m_{f_1}, i_2 m_{i_2}, R m_R, p\rangle$ basis, which is valid for very far separated atoms, such that their electron spin, electronic orbital angular momentum and nuclear spins are coupled together to give a total atomic spin $\mathbf{f}_k = \mathbf{j}_k + \mathbf{i}_k$ for each atom k . Additionally, the projection of f_k on the space-fixed axis, m_{f_k} is also a good quantum number, as are the rotational quantum number of the two atoms R and its projection on the space-fixed axis m_R . Denoting $|\beta_k\rangle = |\gamma_k f_k m_{f_k}\rangle = |n_k((s_k l_k) j_k i_k) f_k m_{f_k}\rangle$ (for the atom in the ground state, $\mathbf{f} = \mathbf{i}$, since $\mathbf{j} = 0$) and symmetrizing yields

$$\begin{aligned} |\pi\rangle &= |(\beta_1 \beta_2)^\rho R m_R\rangle = \\ &= \begin{cases} \frac{1}{\sqrt{2}} [|\beta_1\rangle_A |\beta_2\rangle_B + \rho (-1)^R |\beta_2\rangle_A |\beta_1\rangle_B] \otimes |R, m_R\rangle \\ |\beta_1\rangle_A |\beta_2\rangle_B \otimes |R, m_R\rangle \end{cases} \end{aligned} \quad (4.19)$$

Here $\rho = -1$ for fermions and the labels A and B denote the different nuclei. As required, these states are antisymmetric under exchange of atoms A and B . The parity is given by $p = p_1 p_2 (-1)^R$, where p_k is the parity of the electron state k , which is -1 for the 3P_1 state and 1 for the 1S_0 state. This basis is used to calculate the matrix elements of the dipole operator between the ground and multichannel

excited states. These are essential for determining the molecular natural linewidth as detailed in [85], where the transformation $\langle\pi|\epsilon\rangle$ is also given to be

$$\langle\epsilon|\pi\rangle = \delta_{\gamma'_1, \gamma_1} \delta_{\gamma'_2, \gamma_2} \delta_{f'_1, f_1} \delta_{f'_2, f_2} \delta_{R'_1 R_2} \langle f_1 f_2 m_{f_1} m_{f_2} | F m_F \rangle \langle F' m_F R m_R | T, M_T \rangle \Xi_{\epsilon, \pi'}, \quad (4.20)$$

where $\Xi_{\epsilon\pi'} = \sqrt{2}$ for $\gamma_1 f_1 = \gamma_2 f_2$ but $m_{f_1} \neq m_{f_2}$ and 1 otherwise. In the excited molecular states, one atom is in the $(6s^2)^1S_0$ state and the other one in the $(6s6p)^3P_0$ state, therefore, $\Xi_{\epsilon, \pi'}$ is always one.

H_{mag} , which is diagonal in the $|\pi\rangle$ basis, but not in the $|\epsilon\rangle$ basis, is then calculated via

$$\langle\epsilon|H_{mag}|\epsilon\rangle = \sum_{\pi, \pi'} \langle\epsilon|\pi\rangle \langle\pi|H_{mag}|\pi'\rangle \langle\pi'|\epsilon\rangle. \quad (4.21)$$

Additionally, the molecular dipole matrix element in the $|\epsilon\rangle$ can be calculated with the $|\pi\rangle$ basis

$$\langle\epsilon|(d_{mol})_q|\epsilon_g\rangle = \sum_{\pi\pi_g} \langle\epsilon|\pi\rangle \langle\pi|(d_{mol})_{q'}|\pi_g\rangle \langle\pi_g|\epsilon_g\rangle, \quad (4.22)$$

in which it can be reduced to sums of the atomic dipole moment d_q

$$\begin{aligned} \langle\pi|(d_{mol})_q|\pi_g\rangle &= \delta_{\rho_g \rho} \delta_{R_g R} \delta_{R_{M,g} R_M} \\ &\times \left[\langle\beta_1|d_q|\beta_{1,g}\rangle \delta_{\beta_2 \beta_{2,g}} + \rho(-1)^R \langle\beta_1|d_q|\beta_{2,g}\rangle \delta_{\beta_2 \beta_{1,g}} \right] \end{aligned} \quad (4.23)$$

for $\beta_1 < \beta_2$ and

$$\langle\pi|(d_{mol})_q|\pi_g\rangle = \delta_{\rho_g \rho} \delta_{R_g R} \delta_{R_{M,g} R_M} \sqrt{2} \langle\beta_1|d_q|\beta_{1,g}\rangle \quad (4.24)$$

for $\beta_1 = \beta_2$. The following notation is used here. The ground states are labeled with a subscript g , for the excited state, β_2 denotes the an atom in the 1S_0 ground state and β_1 is the atom in the 3P_1 excited state.

The third basis, denoted by $|\gamma\rangle$, is an extended Hund's case c) basis, as derived in section 2.3. The Born-Oppenheimer Hamiltonian, H_c is diagonal in this molecular

basis for which $\mathbf{s}_1 + \mathbf{s}_2 = \mathbf{S}$, $\mathbf{l}_1 + \mathbf{l}_2 = \mathbf{L}$, $\mathbf{L} + \mathbf{S} = \mathbf{J}$ and $\mathbf{i}_1 + \mathbf{i}_2 = \mathbf{I}$. Furthermore, $\mathbf{I} + \mathbf{J} = \mathbf{F}$ which is then coupled to rotation of the nuclei \mathbf{R} , to give again the total angular momentum \mathbf{T} , $\mathbf{F} + \mathbf{R} = \mathbf{T}$.

$$|\gamma\rangle = |J\Omega I\Phi, TM_T p\rangle = \sum_{(JI)F\Phi} \langle (JI)F\Phi | J\Omega I\iota \rangle | (JI)F\Phi \rangle \mathcal{D}_{\Phi, M_T}^{T*}. \quad (4.25)$$

Here $\Phi = \Omega + \iota$ where Φ , Ω and ι are the projection of \mathbf{F} , \mathbf{J} and \mathbf{I} on the internuclear axis and $\mathcal{D}_{\Phi, M_T}^{T*}$ is the wave function of a symmetric top. Thus, Φ is the projection of \mathbf{T} on the internuclear axis, while M_T is its projection on the space fixed axis. For a similar basis set for alkalis, compare to [85]. The basis transformation between $|\gamma\rangle$ and $|\epsilon\rangle$ is given by

$$\begin{aligned} \langle \gamma | \epsilon \rangle = & \langle F\Phi R0 | T\Phi \rangle \sqrt{\frac{2R+1}{2T+1}} \langle J\Omega, I\iota | F\Phi \rangle \\ & \times (-1)^{j_1+i_1+i_2+F} \sqrt{(2f_1+1)(2I+1)} \left\{ \begin{array}{ccc} j_1 & i_1 & f_1 \\ i_2 & F & I \end{array} \right\}, \end{aligned} \quad (4.26)$$

where $\{\dots\}$ denotes a Wigner 6J-symbol. The gerade/ungerade quantum number σ is determined by $p = \sigma(-1)^I$. For a derivation of this transformation see section 2.3.

4.3 Results

4.3.1 Selective Change of a for P-waves and S-waves

As discussed in section 4.2.1, the total nuclear spin for s-wave collisions $I=0$, as are all other angular momenta, including the total angular momentum T . The electronic ground states have a parity of $p = (-1)^R$, which is 1 for s-waves. Since the dipole operator is odd under parity and has a selection rule of $\Delta T = 0, 1$ with $T = 0 \rightarrow T = 0$ forbidden, the excited state has to have opposite parity $p = -1$, and a total angular momentum of $T = 1$. Therefore, the rotation R of the nuclei in the excited state has to be even. Given the fact that $\mathbf{T} = \mathbf{F} + \mathbf{R}$, with $F = 0, 1$ or 2 and

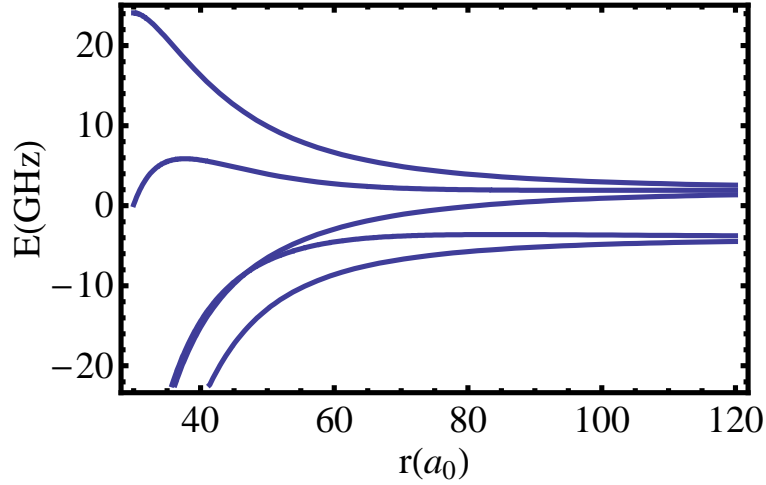


Figure 4.3: The excited adiabatic potentials, accessible via for s-wave collisions. These potentials are found by diagonalizing the potential part of the Hamiltonian as a function of the internuclear distance r . They have a total angular momentum of $T = 1$ and their parity $p = -1$. The shown potentials are for no magnetic field, thus they are degenerate in M_T .

because in the excited state we must have $(-1)^{l_1+l_2+R} = p = -1$, R can be either 0 or 2 in the excited state. Taking all this into account leads to 15 different basis states in the $|\epsilon\rangle$ basis, which are listed in table 4.1. However, the resulting Hamiltonian is blockdiagonal in M_T , thus there are three different blocks of 5 channels each. In the absence of a magnetic field, these three blocks are degenerate.

P-wave collisions are naturally more complex than s-wave collisions, given their higher rotation $R = 1$ and their triplet nuclear spin $I = 1$, which allow for $T = 0, 1$ or 2. Therefore, there are many more accessible excited states with $T = 0, 1, 2$ or 3, odd rotation $R = 1, 3, 5$ and even parity $p = 1$, leading to 89 different basis states in the $|\epsilon\rangle$ basis, as can be seen in table 4.2. The Hamiltonian is again block diagonal in M_T and T , giving rise to 16 different blocks ranging in size from 2×2 to 6×6 . In the absence of magnetic fields, this reduces to 19, $(2T+1)$ -fold degenerate channels. Due to the large mass of ^{171}Yb , the rotational energy is very small, causing several of the potentials with different R to be nearly degenerate. For better visualization, the adiabatic

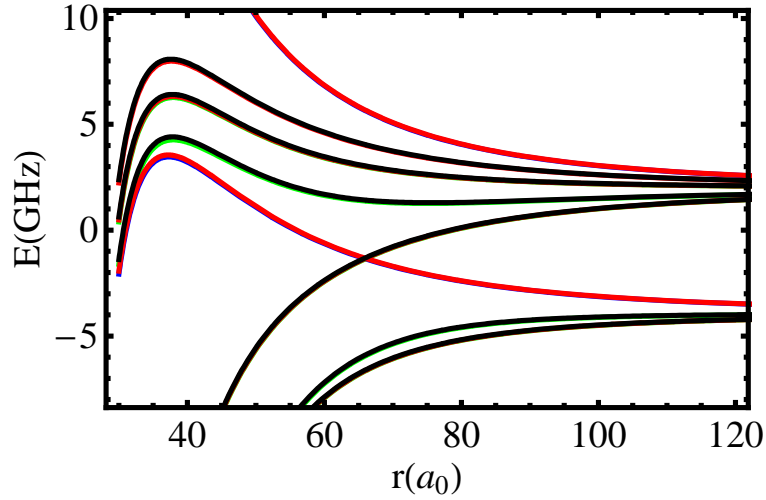


Figure 4.4: The excited adiabatic potentials for p-wave collisions, analogous to Fig. 4.3. Here the total quantum number $T = 0$ (blue), 1 (green), 2 (red) or 3 (black), causing different multiplicity for the different lines. Due to the small rotational energy, several of these lines can not be resolved on this scale, leaving only 8 distinct lines.

potentials are shown in Fig. (4.3) and Fig. (4.4). These potentials are obtained by diagonalizing the potential part of the Hamiltonian (4.14) for each value of r . While this gives a good visual understanding of the system, it can not exhibit the diabatic

T	f_1	F	R
1	1/2	1	0
1	1/2	1	2
1	3/2	1	0
1	3/2	1	2
1	3/2	2	2

Table 4.1: The different channels of the $|\epsilon\rangle$ basis used in the calculation for the s-wave states. f_2 is always 1/2 and is therefore suppressed. M_T , which is also not shown, can be -1, 0, or 1, for each of the states, leading to a total number of 15 different channels. In the absence of a magnetic field, each of these states is 3-fold degenerate, yielding 5 different degenerate potentials.

T	f_1	F	R
0	1/2	1	1
0	3/2	1	1
1	1/2	0	1
1	1/2	1	1
1	3/2	1	1
1	3/2	2	1
1	3/2	2	3
2	1/2	1	1
2	1/2	1	3
2	3/2	1	1
2	3/2	1	3
2	3/2	2	1
2	3/2	2	3
3	1/2	0	3
3	1/2	1	3
3	3/2	1	3
3	3/2	2	1
3	3/2	2	3
3	3/2	2	5

Table 4.2: The different channels of the $|\epsilon\rangle$ basis used in the calculation for the p-wave states. M_T is suppressed for clarity, however, each of the states has a multiplicity of $2T + 1$, yielding 89 different channels. In the absence of a magnetic field, each of these states is $2T + 1$ -fold degenerate, yielding 19 different degenerate potentials.

coupling between the different channels. Therefore, determining wavefunctions and eigenenergies from these potentials would be necessarily less accurate than the full multichannel calculation described earlier.

Note that the symmetry and selection rules cause the potentials to be split into two separate classes, one of which is accessible from s-wave collisions and the other that is accessible from p-wave collisions. This can be exploited for the independent manipulation of p-wave and s-wave scattering lengths, by choosing to use a bound state with parity $p = -1$, which is far from bound states with a parity of $p = 1$. Since this bound state is dark for p-waves, the s-wave scattering length is changed

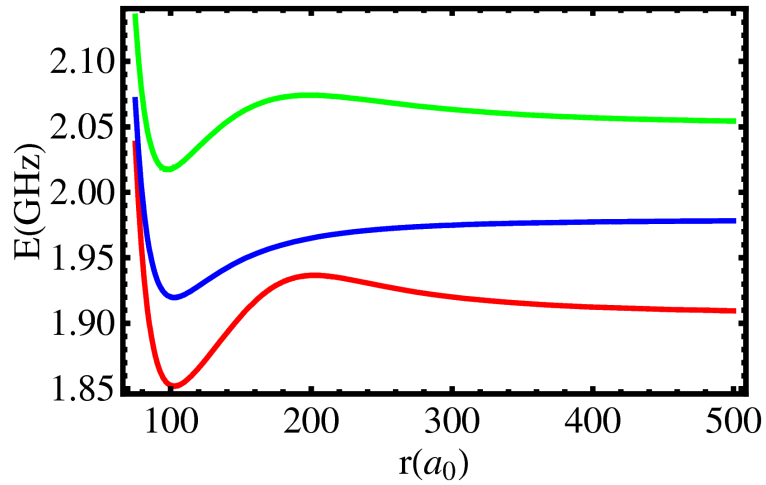


Figure 4.5: Adiabatic purely long-range potentials for s-waves, for a magnetic field of 1 kG. In the absence of a magnetic field all three potentials are degenerate with the line in the middle. It can be seen that the extremely shallow potentials get shifted and develop a barrier in the presence of a magnetic field.

more strongly than the p-wave scattering length that has a larger detuning. In the same manner it is possible to manipulate only p-waves or even to use two lasers simultaneously, one to change s-waves and the other one to change p-waves. By spatially and/or temporally changing the intensity of these two different Feshbach lasers, new and interesting avenues in the control of ultracold atoms are opened.

4.3.2 Purely Long-Range States

Of special interest are several purely long-range (plr) potentials. These are potentials which have both the outer and inner classical turning point at long internuclear distance. Typically, purely long-range potentials form in a transition regime between Hund's cases, where the strength of the spin-orbit coupling is about as large as the energy difference between the Born-Oppenheimer potentials. This can cause avoided crossings between the different Born-Oppenheimer potentials, such that the potential

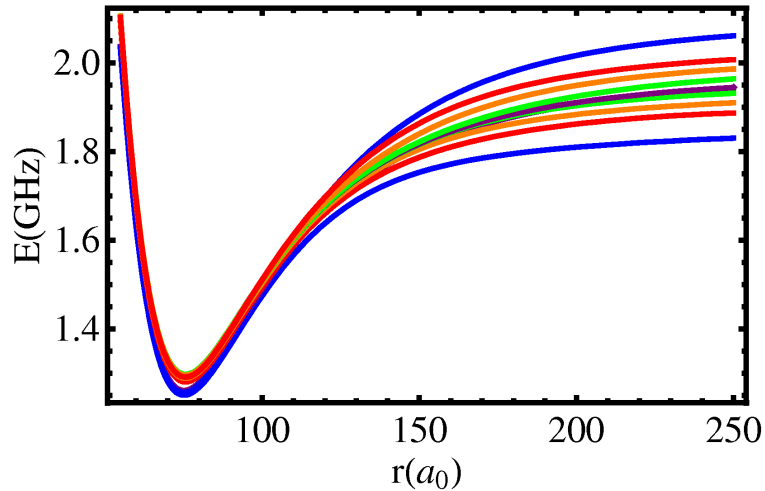


Figure 4.6: Adiabatic purely long-range potentials for p-waves, again for a magnetic field of 1 kG. While these potentials are also shifted in the presence of the magnetic field, they do not develop barriers. In the absence of a magnetic field, these potentials form two nearly degenerate potentials, due to their different rotational quantum number R .

surface acquires a minimum at large relative distance of the nuclei. Several bound states of these purely long-range potentials have been observed [39]. Additionally, at even larger r , it is also possible that the *hyperfine* interaction causes the same effect. Due to the smaller hyperfine constant compared to the fine-structure coupling constant, the resulting potential minimum is even shallower and at larger internuclear distance. Therefore, in alkalis, the hyperfine interaction is typically too small relative to the linewidth to observe such purely-long range states. In alkaline-earths, on the other hand, again due to the narrow intercombination line, and especially in ^{171}Yb with its large hyperfine constant, these states can be experimentally observed. The p-wave plr potential was experimentally observed by Enomoto *et al.* [81] and has a depth of only 717 MHz, while the s-wave plr potential is even more shallow, it has a depth of only 59.2 MHz and to date has not been experimentally observed. The adiabatic purely long-range potentials are shown in Fig. 4.5. The s-wave potential is triply degenerate in the absence of a magnetic field, with the quantum numbers

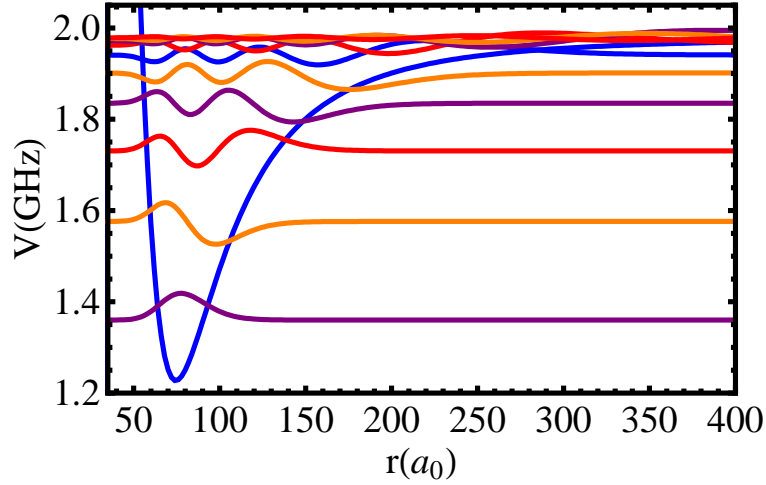


Figure 4.7: The eigenstates of an adiabatic purely long-range potential for p-waves in the absence of a magnetic field. All the amplitude of the states is at comparatively large r . For simplicity, the vibrational states shown are eigenfunctions of the adiabatic potential, similarly to the calculation in [81]. For full multichannel purely long-range states see Fig. 4.10.

$f_1 = 3/2, F = 1, R = 2, T = 1, M_T = 0, \pm 1$. In the presence of a magnetic field, however, the three degenerate potentials shift relative to each other and they also change their shape, developing a barrier and thus a possible shape resonance, as can be seen in Fig. 4.5. There are two nearly degenerate p-wave purely long-range potentials, one with the quantum numbers $f_1 = 3/2, F = 2, R = 1, T = 1, M_T$ in the ϵ basis and the other one with $f_1 = 3/2, F = 2, R = 1, T = 3, M_T$. In the absence of a magnetic field, the former is triply degenerate, while the latter is 7-fold degenerate. In the presence of a magnetic field, these potentials are also shifted relative to each other, lifting the degeneracies, as can be seen in Fig. 4.6, even though, in contrast to the s-wave purely long-range states, they do not acquire a shape resonance.

While all the states close to dissociation depend mainly on the very long-range part of the potentials, this effect is even more pronounced for purely long-range states, given that they are only sensitive to the hyperfine interaction and the long-range tail of the potential. This allows for very accurate determination of the C_n

coefficients if the molecular potentials are modeled with Lennard Jones potentials, including the determination of the C_3 coefficient in the excited states, which are closely related to the lifetime of the excited states. [39]. Furthermore, Enomoto *et al.* [81] used this to determine the C_6 coefficient for ^{171}Yb , by assuming a molecular potential which consists only of the C_6/r^6 part, the hyperfine Hamiltonian H_{HF} and the resonant dipole interaction resulting in a $1/r^3$ potential. Diagonalizing this and perturbatively adding the rotation yields adiabatic potentials, including the purely long-range states, allows one to solve for the only free parameter, C_6 . However, these solutions do not allow for a full multichannel calculation, given that the rotation is not fully included, nor are all the basis states.

Generally, given that all the amplitude of the purely-long range states is at large internuclear distance one would expect the purely long-range states to be especially suitable to the implementation of photoassociation and optical Feshbach resonances as compared to other states close to dissociation. However, other states at a similar energy actually have longer range than the purely long-range states, and therefore the Condon factor between the latter and the ground state is about an order of magnitude lower than for the former. Thus, the other states are better suited for these applications.

4.3.3 Excited-State Spectrum

Having obtained the multichannel Hamiltonian as a function of r in the $|\epsilon\rangle$ basis, a discrete variable representation (DVR) method [88, 89] is used to numerically find the eigenvalues and multichannel wavefunctions. As described by Colbert and Miller [89], this method is implemented by first choosing an evenly spaced grid $r_i = a + (b-a)i/N$ with $N - 1$ points, where i is an iterator going from 1 to $N - 1$ and a and b are the start and end point of the grid, respectively. The Fourier functions associated with

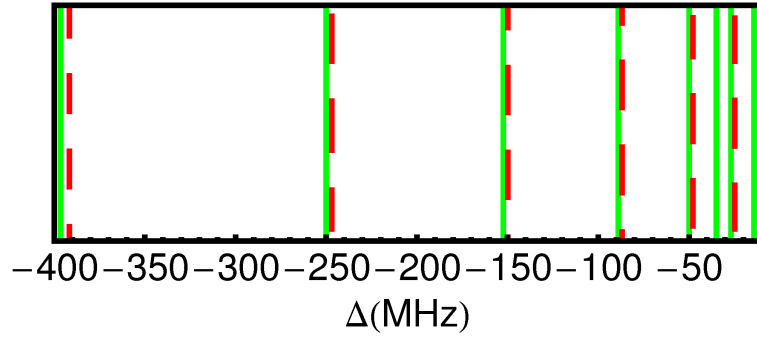


Figure 4.8: S-wave spectrum for the bound states of the excited states. The dashed (red) lines are the results experimental results from [81], while the green lines are from the full multichannel calculation. It can be seen that the agreement is good. There are some additional lines from the multichannel calculation, however, these have very weak Frank-Condon factors, such that they could not be seen experimentally. For the numerical values of the detuning, see also Table 4.3.

this grid are then

$$\phi_n(r) = \sqrt{\frac{2}{b-a}} \sin \left[\frac{n\pi(r-a)}{b-a} \right], \quad (4.27)$$

with the iterator $n = 1, \dots, N-1$. These functions are then used to expand the kinetic energy operator

$$T = -\frac{\hbar^2}{2m} \frac{d^2}{dr^2}, \quad (4.28)$$

which can be written in terms of the Fourier eigenfunctions of the grid to be

$$T_{ii'} = -\frac{\hbar^2}{2m} \Delta r \sum_{n=1}^{N-1} \phi_n(r_i) \phi_n''(r_{i'}), \quad (4.29)$$

with the grid spacing $\Delta r = (b-a)/N$. Inserting Eq. 4.27 into the above Equation yields

$$T_{ii'} = -\frac{\hbar^2}{2m} \left(\frac{\pi}{b-a} \right)^2 \frac{2}{N} \sum_{n=1}^{N-1} n^2 \sin \left[\frac{n\pi i}{N} \right] \sin \left[\frac{n\pi i'}{N} \right]. \quad (4.30)$$

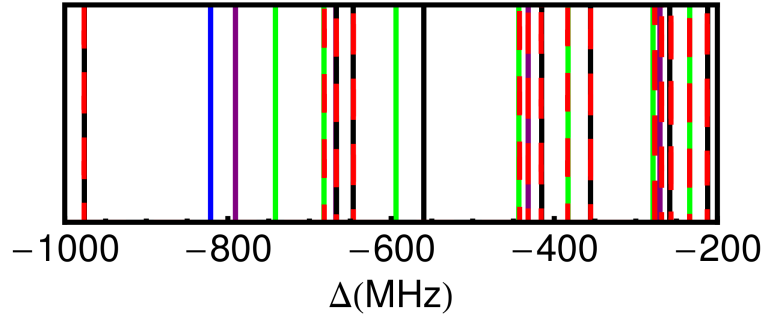


Figure 4.9: P-wave spectrum for the bound states of the excited states. The dashed (red) lines are the results experimental results from [81], while the solid lines are from the full multichannel calculation. As for s-waves, the agreement is good and there are some additional lines from the multichannel calculation which have very small Frank-Condon factors, such that they could not be seen experimentally. For the numerical values of the detuning, see also Table 4.4.

Evaluating the sum gives the following formulae for the diagonal and off-diagonal terms of the kinetic energy matrix

$$T_{ii} = \frac{\hbar^2}{2m} \frac{\pi^2}{2(b-a)^2} \left((2N^2 + 1)/3 - \frac{1}{\sin^2(\pi i/N)} \right) \quad (4.31a)$$

$$T_{ii'} = \frac{\hbar^2}{2m} \frac{\pi^2 (-1)^{(i-i')}}{2(b-a)^2} \left(\frac{1}{\sin^2[\pi(i-i')/2N]} - \frac{1}{\sin^2[\pi(i+i')/2N]} \right). \quad (4.31b)$$

For more details, see Appendix A from [89]. For a single channel, the potential matrix is a diagonal $(N-1) \times (N-1)$ matrix, which is added to the potential energy matrix derived above. For the multichannel problem the grid points and the different channels are treated on an equal footing, such that the resulting kinetic energy matrix is $N' \times N'$, where N' is the number of grid points times the number of channels. The diagonalization of the resulting matrix gives the eigenenergies and the full multichannel eigenfunctions.

The code used for this calculation was written by Julienne and Tiesinga at NIST, with minor adaptations for the parameters relevant for ^{171}Yb and the required number of channels. Since the potentials do not change very much at large r , but are relatively steep at small r , it is advantageous to have more grid points close to the

E_b^{theory} (MHz)	E_b^{exp} (MHz)	Γ_M (kHz)	l_{opt} (a ₀ /W/cm ²)
26.8	24.7	245	24967
34.9	—	89	6854
49.9	47.8	246	11673
89.1	86.9	248	5527
152.3	149.9	251	2969
250.2	247.0	256	1388
396.5	391.7	261	780
462.1	—	161	12
597.3	—	101	218
612.5	604.3	241	363

Table 4.3: Excited molecular bound states and resonance properties. E_b^{theory} are the binding energies found from the multichannel calculation solutions of the Schrödinger equation with Hamiltonian Eq. (4.14). Binding energies are denoted in frequency units relative to the atomic $^1S_0 \rightarrow ^3P_1(f = 3/2)$ transition. For comparison, E_b^{exp} are the photoassociation resonances observed by Enomoto *et al.* with an experimental uncertainty of ± 2 MHz. The agreement between experiment and theory is good, with a small systematic shift that may be attributed to inaccuracies in the Hund's case-(c) potentials, and/or to systematic shifts in the experimental conditions (e.g. light-shift from the confining dipole potential). Γ_M is the molecular natural linewidth and l_{opt} is the optical length at an intensity of 1 W/cm².

origin than at larger internuclear distances. However, the DVR method requires an evenly spaced grid. These seemingly contradictory requirements were both fulfilled by Tiesinga and Julienne by transforming to a different coordinate system in which

$$y = \frac{2}{2-n} \frac{\alpha}{(r-r_s)^{n/2-1}} + r, \quad (4.32)$$

where $\alpha = \sqrt{C_n/E_{kin}}$, with the kinetic energy E_{kin} and $n = 6$ for the used Lennard-Jones potentials. r_s is given by $2a - r_{min}$, where r_{min} is the approximate position of the minimum of the Lennard-Jones potential. Now the matrix for the DVR method is constructed on an evenly spaced grid in the coordinate system y .

The block-diagonal structure and, in the absence of magnetic fields, the degeneracies of the Hamiltonian can be exploited to greatly reduce the number of channels

and thus the CPU time required to diagonalize the Hamiltonian. For s-waves, the Hamiltonian can be reduced to one 5×5 matrix, while for p-waves, 4 different blocks have to be diagonalized, one with $T = 0$, which consists of two channels, one with $T = 1$, which is a 5×5 matrix, and the last two, with $T = 2$ and $T = 3$, respectively, both of which are 6×6 matrices (compare to table 4.2).

The resulting bound states represent photoassociation resonances that dissociate to $^1S_0 + ^3P_1(f = 3/2)$. Their positions relative to the atomic resonance were experimentally determined by Enomoto *et al.* [81], allowing for comparison between experiment and the numerical calculation. Fig. (4.8) and Table (4.3) both show results for s-wave collisions and Fig. (4.9) and Table (4.4) for p-wave collisions. The agreement is very good. For s-waves, there is a small systematic shift, which could be caused by the inaccuracies in the Hund's case c) potentials, or by systematic shifts in the experiment. However, for p-waves, the numerical calculation agrees with the experimental results to within the experimental uncertainty. For both s-waves and p-waves, there are additional lines in the calculated spectrum as compared to the experimental spectrum, which have not been found by Enomoto *et al.*, either because their binding is comparable to their lifetime or because they are too tightly bound and thus have small Franck-Condon factors.

4.3.4 Scattering Length

The DVR method also yields the multichannel eigenvectors of the bound excited states, which can be described as

$$|b\rangle = \sum_{\epsilon} \Psi_{\epsilon}(r)|\epsilon\rangle, \quad (4.33)$$

where $\Psi_{\epsilon}(r)$ are the radial eigenfunctions for given partial wave l for channel ϵ and $|\epsilon\rangle$ are the corresponding spin states in the ϵ basis. In contrast to the ground state wave functions, these bound states are unit normalized. These eigenfunctions can

be used to calculate both the Frank-Condon factors as well as the linewidth of the excited states, both of which are required for the calculation of the scattering length.

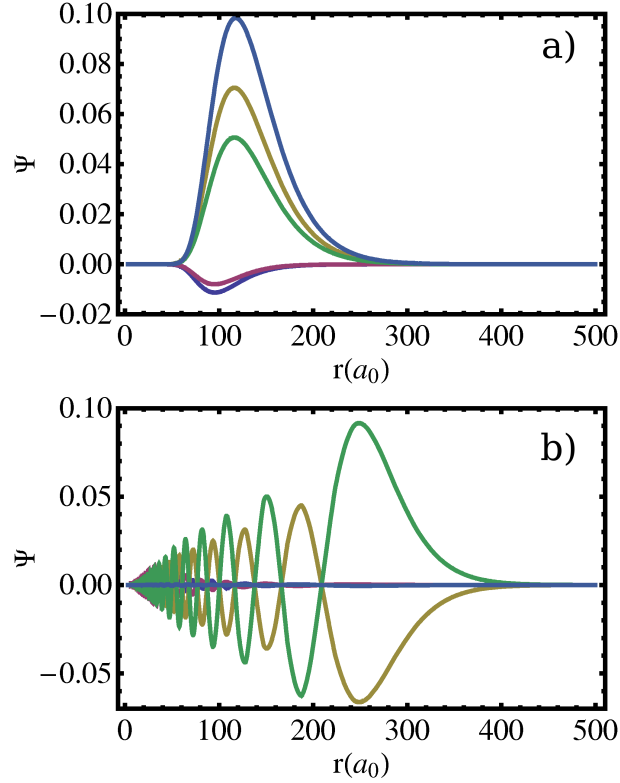


Figure 4.10: The radial parts of two multichannel eigenstates for s-wave scattering. a) shows the lowest purely long-range state for s-waves, which has a binding energy of 34.9 MHz relative to the atomic resonance. It can be seen that the complete amplitude of the purely long-range state is at large internuclear distance. b) shows the next lower multichannel state for s-waves, with a binding energy of 49.9 MHz. Even though this state has support ranging to very small r , the bulk of the amplitude is at even larger internuclear separation than for the purely long-range state, causing its Frank-Condon factor to be larger than the one for the latter.

The molecular linewidth is calculated in two steps [85], first a linewidth matrix is determined to be

$$\Gamma_{\epsilon\epsilon'} = \Gamma_A \frac{1}{d_A^2} \sum_{\epsilon_g} \langle \epsilon | (\hat{d}_{mol})_q | \epsilon_g \rangle \langle \epsilon_g | (\hat{d}_{mol})'_q | \epsilon' \rangle \quad (4.34)$$

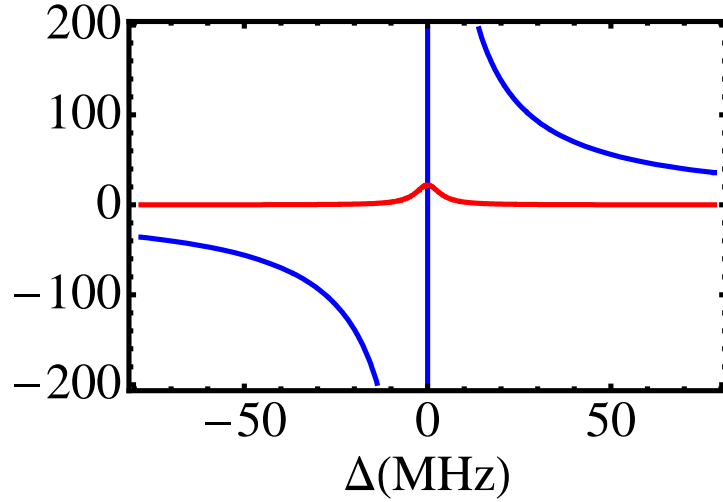


Figure 4.11: The resulting scattering length for s-wave optical Feshbach resonances at a temperature of $2 \mu\text{K}$. The solid (blue) line is the real part of the scattering length, while the dashed (red) line is the imaginary part, which quantizes the losses.

where $|\epsilon\rangle$ and $|\epsilon'\rangle$ are the spin parts of the basis states for the excited states in the ϵ basis, $|\epsilon_g\rangle$ are the spin states of the ground states, q and q' are the polarization of the photons, d_A is the atomic electric dipole matrix element and \hat{d}_{mol} is the molecular dipole operator. The matrix elements of the latter, $\langle\epsilon|(\hat{d}_{mol})_q|\epsilon_g\rangle$ are calculated by expanding the states in the π basis, as described by Eqs. (4.23) and (4.24) in section 4.2.3. Now the linewidth of the excited bound state can be obtained by integrating over the radial part of the wave functions (4.33), multiplied with the relevant elements of the linewidth matrix (4.34)

$$\Gamma_M = \sum_{ee'} \int_0^\infty dr \Psi_e(r) \Gamma_{ee'} \Psi_{e'}(r). \quad (4.35)$$

The resulting linewidths for several s-wave states are shown in table 4.3.

The Franck-Condon factor that measures the overlap between the spatial wave function of the (energy normalized) scattering ground electron state $|g\rangle$ at energy E and the (unit normalized) bound excited state $|b\rangle$ is given by [79]

$$f_{FC} = |\langle b | \mathbf{d} \cdot \epsilon_L | g \rangle|^2 / 2d_A^2, \quad (4.36)$$

where d_A is the atomic dipole moment for this transition and ϵ_L is the laser polarization. Given in Eq. (4.33), Eq. (4.36) can be expanded in the spin part and the radial part

$$f_{FC} = \left| \sum_{\epsilon} \langle \epsilon_g | d_{mol} | \epsilon \rangle \int_0^{\infty} dr \Psi_g(r) \Psi_{\epsilon}^*(r) \right|^2 / 2d_A^2, \quad (4.37)$$

Note that this definition of the Frank-Condon factor includes the spin part and is not limited to the integral over the spatial wave function, as is often the case.

Using this together with V_{opt} , given in Eq. (4.2) allows us to calculate the optical length, given in Eq. (4.8). The results for the s-wave photoassociation resonances near dissociation at a temperature of $2\mu\text{K}$ can be seen in Table 4.3. These are calculated at a laser intensity of 1 W/cm^2 . There are several states, among them the purely-long range states, for which the Frank-Condon factor and with it the optical length are comparatively small and therefore these states were not visible in the experiments by Enomoto *et al.* [81]. This is due to the fact that these states are relatively tightly bound.

The real and imaginary parts of the scattering length, given in Eqs. (4.6) and (4.7) can now be calculated as a function of laser intensity and detuning. Since the bare s-wave scattering length of ^{171}Yb , $a_{bg} = -2.83a_0$, is essentially zero, an OFR will increase $|a|$ by orders of magnitude, similar to that seen in ^{88}Sr [83]. The results for s-waves for a temperature of $2\mu\text{K}$ can be seen in Fig. 4.11. The p-wave scattering length is zero at this low temperature, since the centrifugal barrier is too high for the atoms to interact with each other.

4.4 Application to QIP

As described in section 4.3.1, the parity selection rules make it possible to selectively change s-waves and p-waves independently from each other. Additionally, as detailed

in section 2.2, due to symmetry, even partial waves are related to spin singlet state and odd partial waves to spin triplet states, allowing for the implementation of two-qubit gates via collisional nuclear spin exchange. The increase of the s-wave scattering length with the optical Feshbach resonances makes it possible to implement the two-qubit gate on shorter timescales than otherwise possible. Furthermore, it is in principle possible to set the p-wave scattering length to zero, thus improving the fidelity of the gate if p-wave interactions are not sufficiently suppressed due to low temperatures. In this section, however, I will examine a scheme to implement the gate at low enough temperature for s-wave collisions to be dominant interaction in more detail and will determine possible gate times and resulting fidelities. This proposal is shown schematically in Fig. 4.12

Assuming two atoms in the groundstate of the same optical trap makes it possible to estimate the duration and fidelity of a \sqrt{SWAP} gate. I assume a harmonic oscillator trap, comparable to the experiments by Anderlini *et al.* [38], with a ground state energy corresponding to a temperature of $2\mu\text{K}$. Without the Feshbach laser, the interaction between the atoms and thus the acquired phase shift is very small, owing to the tiny natural scattering length of $-2.83a_0$ for ^{171}Yb . The utility of the optical Feshbach resonance for coherent control of nuclear spin exchange depends on low loss and decoherence. As a figure of merit, consider the example of implementing a \sqrt{SWAP} two-qubit entangling unitary between the spin-1/2 nuclei trapped in one site of an optical lattice. As discussed in 2.2, such a gate occurs if the relative phase shift for singlet vs. triplet nuclear spin states is $\pi/2$. In the perturbative regime and neglecting the small background scattering length, the energy shift of two identical particles due to the interaction is given by $U = 4\pi\hbar^2na_{opt}/\mu$, where n is the atomic density. Since the p-wave scattering length is zero, the s-wave acquires a collisional phase shift $\phi = \int U/\hbar dt = U/\hbar T = (4\pi\hbar na_{opt}/\mu)T$ relative to the p-wave and the interaction time T for a \sqrt{SWAP} gate becomes then $T = \mu/(8\hbar na_{opt})$. As discussed in Chapter 2, the loss/decoherence rate is given by $Kn = 8\pi\hbar nb_{opt}/\mu$. The fidelity

of the gate based only on this loss is then

$$F = e^{-KnT} = e^{\pi b_{opt}/a_{opt}} \approx e^{-\left(\frac{\pi}{2}\right)\left(\frac{\Gamma_M}{\Delta}\right)}. \quad (4.38)$$

To get an estimate of how well the optical Feshbach resonance induces nuclear spin exchange, it is necessary to balance a variety of constraints. High fidelity at moderate intensities requires large detuning from molecular resonance, e.g., a fidelity of 95% is achieved when $\Delta \approx 30\Gamma_M$. Our model, however, assumes sufficiently small detuning so that a single molecular excited state contributes to the resonance. In addition, to ensure a reasonably fast interaction, the applied intensity must be sufficiently large so that the optical scattering length is large, which will power-broaden the atomic resonance $\Gamma_A \rightarrow \sqrt{1 + I/I_{sat}}\Gamma_A$. For all of these reasons, I consider as an example the photoassociation resonance bound by 396.5 MHz, with a natural linewidth of $\Gamma_M = 261$ kHz. This bound state is still relatively close to dissociation, and thus the molecule is long-range, with an outer turning point at $130 a_0$. Nonetheless, the density of states is sufficiently sparse that one can detune many linewidths from that resonance while still neglecting coupling to the next higher molecular state, which is bound by 250.2 MHz and has about twice the Franck-Condon factor. A detuning from the molecular resonance of $\Delta = -30\Gamma_M \approx -7.8\text{MHz}$ fits this constraint. The intensity is chosen to broaden the resonance so as to increase the scattering length by fixing $\Gamma_{stim} = 2k_r l_{opt}\Gamma_M = -\Delta$, or $l_{opt} = 30/k_r \approx 10^4 a_0$, at an energy of $2 \mu\text{K}$. From Table 4.3, this is achieved at an intensity of $I = 13.8 \text{ W/cm}^2$, whereby the atomic linewidth is power broadened to $\Gamma_A \rightarrow 59 \text{ MHz}$, which is still narrow compared to a detuning of 400 MHz from dissociation. When $-\Delta = \Gamma_{stim} \gg \Gamma_M$, the optical scattering length is $a_{opt} \approx -l_{opt}(4\Gamma_M/5\Delta) \approx -287 a_0$ and the loss coefficient is $Kn \approx 2.6 \times 10^{-16} \text{ cm}^3/\text{s}$. With this large magnitude scattering length and low loss, given two ^{171}Yb atoms in a lattice site analogous to the experiments at NIST [38], the time of the \sqrt{SWAP} gate is $T \approx 51.6 \mu\text{s}$ and the gate fidelity is $\approx 95\%$.

In principle, higher fidelity, larger scattering lengths, and shorter gate times are

possible, though a proper treatment will require the modelling of excitation to multiple molecular bound states and line broadening. Even with these modest parameters, we see that optical Feshbach resonances have great potential for control of nuclear-spin exchange and strong entangling interactions.

Note that this calculation does not take into account the change of the wave function in the lattice due to the potentially very large scattering length. Generally, for scattering lengths on the order of the confinement a self-consistent solution is required, owing to the shift of the trap energy due to the interaction between the particles [34]. It should be possible to utilize the large induced scattering length to control the state of the atoms via trap-induced shape resonances, when the atoms are in neighboring traps [37].

4.5 Conclusions

In this chapter, I described the calculation of the multichannel Hamiltonian for the $^1S_0 + ^3P_1$ molecular state of ^{171}Yb , an alkaline-earth like atom, including nuclear spin and hyperfine interaction as well as magnetic fields. Comparison of the resulting spectra with experimental results from photoassociation shows very good agreement. This calculation points out how to exploit the intercombination line for the implementation of optical Feshbach resonances, and allows for the prediction of resulting scattering lengths and useful transition energies and detunings. I discovered two potentials with magnetic-field-dependant barriers and shape resonances, and showed how the optical Feshbach resonances can be utilized for the manipulation of nuclear spins, which in turn allows the implementation for quantum information in alkaline-earth-like atoms. Nuclei do not directly interact, but instead act as a quantum switch due to the quantum statistics of identical particles [13], allowing or forbidding the laser coupling to long-range molecular bound states, and thereby allowing for optical control of nuclear spin-exchange over enormous distances when

compared to the scales of traditional chemistry.

The multichannel calculations pose some difficulties, given the fact that even ^{171}Yb , which has a nuclear spin of $1/2$ gives rise to 89 channels. Other elements with a larger nuclear spin will have even more channels. Fortunately, the Hamiltonian is block diagonal in the chosen basis, making the numerical calculation much more tractable. For ^{171}Yb , with its big hyperfine constant, the magnetic field will be small in comparison to the hyperfine splitting, thus f and m_f are good quantum numbers, and the Hamiltonian will be block diagonal for all experimentally relevant magnetic fields. This, however, is not necessarily true for elements with smaller hyperfine constant, possibly leading to a much more memory-intensive calculation.

In the near future, I plan on calculating the resulting Feshbach resonances for p-waves. Most of the required steps are already complete and only have to be put together. Another important direction for this project is the inclusion of multiple resonances at once, thus extending the current model of optical Feshbach resonances in which only one excited state resonance is considered. This might lead to interesting interference effects and more accurate calculations, especially for the case of very large detuning from a specific line, in which additional, higher lying bound states which usually have a larger Frank Condon factor can be coupled to the scattering state.

Optical Feshbach resonances open up new directions in the research of ultracold gases, lead to new possibilities in the implementation of quantum information processing and metrology and allow for the investigation of cold molecules. They extend the very interesting research that has been done in the control of scattering processes to additional elements without multiple hyperfine sublevels and allow for the additional use of magnetic fields in the control of atoms, which is impossible during the use of magnetic Feshbach resonances.

E_b^{theo} (MHz)	E_b^{exp} (MHz)	E_b^{theo} (MHz)	E_b^{exp} (MHz)
3.1	—	71.3	—
3.1	—	77.1	—
3.2	—	88.0	—
3.2	—	94.1	—
3.3	—	98.6	—
3.4	—	117.8	—
3.5	—	133.8	—
4.0	—	154.2	—
4.2	—	163.0	—
4.4	—	169.3	—
4.8	—	212.0*	212.4
5.5	—	233.8*	234.0
6.5	—	258.2	256.9
7.3	—	270.4	268.3
7.6	—	278.9	276.8
8.0	—	355.3*	355.4
12.2	—	383.2*	383.4
12.4	—	415.5	416.1
13.9	—	431.9	432.0
15.1	—	443.2	442.5
16.4	—	559.8	—
21.8	—	593.9	—
24.7	—	646.3	646.2
27.3	—	666.9	—
28.2	—	667.7	667.2
29.3	—	682.4	681.8
35.3	—	741.8	—
42.2	—	790.7	—
47.7	—	821.1	—
51.9	—	976.0	976.2
54.9	—	1003.5	1002.1
60.3	—	1022.1	1021.4

Table 4.4: P-wave accessible excited molecular bound states. E_b^{theo} are the binding energies found from the multichannel calculation as in Table 4.3. The lines which were also experimentally observed by Enomoto *et al.* at a temperature of $25\mu\text{K}$ are shown for comparison. Their experimental uncertainty is $\pm 2\text{MHz}$ and $\pm 1\text{MHz}$ for the PLR states denoted by *.

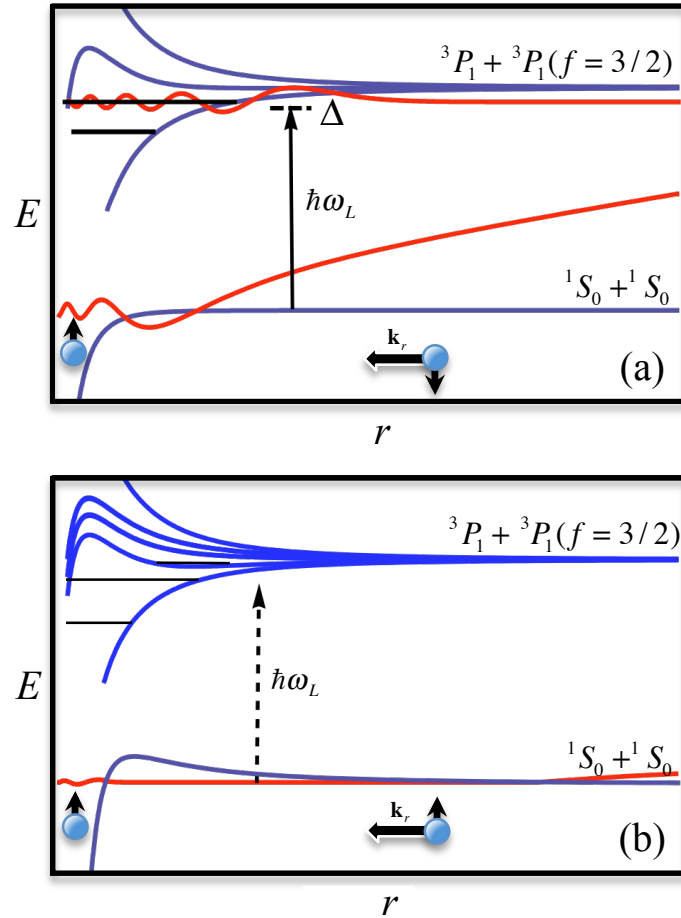


Figure 4.12: Schematic of the optical Feshbach resonance leading to nuclear spin exchange. Shown in (a) is the interaction for the case of a nuclear spin singlet state. A laser photon with energy $\hbar\omega_L$, detuned by Δ from a molecular bound state, excites two atoms colliding with relative momentum $\hbar k_r$ and relative angular momentum $l = 0$, which in turn leads to a phase shift for these s-waves. For nuclear spin triplet, s-wave collisions are forbidden by the Pauli exclusion principle. Shown in (b) is a p-wave scattering state for the spin polarized nuclei and a different set of excited potentials, accessible according to the selection rules. The p-wave phase shift is negligible because low energy collisions cannot penetrate the centrifugal barrier into the region, and thus laser photons cannot excite bound molecules due to the negligible Franck-Condon overlap. The relative phase between s-wave and p-wave collisions correlates with a relative phase between nuclear spin singlet and triplet, and thus leads to a nuclear spin-exchange force.

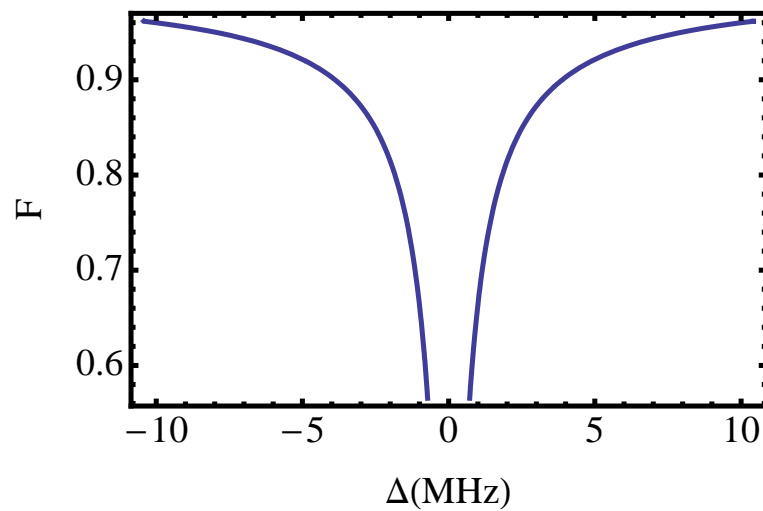


Figure 4.13: The fidelity of a \sqrt{SWAP} gate assuming a temperature of $2 \mu\text{K}$ and a laser power of 1 W/cm^2 . It can be seen that the loss of fidelity due to the imaginary part of the scattering length b_{opt} is reasonably small, depending on the detuning.

Chapter 5

Summary and Outlook

In this thesis I discussed several aspects of quantum control of alkaline-earth-like atoms, particularly in the context of the implementation of QIP. Due to their rich but tractable internal structure, decoupled nuclear spin in the ground state and both conveniently accessible and extremely narrow intercombination transitions, alkaline-earth-like atoms are particularly well suited for these applications, as well as for the implementation of atomic clocks. The possibility to store quantum information in the nuclear spin allows for very long coherence times, while the application of Feshbach resonances allow for relatively fast gates.

As discussed in Chapter 3, the unique properties of alkaline-earth-like atoms make it possible to recool the vibrational degrees of freedom of nuclear-spin qubits via laser cooling, by utilizing magnetic fields and thus decoupling the nuclear spin from the electronic angular momentum in the excited 3P_0 state. Alternatively, the combination of magnetic fields and off-resonant scattering requires weaker magnetic fields, thus posing some advantages for ^{171}Yb . Since the manipulation of qubits usually causes their heating, which generally leads to increased decoherence and degrading of the fidelity of qubit gates, the ability to recool the qubits with relative ease is an important stepping stone towards a truly scalable quantum computer.

With the protocol explained in Chapter 3 in detail for both ^{171}Yb and ^{87}Sr and published in [30], it is possible to recool the qubits between and even during the implementation of successive qubit gates.

In Chapter 4, I examined the promise of alkaline-earth-like atoms for the implementation of optical Feshbach resonances. Calculation of the relevant parameters requires very accurate modeling of both the ground state potentials and the excited state potentials, including rotation, hyperfine interaction, and magnetic fields. Comparison of the resulting spectra with experimental results from photoassociation shows very good agreement. This was the first calculation including all these effects in alkaline-earth-like atoms. Due to the symmetry of the problem, it is possible to change the scattering length of s-waves and p-waves independently from each other, allowing unprecedented control over the scattering properties of these ultracold atoms. Additionally, in the progress of this work I discovered that the extremely shallow purely long-range potentials of ^{171}Yb for s-waves change their shape and develop a barrier in the presence of a magnetic field. Furthermore, I showed how strong entangling interactions can be induced between nuclei over hundreds of angstroms based on optical Feshbach resonances between pairs of ^{171}Yb atoms. Nuclei do not directly interact, but instead act as a quantum switch due to the quantum statistics of identical particles [13], allowing or forbidding the laser coupling to long-range molecular bound states, and thereby allowing for optical control of nuclear spin-exchange over enormous distances when compared to the scales of traditional chemistry. The combination of this tool, together with recent advances in loading optical lattices via superfluid to mott-insulator phase transition [19], the ability to optically manipulate nuclear spin coherence [52] and re-cool atoms without decohering nuclear spins, and proposals for quantum logic [13, 22, 66] make this system attractive for new applications in quantum information processing.

The work described in this dissertation suggests several logical directions for additional research. For the resolved-sideband cooling scheme, there might be possibil-

ities other than strong magnetic fields to decouple the nuclear spin from the electron angular momentum, for example dynamical decoupling with optical or microwave fields. However, preliminary research in this direction has not yielded useful results.

In the context of the optical Feshbach resonances described in Chapter 4, there are more additional directions for research possible. The first logical step is to calculate the optically induced scattering lengths for p-waves in detail, and to find the laser intensities and frequencies required for the independent manipulation for s-waves and p-waves. Additionally, while the calculation is set up to allow for the inclusion of magnetic fields, no systematic investigation of the effects of magnetic fields on the different levels of the excited states and on the optical Feshbach resonances has yet been carried out. The inclusion of magnetic fields is especially important in the light of the resolved-sideband cooling scheme described in Chapter 3, which requires a strong magnetic field. Furthermore, the manipulation of the purely-long range states for s-waves with magnetic fields induces barriers in the potentials, which can potentially lead to shape-resonances, when a scattering state, which is at the same energy as a quasi-bound state, tunnels through the barrier. This should allow for large scattering lengths for excited scattering states of a well-defined and controllable energy.

Another important step in the calculation of optical Feshbach resonances is the inclusion of several excited states instead of only the state with the highest Condon-factor. This is especially important for large detunings, since then optical coupling to several different excited states at once can play a role. This can possibly lead to interferences between the optical Feshbach resonances to the different levels, rendering the predictions of a single state model inaccurate. Due to the close relationship of photoassociation and optical Feshbach resonances, the accurate determination of the excited state potentials required for the prediction of optical Feshbach resonances is the same as for the prediction of photoassociation. Therefore, the calculation in this dissertation can be used as a help in the quest for the production of ultracold

molecules, a difficult task due to the absence of cycling transitions for optical cooling in molecules. However, photoassociation could make the production of ultracold molecules possible, e.g. by applying it to an optical lattice with two atoms per lattice site, thus creating an optical lattice with one molecule per lattice site.

In addition to being the basis of quantum information processing, the ability to implement entangling two-body interactions between atoms can be utilized in the improvement of atomic clocks, thus leading to new basic research, e. g. in the investigation of the time-dependence of fundamental constants. The accuracy of atomic clocks scales as a/\sqrt{N} for unentangled particles, however, if the N atoms that are interrogated for the clock are in an entangled state, accuracy scales as $1/N$. Thus, for a clock consisting of alkaline-earth-like atoms in an optical lattice, the accuracy can be noticeably improved by first entangling the atoms with each other and then implementing the clock.

There are also several more long-term prospects in the continuation of this research, e. g. the combination of optical Feshbach resonances with confinement-induced shape resonances, which were described by Stock *et al.* [90]. These resonances occur when two traps with one atom confined in each are moved relative to each other. The molecular potential of the two atoms is shifted up depending on the relative distance between the centers of the traps, and for the right distance between the traps the highest molecular bound state is resonant with the trap eigenstates, causing an avoided crossing in the energies of the trap eigenstates. The size of the effect depends on the scattering length of the trapped atoms and a large scattering length is necessary to observe this effect. Therefore, increasing the scattering length via optical Feshbach resonances can help in observing this effect in alkaline-earth-like atoms. This can be used in the implementation of quantum information processing, by implementing gates between two atoms in neighboring traps, as described for alkali-atoms in [28]. The difference to the system described here is that the qubits are stored in the nuclear spin of the alkaline-earth-like atoms. Further-

more, confinement-induced shape resonances can also be used for the creation of cold molecules, in that the scattering length between two atoms in neighboring traps is increased, causing the avoided crossing. Then the traps are slowly moved together, with the atoms adiabatically following the avoided crossing, and thus being transferred to the molecular bound states.

Since optical Feshbach resonances can be controlled with much higher temporal and spatial resolution than magnetic Feshbach resonances, their application opens the door to new experiments in many-body physics. One example of this is the possibility to overlay an ultracold gas of atoms in an optical lattice with optical Feshbach lasers of spatially varying intensity. This would allow for a trapped quantum gas which has different regions with varying scattering lengths and is thus in different quantum phases, making new research in the investigation of quantum phase transitions possible. Additionally, combining spatially varying optical Feshbach resonances with the scheme to produce cold molecules with confinement-induced resonances as described above, allows for the creation of an optical lattice which is partly filled with ultracold molecules and partly with ultracold atoms, with control of the exact position of the different phases in the optical lattice.

The multichannel calculation, while very accurate, poses some challenges. Due to the large number of channels for higher partial waves or larger nuclear spin, the size of the matrix that has to be diagonalized can become rather large. Even though ^{171}Yb has a nuclear spin of only $1/2$, the number of channels required for the p-wave calculation is already 89. While this can easily be simplified due to fact that the Hamiltonian is block-diagonal under some circumstances, this is not necessarily always the case, especially in the presence of very high magnetic fields. Therefore, the requirements on the cpu-time and especially memory can easily get too high for practical purposes, depending on the nuclear spin and the desired partial waves.

Altogether, I hope that this dissertation has shed some light on the fact that trapped, ultracold alkaline-earth-like atoms are a very promising system for quan-

tum control and quantum information processing. They have the potential to open up new avenues for interesting basic research and applications and to contribute to the impressive renewal of AMO physics of the last few decades, as well as to the implementation of quantum information processing. Hopefully, additional experimental and theoretical studies will lead to the realization of this potential.

Appendices

A Programs	108
A.1 Calculation of the Breit-Rabi spectrum	108
A.2 Inclusion of the quadrupole part for Sr	117
A.3 Calculation of the multichannel Hamiltonian	124
A.4 Determination of the optically induced scattering length	138

Appendix A

Programs

In this appendix I will show several different Mathematica programs which were used for the calculations described in different parts of this dissertation.

A.1 Calculation of the Breit-Rabi spectrum

This Mathematica program was used to calculate the spectrum for ^{171}Yb in a magnetic field as well as the different resulting c-factors from Eq. (3.40) and the fidelity resulting from application of the magnetic field for the cooling scheme described in Chapter 3

Derivation of the Breit-Rabi formula

```
In[1]:= HBR = {{1/2 A (mi - 1/2) + B (gJ μB/2 - gi μN (mi - 1/2)), A/2 Sqrt[i (i + 1) - (mi - 1/2) (mi + 1/2)]},
             {A/2 Sqrt[i (i + 1) - (mi - 1/2) (mi + 1/2)], -A/2 (mi + 1/2) + B (-gJ μB/2 - gi μN (mi + 1/2))}};
```

```
In[2]:= MatrixForm[HBR]
```

```
Out[2]/MatrixForm=
```

$$\begin{pmatrix} \frac{1}{2} A \left(-\frac{1}{2} + mi\right) + B \left(\frac{gJ \mu B}{2} - gi \left(-\frac{1}{2} + mi\right) \mu N\right) & \frac{1}{2} A \sqrt{i (1 + i) - \left(-\frac{1}{2} + mi\right) \left(\frac{1}{2} + mi\right)} \\ \frac{1}{2} A \sqrt{i (1 + i) - \left(-\frac{1}{2} + mi\right) \left(\frac{1}{2} + mi\right)} & -\frac{1}{2} A \left(\frac{1}{2} + mi\right) + B \left(-\frac{gJ \mu B}{2} - gi \left(\frac{1}{2} + mi\right) \mu N\right) \end{pmatrix}$$

```
In[3]:= FullSimplify[Eigenvalues[HBR]]
```

$$\text{Out[3]} = \left\{ \frac{1}{4} \left(-A - 4 B gi mi \mu N - \sqrt{(A + 2 A i)^2 + 8 A B mi (gJ \mu B + gi \mu N) + 4 B^2 (gJ \mu B + gi \mu N)^2} \right), \right. \\ \left. \frac{1}{4} \left(-A - 4 B gi mi \mu N + \sqrt{(A + 2 A i)^2 + 8 A B mi (gJ \mu B + gi \mu N) + 4 B^2 (gJ \mu B + gi \mu N)^2} \right) \right\}$$

This is the Breit-Rabi formula

$$E_{mJmi} = -\frac{h\nu_{\text{HFS}}}{2(2I+1)} - g_I \mu_N B m +/ - \frac{h\nu_{\text{HFS}}}{2} \sqrt{1 + \frac{mx}{2I+1} + x^2}$$

with

$$x = \frac{B(g_I \mu_B + g_J \mu_N)}{h\nu_{\text{HFS}}}$$

and

$$h\nu_{\text{HFS}} = A(i+1/2)$$

In the common Breit-Rabi formula $J=1/2$, in our case we have instead $I=1/2$, which shouldn't change very much, calculation is below.

I=1/2, J arbitrary

```
In[4]:= Clear["Global`*"];
```

```
In[5]:= Hmag =
```

```
{ {1/2 A (mF - 1/2) + B (gJ μB (mF - 1/2) - gi μN/2), A/2 Sqrt[J (J + 1) - (mF - 1/2) (mF + 1/2)]},
  {A/2 Sqrt[J (J + 1) - (mF - 1/2) (mF + 1/2)], -A/2 (mF + 1/2) + B (gJ μB (mF + 1/2) + gi μN/2)}};
```

```
In[6]:= MatrixForm[Hmag]
```

```
Out[6]/MatrixForm=
```

$$\begin{pmatrix} \frac{1}{2} A \left(-\frac{1}{2} + mF\right) + B \left(gJ \left(-\frac{1}{2} + mF\right) \mu B - \frac{gi \mu N}{2}\right) & \frac{1}{2} A \sqrt{J (1 + J) - \left(-\frac{1}{2} + mF\right) \left(\frac{1}{2} + mF\right)} \\ \frac{1}{2} A \sqrt{J (1 + J) - \left(-\frac{1}{2} + mF\right) \left(\frac{1}{2} + mF\right)} & -\frac{1}{2} A \left(\frac{1}{2} + mF\right) + B \left(gJ \left(\frac{1}{2} + mF\right) \mu B + \frac{gi \mu N}{2}\right) \end{pmatrix}$$

2 | *breitabi_thesis.nb*

In[7]:= **FullSimplify[Eigensystem[Hmag]]**

$$\text{Out[7]} = \left\{ \left\{ -\frac{A}{4} + B \, gJ \, mF \, \mu B - \frac{1}{4} \sqrt{(A + 2 A J)^2 - 8 A B mF (gJ \mu B + gi \mu N) + 4 B^2 (gJ \mu B + gi \mu N)^2}, \right. \right. \\ \left. \frac{1}{4} \left(-A + 4 B \, gJ \, mF \, \mu B + \sqrt{(A + 2 A J)^2 - 8 A B mF (gJ \mu B + gi \mu N) + 4 B^2 (gJ \mu B + gi \mu N)^2} \right) \right\}, \\ \left\{ \left\{ -\frac{A \sqrt{(1 + 2 J)^2 - 4 mF^2}}{2 A mF - 2 B (gJ \mu B + gi \mu N) + \sqrt{(A + 2 A J)^2 - 8 A B mF (gJ \mu B + gi \mu N) + 4 B^2 (gJ \mu B + gi \mu N)^2}}, 1 \right\}, \right. \\ \left. \left\{ \frac{A \sqrt{(1 + 2 J)^2 - 4 mF^2}}{-2 A mF + 2 B (gJ \mu B + gi \mu N) + \sqrt{(A + 2 A J)^2 - 8 A B mF (gJ \mu B + gi \mu N) + 4 B^2 (gJ \mu B + gi \mu N)^2}}, 1 \right\} \right\}$$

Now: use real units

■ Constants:

In[8]:= **Clear["Global`*"];**

In[9]:= **c = 3 * 10⁸ m / s;**
m = 9.109 * 10⁻³¹ kg;
e = 1.602 * 10⁻¹⁹ C;
hbar = 1.055 * 10⁻³⁴ kg m² / s;
e0 = 8.85418 * 10⁻¹² C² s² / (kg m⁴);
M = 1.6726 * 10⁻²⁷ kg;
 $\mu B = \frac{e \, hbar}{2 \, m}$;
 $\mu N = m / M \, \mu B$;

Careful: Bohr magneton is $\frac{e \, hbar}{2 \, m c}$ in cgs units.

In[17]:= **c = 3 * 10⁸;**
m = 9.109 * 10⁻³¹;
e = 1.602 * 10⁻¹⁹;
hbar = 1.055 * 10⁻³⁴;
e0 = 8.85418 * 10⁻¹²;
M = 1.6726 * 10⁻²⁷;
 $\mu B = \frac{e \, hbar}{2 \, m}$;
 $\mu N = m / M \, \mu B$;

Simply using everything in GigaHertz and Gauss

m = 9.109 * 10⁻³¹;
M = 1.6726 * 10⁻²⁷;
 $\mu B = 1.4 * 10^{-3}$;
 $\mu N = m / M \, \mu B$;

Using everything in Gigahertz/T, (I only have to change μB for this)

```

In[25]:= m = 9.109 * 10-31;
          M = 1.6726 * 10-27;
          μB = 14;
          μN = m / M μB;

In[29]:= $TextStyle = {FontSize -> 15, FontFamily -> Times};

```

■ For 171 Ytterbium 1P1

```
In[30]:= A = -.2;
```

```
In[31]:= J = 1;
```

```
In[32]:= gi = 0.9915512130859588 `;
          gJ = 1.035;
```

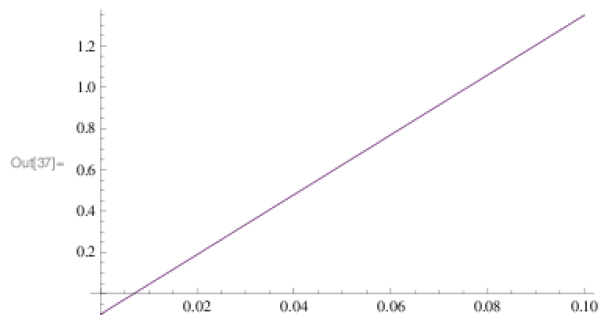
```

In[34]:= sol1[B_, mF_] = - $\frac{A}{4} + B gJ mF \mu B - \frac{1}{4} \sqrt{(A + 2 A J)^2 - 8 A B mF (gJ \mu B + gi \mu N) + 4 B^2 (gJ \mu B + gi \mu N)^2}$ ;
          sol2[B_, mF_] =  $\frac{1}{4} \left( -A + 4 B gJ mF \mu B + \sqrt{(A + 2 A J)^2 - 8 A B mF (gJ \mu B + gi \mu N) + 4 B^2 (gJ \mu B + gi \mu N)^2} \right)$ ;
          solstretched[B_, mF_] = A / 2 J + B (Sign[mF] (Abs[mF] - 1 / 2) gJ μB - gi μN Sign[mF] / 2);

```

That was unnecessary: sol1[B,+/- 3/2]=solstretched[B,+/- 3/2]

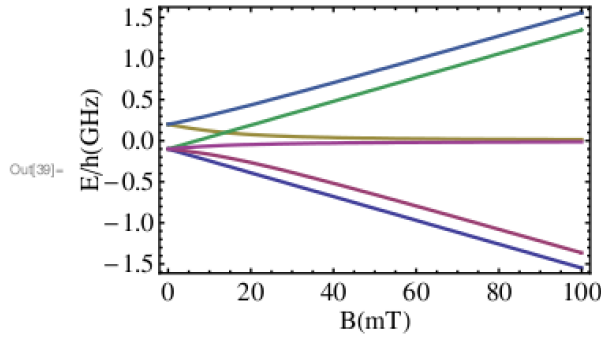
```
In[37]:= Plot[{solstretched[B, 3/2], sol1[B, 3/2]}, {B, 0, 0.1 `}]
```



```
In[38]:=
```

4 | breitrabi_thesis.nb

```
In[39]:= Plot[{solstretched[B/1000, -3/2], sol1[B/1000, -1/2], sol2[B/1000, -1/2],
  solstretched[B/1000, 3/2], sol2[B/1000, 1/2], sol1[B/1000, 1/2]}, {B, 0, 100}, Axes → False,
  Frame → True, FrameStyle → Thickness[0.005], FrameLabel → {"B (mT)", "E/h (GHz)"},
  PlotStyle → Thick, BaseStyle → {FontSize → 15, FontFamily → Times}]
```



What magnetic fields are required for the crossing in the $m_j = -1$ manifold to occur?

```
In[40]:= Solve[solstretched[B, -3/2] == sol1[B, -1/2], B]
```

```
Out[40]:= {{B → -5.3367 × 10-19}, {B → 26.4481}}
```

```
In[41]:= 264481.25143774285`
```

```
Out[41]:= 264481.
```

■ General error probability

```
In[42]:= mF = . ;
  B = . ;
```

$$\text{In[44]:= } c1[B_, mF_] = \frac{A \sqrt{(1 + 2J)^2 - 4mF^2}}{-2AmF + 2B gJ \mu B + 2B g_i \mu N + \sqrt{(A + 2AJ)^2 - 8ABmF(gJ \mu B + g_i \mu N) + 4B^2(gJ \mu B + g_i \mu N)^2}};$$

$$\text{In[45]:= } c2[B_, mF_] = -\frac{A \sqrt{(1 + 2J)^2 - 4mF^2}}{2AmF - 2B(gJ \mu B + g_i \mu N) + \sqrt{(A + 2AJ)^2 - 8ABmF(gJ \mu B + g_i \mu N) + 4B^2(gJ \mu B + g_i \mu N)^2}};$$

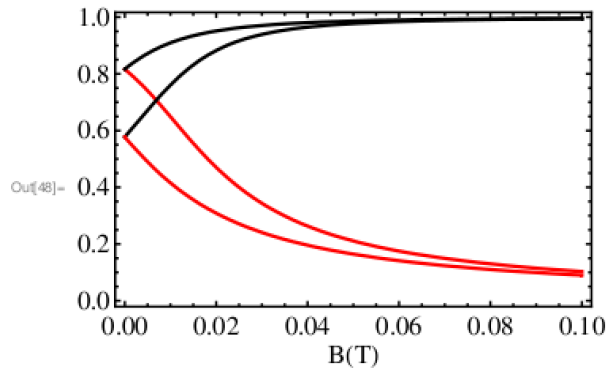
$$\text{In[46]:= } \text{error1}[B_] = \left(\frac{c1[B, -1/2]}{\sqrt{c1[B, -1/2]^2 + 1}} \right)^2;$$

$$\text{In[47]:= } \text{error2}[B_] = \left(\frac{1}{\sqrt{c2[B, 1/2]^2 + 1}} \right)^2;$$


```

In[48]:- P1 = Plot[ {Abs[  $\frac{c1[B, -\frac{1}{2}]}{\sqrt{c1[B, -\frac{1}{2}]^2 + 1}}$  ], Abs[  $\frac{c2[B, -\frac{1}{2}]}{\sqrt{c2[B, -\frac{1}{2}]^2 + 1}}$  ], Abs[  $\frac{c1[B, \frac{1}{2}]}{\sqrt{c1[B, \frac{1}{2}]^2 + 1}}$  ],
Abs[  $\frac{c2[B, \frac{1}{2}]}{\sqrt{c2[B, \frac{1}{2}]^2 + 1}}$  ] }, {B, 0, 0.1`}, Frame -> True, FrameLabel -> {"B(T)", None},
PlotStyle -> {{Thick, Red}, {Thick, Black}, {Thick, Red}, {Thick, Black}},
BaseStyle -> {FontSize -> 15, FontFamily -> Times}, FrameStyle -> Thickness[0.005`] ]

```



```

In[49]:- SetOptions[Plot, Axes -> False, Frame -> True];

```

```

In[50]:- error1[0]

```

```

Out[50]- 0.666667

```

```

In[51]:- error2[0]

```

```

Out[51]- 0.333333

```

```

In[52]:- error1[0.1]
error2[0.1]

```

```

Out[52]- 0.0106291

```

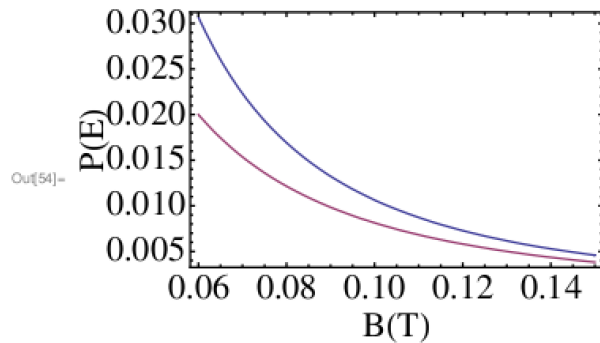
```

Out[53]- 0.00812486

```

6 | breitrabi_thesis.nb

```
In[54]:= Plot[{error1[B], error2[B]}, {B, 0.06, 0.15}, BaseStyle -> {FontSize -> 20},
  FrameLabel -> {"B(T)", "P(E)"}, FrameStyle -> Thickness[0.005], PlotStyle -> Thickness[0.005]]
```



■ For really high magnetic fields

```
In[55]:= B = 100;
```

```
In[56]:= {sol1[B, 1/2], sol1[B, -1/2], sol2[B, 1/2],
  sol2[B, -1/2], solstretched[B, -3/2], solstretched[B, 3/2]}
```

```
Out[56]:= {-0.378014, -1449.28, 1449.48, 0.378014, -1448.72, 1448.52}
```

```
In[57]:= B = 106;
```

```
In[58]:= {sol1[B, 1/2], sol1[B, -1/2], sol2[B, 1/2],
  sol2[B, -1/2], solstretched[B, -3/2], solstretched[B, 3/2]}
```

```
Out[58]:= {-3780., -1.44938 × 107, 1.44938 × 107, 3780., -1.44862 × 107, 1.44862 × 107}
```

■ Reasonable fields

```
In[59]:= B = 0.100;
```

```
In[60]:= {solstretched[B, -3/2], sol1[B, -1/2], sol1[B, 1/2],
  sol2[B, -1/2], solstretched[B, 3/2], sol2[B, 1/2]}
```

```
Out[60]:= {-1.54862, -1.36404, -0.0131775, 0.0150363, 1.34862, 1.56218}
```

■ New Ansatz: Combining error rate due to decay and differential detuning in one

```
In[61]:= $TextStyle = {FontSize -> 15, FontFamily -> Times};
  SetOptions[Plot, Axes -> False, Frame -> True, FrameStyle -> Thickness[0.005]];
```

First: Calculate the undesired overlapp $|\langle \text{down} | b \rangle|^2$ and $|\langle \text{up} | a \rangle|^2$ of the different states to obtain γ_{up} and γ_{down} which is given by $\Gamma |\langle \text{down} | b \rangle|^2$ and $\Gamma |\langle \text{up} | a \rangle|^2$, respectively

```
In[63]:= B = .;
```

```
In[64]:=  $\Gamma = 28 * 10^{-3}$ ;
```

Gamma in GHz

```

In[65]:- c1[B_, mF_] :=

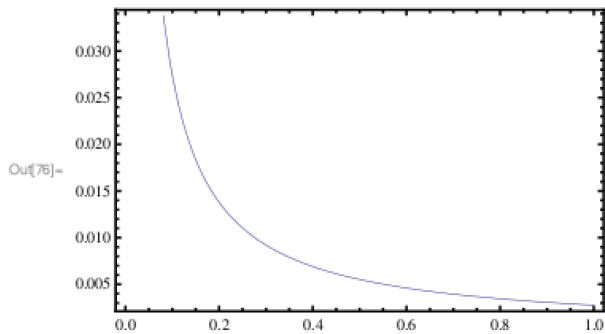
$$\frac{A \sqrt{(1 + 2 J)^2 - 4 mF^2}}{-2 A mF + 2 B g J \mu B + 2 B g i \mu N + \sqrt{(A + 2 A J)^2 - 8 A B mF (g J \mu B + g i \mu N) + 4 B^2 (g J \mu B + g i \mu N)^2}};$$

In[66]:- c2[B_, mF_] :=

$$\frac{A \sqrt{(1 + 2 J)^2 - 4 mF^2}}{2 A mF - 2 B (g J \mu B + g i \mu N) + \sqrt{(A + 2 A J)^2 - 8 A B mF (g J \mu B + g i \mu N) + 4 B^2 (g J \mu B + g i \mu N)^2}};$$

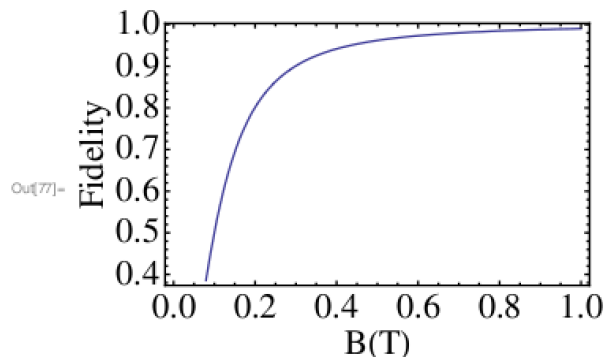
In[67]:- error1[B_] :=  $\left( \frac{c1[B, -1/2]}{\sqrt{c1[B, -1/2]^2 + 1}} \right)^2;$ 
In[68]:- error2[B_] :=  $\left( \frac{1}{\sqrt{c2[B, 1/2]^2 + 1}} \right)^2;$ 
In[69]:-  $\gamma_{up}[B_] := \Gamma \text{error1}[B];$ 
 $\gamma_{down}[B_] := \Gamma \text{error2}[B];$ 
Double check whether  $\gamma$  ups really  $\gamma$  upr  $\gamma$  down!
In[71]:-  $\Delta e[B_] := \text{sol1}[B, 1/2] - \text{sol2}[B, -1/2];$ 
 $\Delta g[B_] := -\mu N B g i$ 
In[73]:-  $g i$ 
Out[73]:- 0.991551
In[74]:-  $\delta[B_] := \Delta g[B] - \Delta e[B]$ 
In[75]:-  $\text{transfer}[B_] := \frac{\Gamma^2 (1 - \text{error1}[B]) (1 - \text{error2}[B])}{\Gamma^2 + \delta[B]^2}$ 
In[76]:-  $\text{Plot}[\delta[B], \{B, 0, 1\}]$ 

```



8 | breitrabi_thesis.nb

```
In[77]:= P1 = Plot[transfer[B], {B, 0, 1},
  BaseStyle -> {FontSize -> 20, FontFamily -> Times}, FrameLabel -> {"B(T)", "Fidelity"},
  FrameStyle -> Thickness[0.005`], PlotStyle -> Thickness[0.005`] ]
```



Zeeman effect in the $^3 P_1$ state of ^{171}Yb

```
Clear["Global`*"];
```

```
$TextStyle = {FontFamily -> "Arial", FontSize -> 15};
SetOptions[Plot, Axes -> False, Frame -> True];
```

■ Constants:

(everything in GigaHertz and Gauss)

```
m = 9.109 * 10-31;
```

```
M = 1.6726 * 10-27;
```

```
 $\mu_B = 1.4 * 10^{-3}$ ;
```

```
 $\mu_N = m / M \mu_B$ ;
```

```
A = 3.958;
```

```
J = 1;
```

```
gi = 0.9915512130859588`;
```

```
gJ = 1.5;
```

```
sol1[B_, mF_] = - $\frac{A}{4}$  + B gJ mF  $\mu_B$  -  $\frac{1}{4} \sqrt{(A + 2 A J)^2 - 8 A B mF (gJ \mu_B + gi \mu_N) + 4 B^2 (gJ \mu_B + gi \mu_N)^2}$ ;
```

```
sol2[B_, mF_] =  $\frac{1}{4} \left( -A + 4 B gJ mF \mu_B + \sqrt{(A + 2 A J)^2 - 8 A B mF (gJ \mu_B + gi \mu_N) + 4 B^2 (gJ \mu_B + gi \mu_N)^2} \right)$ ;
```

```
solstretched[B_, mF_] = A / 2 J + B (Sign[mF] (Abs[mF] - 1 / 2) gJ  $\mu_B$  - gi  $\mu_N$  Sign[mF] / 2);
```

```
Plot[{solstretched[B, - $\frac{3}{2}$ ], sol1[B, - $\frac{1}{2}$ ], sol2[B, - $\frac{1}{2}$ ], solstretched[B,  $\frac{3}{2}$ ], sol2[B,  $\frac{1}{2}$ ],
```

```
sol1[B,  $\frac{1}{2}$ ]], {B, 0, 1100}, Axes -> False, Frame -> True, FrameLabel -> {"B(Gauss)", "E/h(GHz)"}]
```

A.2 Inclusion of the quadrupole part for Sr

This program is similar to the one in Appendix [A.1](#), but it includes the quadrupole part of the Zeeman interaction and is thus suitable for ^{87}Sr . It was thus used to numerically calculate the spectrum for ^{87}Yb in a magnetic field and the fidelity for the cooling scheme described in Chapter [3](#)

Hyperfine effect for ^{87}Sr including quadrupole effect

For the 1P_1 state

```
Clear["Global`*"];
$TextStyle = {FontSize -> 15, FontFamily -> Times};
SetOptions[Plot, Axes -> False, Frame -> True, FrameStyle -> Thickness[0.005]];
```

I call the quadrupole constant here const to avoid confusion with the magnetic field and I multiply the other constants with B, such that $\text{const} = 3 B / (2 i j - i(i+1)j(j+1)/3)$. The other part of the quadrupole effect, $1/2 i j - i(i+1)j(j+1)/3$ is ignored so far, will be put in later.

```
Quadrupole[mF_] =
  { { const (mF + 1)^2 + 1/2 const (i (i + 1) - mF (mF + 1)), -const / sqrt[2] sqrt[i (i + 1) - mF (mF + 1)] (mF + 1),
    1/2 const sqrt[i (i + 1) - (mF - 1) mF] sqrt[i (i + 1) - mF (mF + 1)] },
    { -const / sqrt[2] sqrt[i (i + 1) - mF (mF + 1)] (mF + 1), const (i (i + 1) - mF^2),
    const / sqrt[2] sqrt[i (i + 1) - (mF - 1) mF] (mF - 1) },
    { 1/2 const sqrt[i (i + 1) - (mF + 1) mF] sqrt[i (i + 1) - mF (mF - 1)],
    const / sqrt[2] sqrt[i (i + 1) - (mF - 1) mF] (mF - 1), const (mF - 1)^2 + 1/2 const (i (i + 1) - mF (mF - 1)) } };
```

```
quadrupole2 = -const / 3 i (i + 1) J (J + 1) { {1, 0, 0}, {0, 1, 0}, {0, 0, 1} };
```

```
dipoleandmagnetic[B_, mF_] :=
  { { -A (mF + 1) - B (gJ muB + gJ muN (mF + 1)), A / 2 sqrt[99 / 4 - mF (mF + 1)] sqrt[2], 0 },
    { A / 2 sqrt[99 / 4 - mF (mF + 1)] sqrt[2], -B gI muN mF, A / 2 sqrt[99 / 4 - mF (mF - 1)] sqrt[2] },
    { 0, A / 2 sqrt[99 / 4 - mF (mF - 1)] sqrt[2], A (mF - 1) + B (gJ muB - gJ muN (mF - 1)) } };
```

```
General::spell1: Possible spelling error:
  new symbol name "muN" is similar to existing symbol "muB". More...
```

```
HFSr[B_, mF_] = dipoleandmagnetic[B, mF] + Quadrupole[mF] + quadrupole2;
```

μ Bn Megahertz/Gauss

```
BHF = 39;
A = -3.4 + 3/2 BHF / (2 i J (2 i - 1) (2 J - 1));
gI = -1.0924 * 2 / 9;
J = 1;
i = 9 / 2;
gJ = 1;
const = 3 BHF / (2 i J (2 i - 1) (2 J - 1));
```

A = -3.4 MHz is for 1P_1

2 | *quadrupolegraph_thesis.nb*

BHF is the hyperfine B constant

$gJ=gL=1$, if there is no mixing in of other states. Should be ok. (For Yb it is 1.035, close enough to 1)

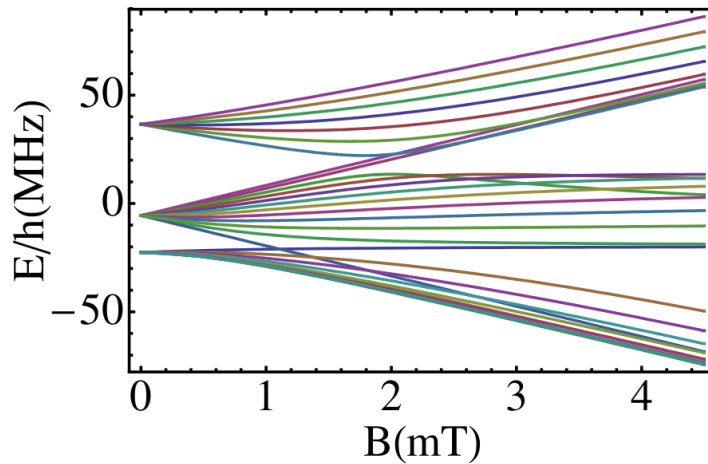
```
test1[B_, mF_] := Sort[Eigenvalues[N[HFSr[B, mF]]]][[1]]
test2[B_, mF_] := Sort[Eigenvalues[N[HFSr[B, mF]]]][[2]]
test3[B_, mF_] := Sort[Eigenvalues[N[HFSr[B, mF]]]][[3]]

ninehalfneg[B_, mF_] := {{HFSr[B, mF][[1, 1]], HFSr[B, mF][[1, 2]]}, {HFSr[B, mF][[2, 1]],
  dipoleandmagnetic[B, mF][[2, 2]] + quadrupole2[[2, 2]] + 1/2 const (i (i + 1) - mF (mF + 1))}}
ninehalfpos[B_, mF_] := {{1/2 const (i (i + 1) - mF (mF - 1)) + dipoleandmagnetic[B, mF][[2, 2]] +
  quadrupole2[[2, 2]], HFSr[B, mF][[2, 3]]}, {HFSr[B, mF][[3, 2]], HFSr[B, mF][[3, 3]]}}
```

The element in the middle, HFSr[[2,2]], has elements from both $J+I-J-I^-$ and $J-I+J+I^-$, only one of them is required for each ninehalfpos and ninehalfneg.

```
halfstretchedpos1[B_] := Sort[Eigenvalues[ninehalfpos[B, 9/2]]][[1]]
halfstretchedpos2[B_] := Sort[Eigenvalues[ninehalfpos[B, 9/2]]][[2]]
halfstretchedneg1[B_] := Sort[Eigenvalues[ninehalfneg[B, -9/2]]][[1]]
halfstretchedneg2[B_] := Sort[Eigenvalues[ninehalfneg[B, -9/2]]][[2]]

Plot[{halfstretchedpos1[B], halfstretchedpos2[B], halfstretchedneg1[B],
  halfstretchedneg2[B], stretched[B], stretched2[B], test1[B, 7/2], test2[B, 7/2],
  test3[B, 7/2], test1[B, 5/2], test2[B, 5/2], test3[B, 5/2], test1[B, 3/2], test2[B, 3/2],
  test3[B, 3/2], test1[B, 1/2], test2[B, 1/2], test3[B, 1/2], test1[B, -1/2], test2[B, -1/2],
  test3[B, -1/2], test1[B, -3/2], test2[B, -3/2], test3[B, -3/2], test1[B, -5/2], test2[B, -5/2],
  test3[B, -5/2], test1[B, -7/2], test2[B, -7/2], test3[B, -7/2]}, {B, 0, 4.5}], Axes → False,
Frame → True, FrameStyle → Thickness[0.005], PlotStyle → Thickness[0.005],
FrameLabel → {"B(mT)", "E/h(MHz)", BaseStyle → {FontSize → 25}]
```



```

Plot[{test2[B, 7/2], test2[B, 5/2], test2[B, 3/2], test2[B, 1/2], test2[B, -1/2], test2[B, -3/2],
      test2[B, -5/2], test2[B, -7/2], halfstretchedpos1[B], halfstretchedneg2[B]}, {B, 0, 80},
  Axes → False, Frame → True, FrameStyle → Thickness[0.004`], FrameLabel → {"B (mT)", "E/h (MHz)"},
  PlotStyle → {{Hue[0.1`], Thickness[0.004`]}, {Hue[0.2`], Thickness[0.004`]},
               {Hue[0.3`], Thickness[0.004`]}, {Hue[0.4`], Thickness[0.004`]},
               {Hue[0.5`], Thickness[0.004`]}, {Hue[0.6`], Thickness[0.004`]},
               {Hue[0.7`], Thickness[0.004`]}, {Hue[0.8`], Thickness[0.004`]},
               {Hue[0.9`], Thickness[0.004`]}, {Hue[1], Thickness[0.004`]}}, PlotRange → {-25, 16},
  BaseStyle → {FontSize → 15, FontFamily → Times}, FrameStyle → Thickness[0.005`]

```

Calculation of the spin flip probability

```

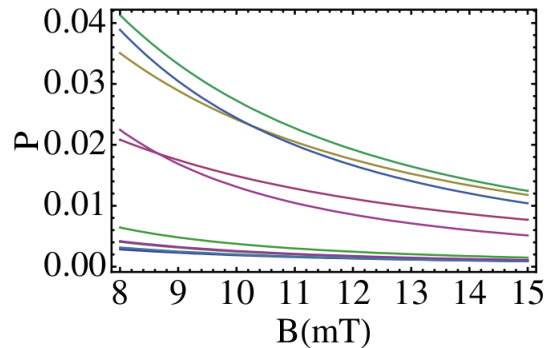
Fidelity[B_, mF_] := Sort[Sort[Eigenvalues[HFSr[B, mF]]][[2]]][[3]]2
Fidelityninehalfpos[B_] := Sort[Sort[Eigenvalues[ninehalfpos[B, 9/2]]][[1]]][[2]]2
Fidelityninehalfneg[B_] := Sort[Sort[Eigenvalues[ninehalfneg[B, -9/2]]][[2]]][[2]]2

Errorprobability[B_, mF_] := 1 - Sort[Sort[Eigenvalues[HFSr[B, mF]]][[2]]][[3]]2

Errorprobabilityninehalfpos[B_] :=
  1 - Sort[Sort[Eigenvalues[ninehalfpos[B, 9/2]]][[1]]][[2]]2
Errorprobabilityninehalfneg[B_] :=
  1 - Sort[Sort[Eigenvalues[ninehalfneg[B, -9/2]]][[2]]][[2]]2

Plot[{Errorprobabilityninehalfpos[B], Errorprobability[B, -7/2],
      Errorprobability[B, -5/2], Errorprobability[B, -3/2], Errorprobability[B, -1/2],
      Errorprobability[B, 1], Errorprobability[B, 3], Errorprobability[B, 5/2],
      Errorprobability[B, 7/2], Errorprobabilityninehalfneg[B]},
  {B, 8, 15}, FrameLabel → {"B (mT)", "P"}, BaseStyle → {FontSize → 20},
  FrameStyle → Thickness[0.005`], PlotStyle → Thickness[0.005`]

```



4 | *quadrupolegraph_thesis.nb*

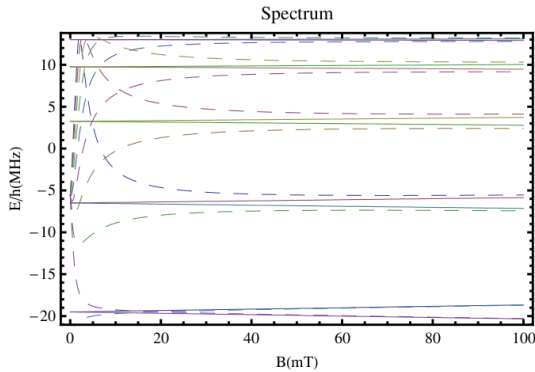
■ For comparison: errorprobability with perturbation theory

```
(*Epert[B_,mF_] := B(-mF gI μN) + const (i (1+i) - mF2) -  $\frac{1}{3}$  const i (1+i) J (1+J);*)
Epert[B_, mF_] := HFSr[B, mF][[2, 2]]
Epertninehalfpos[B_] :=
  1/2 const (i (i + 1) - 9/2 (9/2 - 1)) + dipoleandmagnetic[B, 9/2][[2, 2]] + quadrupole2[[2, 2]]
Epertninehalfneg[B_] := dipoleandmagnetic[B, -9/2][[2, 2]] +
  quadrupole2[[2, 2]] + 1/2 const (i (i + 1) + 9/2 (-9/2 + 1))

T1 = Plot[
  {Epertninehalfpos[B], Epert[B,  $\frac{7}{2}$ ], Epert[B,  $\frac{5}{2}$ ], Epert[B,  $\frac{3}{2}$ ], Epert[B,  $\frac{1}{2}$ ], Epert[B,  $-\frac{1}{2}$ ],
  Epert[B,  $-\frac{3}{2}$ ], Epert[B,  $-\frac{5}{2}$ ], Epert[B,  $-\frac{7}{2}$ ], Epertninehalfneg[B]}, {B, 0, 100}];

T2 = Plot[{test2[B,  $\frac{7}{2}$ ], test2[B,  $\frac{5}{2}$ ], test2[B,  $\frac{3}{2}$ ], test2[B,  $\frac{1}{2}$ ], test2[B,  $-\frac{1}{2}$ ], test2[B,  $-\frac{3}{2}$ ],
  test2[B,  $-\frac{5}{2}$ ], test2[B,  $-\frac{7}{2}$ ], halfstretchedpos1[B], halfstretchedneg2[B]},
  {B, 0, 100}, Axes → False, Frame → True, FrameStyle → Thickness[0.004],
  FrameLabel → {"B (mT)", "E/h (MHz)"}, PlotStyle → Dashing[{0.03}]];

Show[T1, T2, PlotLabel → "Spectrum", FrameLabel → {"B (mT)", "E/h (MHz)"}]
```



Calculation of the transfer of the coherences including γ and δ

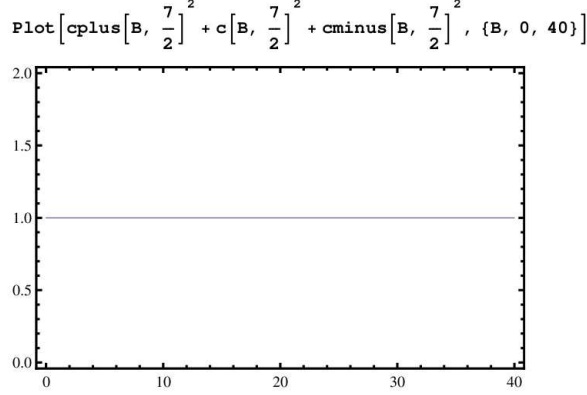
```
r = 32;

cplus[B_, mF_] := Sort[Eigensystem[N[HFSr[B, mF]]]][[2]][[3]][[1]];
c[B_, mF_] := Sort[Eigensystem[N[HFSr[B, mF]]]][[2]][[3]][[2]];
cminus[B_, mF_] := Sort[Eigensystem[N[HFSr[B, mF]]]][[2]][[3]][[3]];

cplusninehalfneg[B_] := Eigenvectors[N[ninehalfneg[B, -9/2]]][[2]][[1]];
cninehalfneg[B_] := Eigenvectors[N[ninehalfneg[B, -9/2]]][[2]][[2]];

The square of cplus ninehalfneg is the overlapp between the states  $|F=9/2, mF=-9/2\rangle$  and  $|mI=-7/2, mJ=-1\rangle$  (of course the state  $F=9/2$  is only a good quantum number for zero magnetic field, its only used as a label for the state here)

cminusninehalfpos[B_] := Sort[Eigenvectors[N[ninehalfpos[B, 9/2]]]][[1]][[1]];
cninehalfpos[B_] := Sort[Eigenvectors[N[ninehalfpos[B, 9/2]]]][[1]][[2]];
```



Ok, *Mathematica* does in fact normalize these vectors.

```

cninehalfpos[3]
0.992545

Δe[B_, mF_] := test2[B, mF] - test2[B, -mF];
Δg[B_, mF_] := -2 mF μN B gI;
Δeninehalf[B_] := halfstretchedpos1[B] - halfstretchedneg2[B];

δ[B_, mF_] := Δg[B, mF] - Δe[B, mF];
δninehalf[B_] := Δg[B, 9/2] - Δeninehalf[B]

γup[B_, mF_] := Γ (cplus[B, mF]^2 + cminus[B, mF]^2);
γdown[B_, mF_] := Γ (cplus[B, -mF]^2 + cminus[B, -mF]^2);
γupninehalf[B_] := Γ Abs[cplusninehalfneg[B]]^2;
γdownninehalf[B_] := Γ Abs[cminusninehalfpos[B]]^2

(*transfer[B_, mF_] := 
$$\frac{\Gamma^2 (c[B, mF]^2 + c[B, -mF]^2)^2 / 4}{(\Gamma (c[B, mF]^2 + c[B, -mF]^2) / 2 + \gamma_{up}[B, mF] / 2 + \gamma_{down}[B, mF] / 2)^2 + \delta[B, mF]^2}$$
 *)

(*transferninehalf[B_] := 
$$\frac{\Gamma^2 (cninehalfpos[B]^2 + cninehalfneg[B]^2)^2 / 4}{(\Gamma (cninehalfpos[B]^2 + cninehalfneg[B]^2) / 2 + \gamma_{upninehalf}[B] / 2 + \gamma_{downninehalf}[B] / 2)^2 + \delta_{ninehalf}[B]^2}$$
 *)

transfer[B_, mF_] := 
$$\frac{\Gamma^2 c[B, mF]^2 c[B, -mF]^2}{\Gamma^2 + \delta[B, mF]^2}$$


transferninehalf[B_] := 
$$\frac{\Gamma^2 cninehalfpos[B]^2 cninehalfneg[B]^2}{\Gamma^2 + \delta_{ninehalf}[B]^2}$$


```

■ Some tests

The Clebsch Gordan coefficients for the states have to be the same as the c 's for $B=0$.

```

cninehalfneg[0]^2
0.181818

```

6 | *quadrupolegraph_thesis.nb*

```
N[ClebschGordan[{9/2, -9/2}, {1, 0}, {11/2, -9/2}]2]
```

0.181818

```
cninehalfpos[0]2
```

0.818182

```
N[ClebschGordan[{9/2, 9/2}, {1, 0}, {9/2, 9/2}]2]
```

0.818182

```
cplusninehalfneg[0]2
```

0.818182

```
N[ClebschGordan[{9/2, -7/2}, {1, -1}, {11/2, -9/2}]2]
```

0.818182

```
cminusninehalfpos[0]2
```

0.181818

```
N[ClebschGordan[{9/2, 7/2}, {1, 1}, {9/2, 9/2}]2]
```

0.181818

Ok, this is fine for mF=9/2, now check some others:

```
N[ClebschGordan[{9/2, 5/2}, {1, 0}, {11/2, 5/2}]2]
```

0.436364

```
c[0, 5/2]2
```

0.436364

```
N[ClebschGordan[{9/2, 3/2}, {1, 1}, {11/2, 5/2}]2]
```

0.509091

```
cminus[0, 5/2]2
```

0.509091

```
N[ClebschGordan[{9/2, 3/2}, {1, -1}, {11/2, 1/2}]2]
```

0.181818

```
cplus[0, 1/2]2
```

0.181818

```
N[ClebschGordan[{9/2, -3/2}, {1, -1}, {11/2, -5/2}]2]
```

0.509091

```
cplus[0, -5/2]2
```

0.509091

A.3 Calculation of the multichannel Hamiltonian

This Mathematica 6 program was used to determine the full multichannel Hamiltonian from the transformations between the different bases described in Chapter 4. Furthermore, it was used to find the adiabatic potentials and the linewidthmatrix from the same chapter. The resulting, block diagonal Hamiltonian was then exported into a fortran Code based on a code by E. Tiesinga and P. Julienne from NIST which used the DVR method described in Section 4.2.2 to yield the multichannel wave functions.

Basis states $|F, R, T, M_T, \rho\rangle$

Initialization

```
Clear["Global`*"];
Off[ClebschGordan::"phy"];
Off[ClebschGordan::"tri"];
SetOptions[Plot, Axes -> False, Frame -> True, BaseStyle -> {FontSize -> 15, FontFamily -> Times}];
```

■ molecular potentials from P. Julienne

```
eu0[σu0_] =  $\frac{2600}{4 \sigma u0^6} * \text{Hartree};$ 
eu1[σu1_] =  $\frac{2600}{4 \sigma u1^6} * \text{Hartree};$ 
Cu0 = -0.1939 * Hartree;
Cu1 = -Cu0 / 2;
μ = 86.96943 amu;

Hartree =  $27.2114 * 2.41799 * 10^{14} / (10^6 * 10^3);$ 
amu =  $1.66054 * 10^{-27};$ 
hbar =  $1.05457 * 10^{-34};$ 
Joule =  $6.24151 * 10^{18} * 2.41799 * 10^{14} / (10^6 * 10^3);$ 
a0 =  $5.29177 * 10^{-11};$ 
```

J in MHz, alternatively I can use P. Juliennes approach,

```
AMU = 1822.8885060;
HARTREE = 219474.630680;
SOL = 29.97924580;
with MHz given as
(HARTREE * SOL * 103 / AMU)
```

$$\text{pot0u}[r_, \sigma u0_] := 4 \text{eu0}[\sigma u0] \left(\left(\frac{\sigma u0}{r} \right)^{12} - \left(\frac{\sigma u0}{r} \right)^6 \right) + \frac{\text{Cu0}}{r^3}$$

$$\text{pot1u}[r_, \sigma u1_] := 4 \text{eu1}[\sigma u1] \left(\left(\frac{\sigma u1}{r} \right)^{12} - \left(\frac{\sigma u1}{r} \right)^6 \right) + \frac{\text{Cu1}}{r^3}$$

$$\text{pot0g}[r_, \sigma u0_] := 4 \text{eu0}[\sigma u0] \left(\left(\frac{\sigma u0}{r} \right)^{12} - \left(\frac{\sigma u0}{r} \right)^6 \right) - \frac{\text{Cu0}}{r^3}$$

$$\text{pot1g}[r_, \sigma u1_] := 4 \text{eu1}[\sigma u1] \left(\left(\frac{\sigma u1}{r} \right)^{12} - \left(\frac{\sigma u1}{r} \right)^6 \right) - \frac{\text{Cu1}}{r^3}$$

```
 $\frac{\text{hbar}^2}{2 \mu 30^2 a0^2} \text{Joule}$ 
0.0230571
```

pot1g is 1_g , while pot1u is 1_u , analogous for the 0 potentials.

2 | YbHamiltonian_thesis.nb

```
potlu[r_] = potlu[r, 6.13 `];
pot0u[r_] = pot0u[r, 6.13 `];
potlg[r_] = potlg[r, 6.13 `];
pot0g[r_] = pot0g[r, 6.13 `];
```

■ Matrices

```
J = 1;
j1 = 1; i1 = 1/2; i2 = 1/2;

μB = 1.4 * 10-3;
gj1 = 1.035;
j1 = 1;
A = 3.9579747;
A = .;

hbar = 1.05457 * 10-34;
Joule = 6.24151 * 1018 * 2.41799 * 1014 / (106 * 103);
a0 = 5.29177 * 10-11;
amu = 1.66054 * 10-27;
μ = 86.96943 amu;

pot[Ω_, i_, p_] :=
  If[(Ω == 1 || Ω == -1) && i == 0 && p == -1, potlu, If[(Ω == 1 || Ω == -1) && i == 1 && p == -1,
    potlg, If[Ω == 0 && i == 0 && p == -1, pot0u, If[Ω == 0 && i == 1 && p == -1, pot0g,
      If[(Ω == 1 || Ω == -1) && i == 0 && p == 1, potlg, If[(Ω == 1 || Ω == -1) && i == 1 && p == 1,
        potlu, If[Ω == 0 && i == 0 && p == 1, pot0g, If[Ω == 0 && i == 1 && p == 1, pot0u]]]]]]]]

X[Ω_, ℓ_] := If[Ω == 0 && ℓ == 0, 1, √2]

yε[f1_, F_, R_, T_, mT_, Ω_, i_, ℓ_, Tp_, mTp_, ε_] := ClebschGordan[{F, ε}, {R, 0}, {T, ε}]
  √((2 i + 1) (2 f1 + 1)) √(2 R + 1) / √(2 T + 1) SixJSymbol[{i1, i2, i}, {j1, F, f1}] (-1)
  ClebschGordan[{J, Ω}, {i, ℓ}, {F, ε}] KroneckerDelta[T, Tp] KroneckerDelta[mT, mTp]

επ[f1_, F_, R_, T_, mT_, f1p_, mf1_, mi2_, Rp_, mR_] :=
  ClebschGordan[{F, (mf1 + mi2)}, {R, mR}, {T, mT}] ClebschGordan[{f1, mf1},
    {i2, mi2}, {F, (mf1 + mi2)}] KroneckerDelta[f1, f1p] KroneckerDelta[R, Rp]
```

s-waves: T=1 (R=0 in the ground state, but in the excited states R=0 or 2)

■ Hamiltonian

p = -1;

ℓ ∈ ≠ |f₁, F, R, T, mT, (p)⟩

```
elist = {{1/2, 1, 0, 1, -1}, {1/2, 1, 2, 1, -1}, {3/2, 1, 0, 1, -1}, {3/2, 1, 2, 1, -1}, {3/2, 2, 2, 1, -1},
  {1/2, 1, 0, 1, 0}, {1/2, 1, 2, 1, 0}, {3/2, 1, 0, 1, 0}, {3/2, 1, 2, 1, 0}, {3/2, 2, 2, 1, 0},
  {1/2, 1, 0, 1, 1}, {1/2, 1, 2, 1, 1}, {3/2, 1, 0, 1, 1}, {3/2, 1, 2, 1, 1}, {3/2, 2, 2, 1, 1}};
```

$\gamma \in \{\Omega, I, \iota, T, mT, \Phi\}$

```

γlist = {};
For[Ωk = -2, Ωk < 1, Ωk++; For[ik = -1, ik < 1, ik++;
  For[mTk = -2, mTk < 1, mTk++; γlist = Append[γlist, {Ωk, ik, 0, 1, mTk, Ωk}]]];
For[Ωk = -2, Ωk < 0, Ωk++; For[mTk = -2, mTk < 1, mTk++;
  γlist = Append[γlist, {Ωk, 1, 1, 1, mTk, Ωk + 1}]]];
For[Ωk = -1, Ωk < 1, Ωk++; For[mTk = -2, mTk < 1, mTk++;
  γlist = Append[γlist, {Ωk, 1, -1, 1, mTk, Ωk - 1}]]];

Length[γlist]

30

εγtable = Table[εγ[{elist[[i]], γlist[[j]]} /. List → Sequence],
  {i, 1, Length[elist]}, {j, 1, Length[γlist]}];

πlist = {}; For[f1k = -1/2, f1k < 3/2, f1k++; For[mf1k = -f1k - 1, mf1k < f1k,
  mf1k++; For[mi2k = -3/2, mi2k < 1/2, mi2k++; For[Rk = -2, Rk < 2, Rk = Rk + 2;
  For[mRk = -Rk - 1, mRk < Rk, mRk++; πlist = Append[πlist, {f1k, mf1k, mi2k, Rk, mRk}]]]]];

επtable = Table[επ[{elist[[ii]], πlist[[jj]]} /. List → Sequence],
  {ii, 1, Length[elist]}, {jj, 1, Length[πlist]}];

B = .;
A = .;
μB = .;
gjl = .;

Ω[γ_] := γlist[[γ]][[1]];
i[γ_] := γlist[[γ]][[2]];
ι[γ_] := γlist[[γ]][[3]];
Φ[γ_] := γlist[[γ]][[4]];
F[ε_] := elist[[ε]][[2]];
T[ε_] := elist[[ε]][[4]];
mT[ε_] := elist[[ε]][[5]];
f1[πt_] := πlist[[πt]][[1]];
mf1[πt_] := πlist[[πt]][[2]];
mi2[πt_] := πlist[[πt]][[3]];
R[πt_] := πlist[[πt]][[4]];
mR[πt_] := πlist[[πt]][[5]];

Htotal = Table[Sum[επtable[[ek]][[πk]] (A/2 (f1[πk] (f1[πk] + 1) - 11/4) +
  B gjl ( (f1[πk] (f1[πk] + 1) - 11/4) / (2 f1[πk] (f1[πk] + 1)) ) μB mf1[πk] + Erot R[πk] (R[πk] + 1) )
  επtable[[ekp]][[πkp]] KroneckerDelta[mR[πk], mR[πkp]] KroneckerDelta[mi2[πk], mi2[πkp]]
  KroneckerDelta[mf1[πk], mf1[πkp]] KroneckerDelta[f1[πk], f1[πkp]]
  KroneckerDelta[F[ek], F[ekp]] KroneckerDelta[R[πk], R[πkp]]
  KroneckerDelta[T[ek], T[ekp]] KroneckerDelta[mT[ek], mT[ekp]],
  {πk, 1, Length[πlist]}, {πkp, 1, Length[πlist]}] +
  Sum[εγtable[[ek]][[γk]] pot[Ω[γk], i[γk], p] εγtable[[ekp]][[γk]]
  KroneckerDelta[T[ek], T[ekp]] KroneckerDelta[mT[ek], mT[ekp]], {γk, 1, Length[γlist]}],
  {ek, 1, Length[elist]}, {ekp, 1, Length[elist]}];

```

Using the fact that the Hamiltonian is blockdiagonal and extracting the blocks

```

H1third = FullSimplify[Htotal[[1 ;; 5, 1 ;; 5]]];
H2third = FullSimplify[Htotal[[6 ;; 10, 6 ;; 10]]];
H3third = FullSimplify[Htotal[[11 ;; 15, 11 ;; 15]]];

```

4 | YbHamiltonian_thesis.nb

```

gjl = .;
μB = .;
A = .;

Export["/Users/iris/Documents/H1third.dat", H1third, "Table"]
/Users/iris/Documents/H1third.dat

Export["/Users/iris/Documents/H2third.dat", H2third, "Table"]
/Users/iris/Documents/H2third.dat

Export["/Users/iris/Documents/H3third.dat", H3third, "Table"]
/Users/iris/Documents/H3third.dat

B = .;

A = 3.9579747;
μB = 1.4 * 10-3;
gjl = 1.035;

sol1third[r_, B_] = Eigenvalues[H1third] /. {pot0u → pot0u[r],
    pot1u → pot1u[r], pot0g → pot0g[r], pot1g → pot1g[r], Erot →  $\frac{\hbar^2}{2 \mu r^2 a_0^2}$  Joule};

sol1third[400 000, 0]
{-3.95797, -3.95797, 1.97899, 1.97899, 1.97899}

```

Asymptotic behavior of the eigenvalues is ok.

```

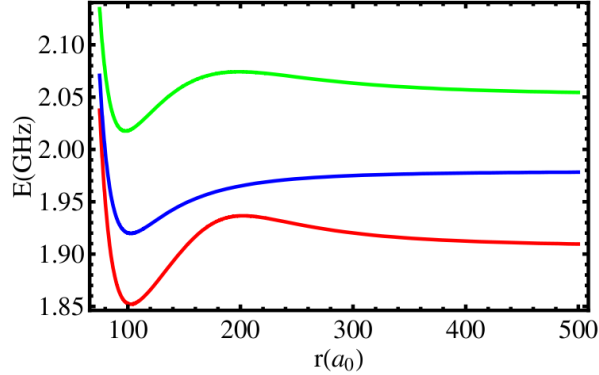
sol2third[r_, B_] = Eigenvalues[H2third] /. {pot0u → pot0u[r],
    pot1u → pot1u[r], pot0g → pot0g[r], pot1g → pot1g[r], Erot →  $\frac{\hbar^2}{2 \mu r^2 a_0^2}$  Joule};

sol3third[r_, B_] = Eigenvalues[H3third] /. {pot0u → pot0u[r],
    pot1u → pot1u[r], pot0g → pot0g[r], pot1g → pot1g[r], Erot →  $\frac{\hbar^2}{2 \mu r^2 a_0^2}$  Joule};

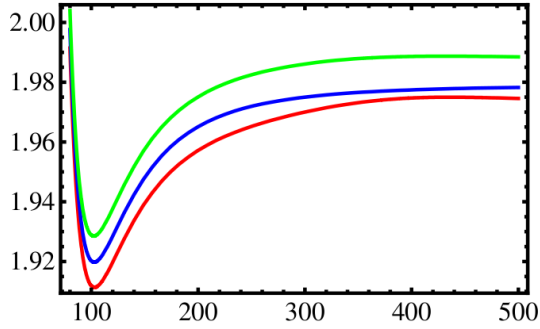
```



```
Plot[{sol1third[r, 1000][[4]], sol2third[r, 1000][[4]], sol3third[r, 1000][[4]]},
  {r, 75, 500}, PlotStyle -> {{Thick, Red}, {Thick, Blue}, {Thick, Green}},
  FrameStyle -> Thick, FrameLabel -> {"r(a0)", "E(GHz)"}]
```



```
Plot[{sol1third[r, 100][[4]], sol2third[r, 100][[4]], sol3third[r, 100][[4]]}, {r, 80, 500},
  PlotStyle -> {{Thick, Red}, {Thick, Blue}, {Thick, Green}}, FrameStyle -> Thick]
```



■ Linewidthmatrix

```
 $\pi$ list = {}; For[f1k = -1/2, f1k < 3/2, f1k++; For[mf1k = -f1k - 1, mf1k < f1k,
  mf1k++; For[mi2k = -3/2, mi2k < 1/2, mi2k++; For[Rk = -2, Rk < 2, Rk = Rk + 2;
  For[mRk = -Rk - 1, mRk < Rk, mRk++;  $\pi$ list = Append[ $\pi$ list, {f1k, mf1k, mi2k, Rk, mRk}]]]]];
```

```
Length[ $\pi$ list]
```

```
72
```

```
e1list = {{1/2, 1, 0, 1, -1}, {1/2, 1, 2, 1, -1}, {3/2, 1, 0, 1, -1}, {3/2, 1, 2, 1, -1}, {3/2, 2, 2, 1, -1},
  {1/2, 1, 0, 1, 0}, {1/2, 1, 2, 1, 0}, {3/2, 1, 0, 1, 0}, {3/2, 1, 2, 1, 0}, {3/2, 2, 2, 1, 0},
  {1/2, 1, 0, 1, 1}, {1/2, 1, 2, 1, 1}, {3/2, 1, 0, 1, 1}, {3/2, 1, 2, 1, 1}, {3/2, 2, 2, 1, 1}}
```

```
 $\epsilon$ table = Table[ $\epsilon$  $\pi$ [{e1list[[ii]],  $\pi$ list[[jj]]} /. List -> Sequence],
  {ii, 1, Length[e1list]}, {jj, 1, Length[ $\pi$ list]}];
```

6 | YbHamiltonian_thesis.nb

■ natural linewidth matrix

Since this is the calculation of the natural linewidth, it is not necessarily true that $R=0$ in the ground state. It is possible for R to be another value since the excited state can decay via a ground state with another R than the original one.

```

milg[γ_] := πglist[[γ]][[1]];
mi2g[γ_] := πglist[[γ]][[2]];
Rg[γ_] := πglist[[γ]][[3]];
mRg[γ_] := πglist[[γ]][[4]];

πglist = {};
For[Rk = -2, Rk < 2, Rk = Rk + 2;
  For[mRk = -Rk - 1, mRk < Rk, mRk++; πglist = Append[πglist, {-1/2, 1/2, Rk, mRk}]]];

πglist

{{{-1/2, 1/2, 0, 0}, {-1/2, 1/2, 2, -2}, {-1/2, 1/2, 2, -1}, {-1/2, 1/2, 2, 0}, {-1/2, 1/2, 2, 1}, {-1/2, 1/2, 2, 2}}}

milg[3]

-1/2

πgdre[Rg_, mRg_, fle_, mfle_, mi2e_, R_, mR_, q_] :=
KroneckerDelta[R, Rg] KroneckerDelta[mR, mRg]
(ClebschGordan[{1/2, -1/2}, {1, q}, {fle, mfle}] KroneckerDelta[mi2e, 1/2] -
ClebschGordan[{1/2, 1/2}, {1, q}, {fle, mfle}] KroneckerDelta[mi2e, -1/2])

(*linewidthelement[fle_, mfle_, mi2e_, R_, mR_, flep_, mflep_, mi2ep_, Rp_, mRp_] :=
yat Sum[πgdre[fle, mfle, mi2e, R, mR, Rp, mRp, q] πgdre[flep, mflep, mi2ep, R, mR, Rp, mRp, qp],
{q, -1, 1}, {qp, -1, 1}]8*)

linewidthelement[fle_, mfle_, mi2e_, R_, mR_, flep_, mflep_, mi2ep_, Rp_, mRp_] :=
yat Sum[πgdre[Rg[πgi], mRg[πgi], fle, mfle, mi2e, R, mR, q] πgdre[Rg[πgi], mRg[πgi], flep,
mflep, mi2ep, Rp, mRp, qp], {q, -1, 1}, {qp, -1, 1}, {πgi, 1, Length[πglist]}]

linewidthelementmatrix =
Table[linewidthelement[{πk}, πlist[[πk]]] /. List → Sequence],
{πk, 1, Length[πlist]}, {πkp, 1, Length[πlist]}];

linewidthmatrix = Table[0, {ii, 1, Length[elist]}, {kk, 1, Length[elist]}];

Monitor[
Do[linewidthmatrix[[ek, ekp]] = Sum[επtable[[ek, πk]] linewidthelementmatrix[[πk, πkp]]
επtable[[ekp, πkp]], {πk, 1, Length[πlist]}, {πkp, 1, Length[πlist]}],
{ek, 1, Length[elist]}, {ekp, 1, Length[elist]}], {ek, ekp}]

linewidthmatrix2 = linewidthmatrix /. yat → atomlw;

Export["/Users/iris/Documents/linewidthmatrix2.txt", linewidthmatrix2, "Table"]

/Users/iris/Documents/linewidthmatrix2.txt

```

p-waves: T=0, 1 or 2 (ground state)

For p-waves: $R=1$, the ground state has parity -1, the nuclear spin I in the groundstate is 1. Therefore, the total angular momentum in the ground state can be 0,1, or 2. Thus, in the excited state, $T=0,1,2$ or 3 and parity is 1.

■ Hamiltonian

```
p = 1;
```

```
 $\pi$  list = {f1, mf1, i2, mi2} |R mR)
 $\epsilon$  list = {f1, F, R, T, MT, p}
 $\gamma$  list = { $\Omega$ , I,  $\mu$ , T, MT,  $\Phi$ }
```

First I construct a list with even and odd R, then I extract the list with only the odd R, which is what I need for p-waves, due to parity $p = p1 p2 (-1)^R$

```
e1list1 = {};
For[Tk = -1, Tk < 3, Tk++; For[MTk = -Tk - 1, MTk < Tk, MTk++;
  For[f1k = -1/2, f1k < 3/2, f1k++; For[Fk = f1k - 3/2, Fk < f1k + 1/2, Fk++; For[
    Rk = Abs[Tk - Fk] - 1, Rk < Tk + Fk, Rk++; e1list1 = Append[e1list1, {f1k, Fk, Rk, Tk, MTk}]]]]]]
```

```
e1list = {};
```

```
Monitor[
  Do[If[OddQ[e1list1[[ii, 3]]], e1list = Append[e1list, e1list1[[ii]]], {ii, Length[e1list1]}, ii]
Length[e1list]
```

89

```
 $\gamma$ list = {};
For[ $\Omega$ k = -2,  $\Omega$ k < 1,  $\Omega$ k++;
  For[ik = -1, ik < 1, ik++; For[ $\iota$ k = -ik - 1,  $\iota$ k < ik,  $\iota$ k++; For[Tk = -1, Tk < 3, Tk++; For[
    MTk = -Tk - 1, MTk < Tk, MTk++;  $\gamma$ list = Append[ $\gamma$ list, { $\Omega$ k, ik,  $\iota$ k, Tk, MTk, ( $\iota$ k +  $\Omega$ k)}]]]]]]];
```

```
Length[ $\gamma$ list]
```

192

```
e $\gamma$ table = Table[ $\gamma \in$ [{e1list[[i]],  $\gamma$ list[[j]]} /. List  $\rightarrow$  Sequence],
  {i, 1, Length[e1list]}, {j, 1, Length[ $\gamma$ list]}];
```

```
Length[e $\gamma$ table]
```

89

```
 $\pi$ list = {}; For[f1k = -1/2, f1k < 3/2, f1k++; For[mf1k = -f1k - 1, mf1k < f1k,
  mf1k++; For[mi2k = -3/2, mi2k < 1/2, mi2k++; For[Rk = -1, Rk < 5, Rk = Rk + 2;
  For[mRk = -Rk - 1, mRk < Rk, mRk++;  $\pi$ list = Append[ $\pi$ list, {f1k, mf1k, mi2k, Rk, mRk}]]]]]]];
```

```
Length[ $\pi$ list]
```

252

```
e $\pi$ table = Table[e $\pi$ [{e1list[[ii]],  $\pi$ list[[jj]]} /. List  $\rightarrow$  Sequence],
  {ii, 1, Length[e1list]}, {jj, 1, Length[ $\pi$ list]}];
```

■ Including magnetic fields and testing

Including magnetic fields. Corrected.

8 | YbHamiltonian_thesis.nb

```

Ω[γ_] := γlist[[γ]][[1]];
i[γ_] := γlist[[γ]][[2]];
ι[γ_] := γlist[[γ]][[3]];
Φ[γ_] := γlist[[γ]][[4]];
F[ε_] := elist[[ε]][[2]];
T[ε_] := elist[[ε]][[4]];
mT[ε_] := elist[[ε]][[5]];
f1[πt_] := πlist[[πt]][[1]];
mf1[πt_] := πlist[[πt]][[2]];
mi2[πt_] := πlist[[πt]][[3]];
R[πt_] := πlist[[πt]][[4]];
mR[πt_] := πlist[[πt]][[5]];

B = .;
A = .;
μB = .;
gjl = .;

Htotal = Table[Sum[επtable[[ek]][[πk]] (A/2 (f1[πk] (f1[πk] + 1) - 11/4) +
  B gjl ( (f1[πk] (f1[πk] + 1) - 11/4) ) μB mf1[πk] + Erot R[πk] (R[πk] + 1) )
  επtable[[ekp]][[πkp]] KroneckerDelta[mR[πk], mR[πkp]] KroneckerDelta[mi2[πk], mi2[πkp]]
  KroneckerDelta[mf1[πk], mf1[πkp]] KroneckerDelta[f1[πk], f1[πkp]]
  KroneckerDelta[F[ek], F[ekp]] KroneckerDelta[R[πk], R[πkp]]
  KroneckerDelta[T[ek], T[ekp]] KroneckerDelta[mT[ek], mT[ekp]],
  {πk, 1, Length[πlist]}, {πkp, 1, Length[πlist]}] +
  Sum[εγtable[[ek]][[γk]] pot[Ω[γk], i[γk], p] εγtable[[ekp]][[γkp]]
  KroneckerDelta[Ω[γk], Ω[γkp]] KroneckerDelta[i[γk], i[γkp]]
  KroneckerDelta[ι[γk], ι[γkp]] KroneckerDelta[Φ[γk], Φ[γkp]]
  KroneckerDelta[T[ek], T[ekp]] KroneckerDelta[mT[ek], mT[ekp]],
  {γk, 1, Length[γlist]}, {γkp, 1, Length[γlist]}],
  {ek, 1, Length[elist]}, {ekp, 1, Length[elist]}];

```

■ Export

```

Htotal2 = Simplify[Htotal];
Htotal2 >> /Users/iris/Documents/H2total2s

```

■ Finding the blocks of the block diagonal matrix

```

gjl = .; μB = .;
Htest = Htotal2;
Htest2 = Htest;
Zeromatrix2 = Table[0, {ii, 1, 2}, {kk, 1, 2}];
Zeromatrix5 = Table[0, {ii, 1, 5}, {kk, 1, 5}];
Zeromatrix6 = Table[0, {ii, 1, 6}, {kk, 1, 6}];
Htest2[[1 ;; 2, 1 ;; 2]] = Zeromatrix2;
Htest2[[3 ;; 7, 3 ;; 7]] = Zeromatrix5;

```

```

Htest2[[8 ;; 12, 8 ;; 12]] = Zeromatrix5;
Htest2[[13 ;; 17, 13 ;; 17]] = Zeromatrix5;
Do[Htest2[[ii ;; ii + 5, ii ;; ii + 5]] = Zeromatrix6, {ii, 18, Length[Htest2] - 5, 6}]

Max[Htest2]
0

Min[Htest2]
0

H2Blocks = Table[0, {ii, 1, 16}]
{0, 0, 0, 0, 0, 0, 0, 0, 0, 0, 0, 0, 0, 0, 0, 0}

H2Blocks[[1]] = FullSimplify[Htest[[1 ;; 2, 1 ;; 2]]] /.
{gj1 * μB → gj, pot0g → V0g, pot0u → V0u, pot1g → V1g, pot1u → V1u};
H2Blocks[[2]] = FullSimplify[Htest[[3 ;; 7, 3 ;; 7]]] /.
{gj1 * μB → gj, pot0g → V0g, pot0u → V0u, pot1g → V1g, pot1u → V1u};
H2Blocks[[3]] = FullSimplify[Htest[[8 ;; 12, 8 ;; 12]]] /.
{gj1 * μB → gj, pot0g → V0g, pot0u → V0u, pot1g → V1g, pot1u → V1u};
H2Blocks[[4]] = FullSimplify[Htest[[13 ;; 17, 13 ;; 17]]] /.
{gj1 * μB → gj, pot0g → V0g, pot0u → V0u, pot1g → V1g, pot1u → V1u};
Do[ii = (kk - 5) * 6 + 18; H2Blocks[[kk]] = FullSimplify[Htest[[ii ;; ii + 5, ii ;; ii + 5]]] /.
{gj1 * μB → gj, pot0g → V0g, pot0u → V0u, pot1g → V1g, pot1u → V1u}, {kk, 5, 16}]

H2Blocks >> /Users/iris/Documents/H2Blocks

```

These blocks can now be inserted into the NIST-Code

■ Shape of the potentials

```

A = 3.9579747;
μB = 1.4 * 10-3;
gj1 = 1.035;

```

All the potentials have to asymptote to either A/2 or -A, depending on whether they correspond to the excited 3P1 state with f1=1/2 or f1=3/2.

```

solblocks = .;

solblocks = Table[0, {i, 1, 16}];

Monitor[Do[solblocks[[ii]] =
Eigenvalues[H2Blocks[[ii]] /. {V0u → pot0u[40 000], V1u → pot1u[40 000], V0g → pot0g[40 000],
V1g → pot1g[40 000], Erot ->  $\frac{\hbar^2}{2 \mu 40 000^2 a_0^2}$  Joule, gj -> gj1 * μB, B → 0}], {ii, 1, 16}], ii];

solblocks[[1]]
{-3.95797, 1.97899}

```

10 | *YbHamiltonian_thesis.nb*

```
solblocks[[2]]  
{-3.95797, -3.95797, 1.97899, 1.97899, 1.97899}  
solblocks[[3]]  
{-3.95797, -3.95797, 1.97899, 1.97899, 1.97899}  
solblocks[[4]]  
{-3.95797, -3.95797, 1.97899, 1.97899, 1.97899}  
solblocks[[5]]  
{-3.95797, -3.95797, 1.97899, 1.97899, 1.97899, 1.97899}  
solblocks[[6]]  
{-3.95797, -3.95797, 1.97899, 1.97899, 1.97899, 1.97899}  
solblocks[[7]]  
{-3.95797, -3.95797, 1.97899, 1.97899, 1.97899, 1.97899}  
solblocks[[8]]  
{-3.95797, -3.95797, 1.97899, 1.97899, 1.97899, 1.97899}  
solblocks[[9]]  
{-3.95797, -3.95797, 1.97899, 1.97899, 1.97899, 1.97899}  
solblocks[[10]]  
{-3.95797, -3.95797, 1.97899, 1.97899, 1.97899, 1.97899}  
solblocks[[11]]  
{-3.95797, -3.95797, 1.97899, 1.97899, 1.97899, 1.97899}  
solblocks[[12]]  
{-3.95797, -3.95797, 1.97899, 1.97899, 1.97899, 1.97899}  
solblocks[[13]]  
{-3.95797, -3.95797, 1.97899, 1.97899, 1.97899, 1.97899}  
solblocks[[14]]  
{-3.95797, -3.95797, 1.97899, 1.97899, 1.97899, 1.97899}  
solblocks[[15]]  
{-3.95797, -3.95797, 1.97899, 1.97899, 1.97899, 1.97899}  
solblocks[[16]]  
{-3.95797, -3.95797, 1.97899, 1.97899, 1.97899, 1.97899}
```

Ok, that is fine. Now some plots:

```

solblock1[r_] = Eigenvalues[H2Blocks[[1]]] /. {V0u -> pot0u[r], V1u -> pot1u[r],
  V0g -> pot0g[r], V1g -> pot1g[r], Erot ->  $\frac{\hbar^2}{2 \mu r^2 a^2}$  Joule, gj -> gj1 *  $\mu B$ };

P1 = Plot[solblock1[r], {r, 30, 250}];

A / 2
1.97899

solblock2[r_, B_] = Eigenvalues[H2Blocks[[2]]] /. {V0u -> pot0u[r], V1u -> pot1u[r],
  V0g -> pot0g[r], V1g -> pot1g[r], Erot ->  $\frac{\hbar^2}{2 \mu r^2 a^2}$  Joule, gj -> gj1 *  $\mu B$ };

P2 = Plot[solblock2[r, 0], {r, 30, 250}, PlotStyle -> Green];

solblock5[r_, B_] = Eigenvalues[H2Blocks[[5]]] /. {V0u -> pot0u[r], V1u -> pot1u[r],
  V0g -> pot0g[r], V1g -> pot1g[r], Erot ->  $\frac{\hbar^2}{2 \mu r^2 a^2}$  Joule, gj -> gj1 *  $\mu B$ };

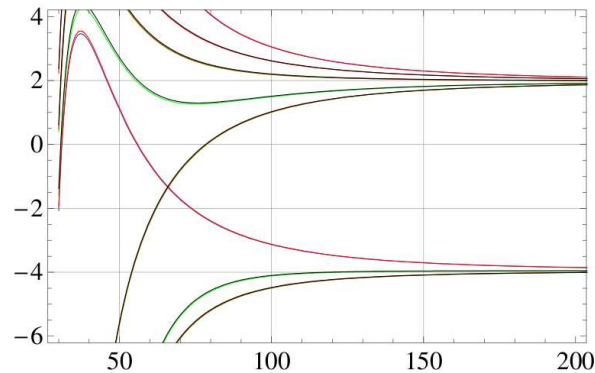
P5 = Plot[solblock5[r, 0], {r, 30, 250}, PlotStyle -> Red];
Plot[solblock5[r, 0], {r, 65, 67}, PlotRange -> {-1, -1.7}]

solblock10[r_, B_] = Eigenvalues[H2Blocks[[10]]] /. {V0u -> pot0u[r], V1u -> pot1u[r],
  V0g -> pot0g[r], V1g -> pot1g[r], Erot ->  $\frac{\hbar^2}{2 \mu r^2 a^2}$  Joule, gj -> gj1 *  $\mu B$ };

P10 = Plot[solblock10[r, 0], {r, 30, 250}, PlotStyle -> Black];

Show[P1, P2, P5, P10, PlotRange -> {{30, 200}, {4, -6}}, GridLines -> Automatic]

```



■ Linewidthmatrix

p = 1;

π list = {f1, mf1, i2, mi2} | R mR)

ϵ list = {f1, FR, T, MT, p}

12 | YbHamiltonian_thesis.nb

```

γ list = {Ω, I, T, MT, Φ }

elist1 = {};
For[Tk = -1, Tk < 3, Tk++; For[MTk = -Tk - 1, MTk < Tk, MTk++;
  For[f1k = -1/2, f1k < 3/2, f1k++; For[Fk = f1k - 3/2, Fk < f1k + 1/2, Fk++; For[
    Rk = Abs[Tk - Fk] - 1, Rk < Tk + Fk, Rk++; elist1 = Append[elist1, {f1k, Fk, Rk, Tk, MTk}]]]]]]

elist = {};

Monitor[
  Do[If[OddQ[elist1[[ii, 3]]], elist = Append[elist, elist1[[ii]]], {ii, Length[elist1]}], ii]
Length[elist]

89

πlist = {}; For[f1k = -1/2, f1k < 3/2, f1k++; For[mf1k = -f1k - 1, mf1k < f1k,
  mf1k++; For[mi2k = -3/2, mi2k < 1/2, mi2k++; For[Rk = -1, Rk < 5, Rk = Rk + 2;
  For[mRk = -Rk - 1, mRk < Rk, mRk++; πlist = Append[πlist, {f1k, mf1k, mi2k, Rk, mRk}]]]]]]

Length[πlist]

252

επtable = Table[επ[{elist[[ii]], πlist[[jj]]} /. List → Sequence],
  {ii, 1, Length[elist]}, {jj, 1, Length[πlist]};

Dimensions[επtable]

{89, 252}

πglist = {}; For[Rk = -1, Rk < 3, Rk = Rk + 2; For[mRk = -Rk - 1, mRk < Rk, mRk++;
  πglist = Join[πglist, {{-1/2, 1/2, Rk, mRk}, {1/2, 1/2, Rk, mRk}, {-1/2, -1/2, Rk, mRk}}]]]

```

■ actual calculation

```

milg[πk_] := πglist[[πk]][[1]];
mi2g[πk_] := πglist[[πk]][[2]];
Rg[πk_] := πglist[[πk]][[3]];
mRg[πk_] := πglist[[πk]][[4]];

πgdre[milg_, mi2g_, Rg_, mRg_, fle_, mfle_, mi2e_, R_, mR_, q_] :=
  KroneckerDelta[milg, -1/2] KroneckerDelta[mi2g, 1/2] KroneckerDelta[R, Rg] KroneckerDelta[mR,
  mRg] (ClebschGordan[{1/2, -1/2}, {1, q}, {fle, mfle}] KroneckerDelta[mi2e, 1/2] -
  ClebschGordan[{1/2, 1/2}, {1, q}, {fle, mfle}] KroneckerDelta[mi2e, -1/2]) +
  KroneckerDelta[milg, mi2g] KroneckerDelta[R, Rg] KroneckerDelta[mR, mRg]
  √2 ClebschGordan[{1/2, milg}, {1, q}, {fle, mfle}]

```

Since this is the calculation of the natural linewidth, it is not necessarily true that $R=1$ in the ground state. It is possible for R to be 1 or 3 since the excited state can decay via a ground state with one of these values.

```

linewidthelement[fle_, mfle_, mi2e_, R_, mR_, flep_, mflep_, mi2ep_, Rp_, mRp_] :=
  γat Sum[πgdre[milg[πgi], mi2g[πgi], Rg[πgi], mRg[πgi], fle, mfle, mi2e, R, mR, q]
  πgdre[milg[πgi], mi2g[πgi], Rg[πgi], mRg[πgi], flep, mflep, mi2ep, Rp, mRp, qp],
  {q, -1, 1}, {qp, -1, 1}, {πgi, 1, Length[πglist]}}

linewidthelement[{πlist[[5]], πlist[[5]]} /. List → Sequence]

8 γat
3

Monitor[linewidthelementmatrix =
  Table[linewidthelement[{πlist[[πk]], πlist[[πkp]]} /. List → Sequence],
  {πk, 1, Length[πlist]}, {πkp, 1, Length[πlist]}, {πk, πkp}]

```



```

Dimensions[linewidthelementmatrix]
{252, 252}

linewidthelementmatrix = linewidthelementmatrix /. γat → lwat;

linewidthmatrix = Table[0, {ii, 1, Length[elist]}, {kk, 1, Length[elist]};

Monitor[
  Do[linewidthmatrix[[ek, ekp]] = Sum[επtable[[ek, πk]] linewidthelementmatrix[[πk, πkp]]
    επtable[[ekp, πkp]], {πk, 1, Length[πlist]}, {πkp, 1, Length[πlist]}],
    {ek, 1, Length[elist]}, {ekp, 1, Length[elist]}], {ek, ekp}]
Export["/Users/iris/Documents/p-wavelinewidth.dat", linewidthmatrix, "Table"]

/Users/iris/Documents/p-wavelinewidth.dat

linewidthmatrix >> /Users/iris/Documents/p-wavelinewidthmatrix

```

This can now be imported again via linewidthmatrix = << /Users/iris/Documents/p-wavelinewidthmatrix

```

Dimensions[linewidthmatrix]
{89, 89}

linewidthmatrix2 = Table[0, {ii, 1, 89}, {jj, 1, 89}];

Monitor[Do[linewidthmatrix2[[ii, jj]] = Simplify[linewidthmatrix[[ii, jj]]],
  {ii, 1, 89}, {jj, 1, 89}], {ii, jj}]

Export["/Users/iris/Documents/p-wavelinewidth_simplified.txt", linewidthmatrix2, "Table"]

/Users/iris/Documents/p-wavelinewidth_simplified.txt

```

A.4 Determination of the optically induced scattering length

This program first determines the Condon factors and linewidths from the multi-channel wave functions calculated with fortran and the uses these to calculate the real and imaginary parts of the scattering length optically induced via the Feshbach resonance.

Initialization

```

Clear["Global`*"];

Off[ClebschGordan::"phy"]
Off[ClebschGordan::"tri"]

SetOptions[Plot, Axes → False, Frame → True,
  BaseStyle → {FontSize → 15, FontFamily → Times}, PlotStyle → Thick, FrameStyle → Thick];

e = 2 μK;

ν0 = (2 l + 1) / 4;

C6 = 1931.7 * Hartree * a06;
C8 = 1.93 * 105 * Hartree;
μ = 85.468163 amu;
σg = 9.0109362 a0;

(*atomic units*)
Hartree = 1;
amu = 1822.8885060;
(*sol = 29.97924580; *)
μK = 3.16682930 * 10-12 Hartree;
hbar = 1;
a0 = 1;

```

Ground state wave functions

This follows Bo Gao's formula for r^6 potentials.

s- waves

■ Initialization

```

l = 0;
e = 2 μK;

ν0 = (2 l + 1) / 4;

β6 = (2 μ C6 / hbar2)1/4 / a0;

Δ =  $\frac{1}{16} \frac{2 \mu \beta 6^2 e}{\text{hbar}^2}$ ;

x = Δ2;

```

2 | Condonfactor_thesis.nb

■ Definitions of required functions

```

Qbar[v_, v0_, x_] := Module[{fpmin, maxIt, vj, b},
  maxIt = 105;
  fpmin = 10-200;
  eps = $MachineEpsilon;
  vj = v + 1;
  b = vj (vj2 - v02);
  If[Abs[b] < fpmin, b = fpmin];
  d = 1/b;
  c = 1/fpmin;
  qb = 1/b;
  Do[
    vj = v + j;
    b = vj (vj2 - v02);
    d = b - x d;
    If[Abs[d] < fpmin, d = fpmin];
    d = 1/d;
    c = b - x/c;
    If[Abs[c] < fpmin, c = fpmin];
    qb = qb * c d;
    nIter = j;
    If[Abs[c d - 1] < eps, Break[], {j, 2, maxIt}];
  qb]

QbarP[v_, v0_, x_] := Module[{j, vj, Iter, qbarP},
  Qbar[v, v0, x];
  Iter = nIter;
  qbarP = 0;
  Do[
    vj = v + j;
    Qbar[vj - 1, v0, x];
    qbarP = -qb2 (3 vj2 - v02 - x qbarP),
    {j, Iter + 1, 1, -1}];
  qbarP]

Λ[v_, v0_, x_] := Module[{fpmin},
  fpmin = 10-200;
  If[Abs[v] < fpmin, lambda = N[-v02 - 2 x QbarP[0, v0, x]],
    lambda = N[(v2 - v02) - (x/v) * (Qbar[v, v0, x] - Qbar[-v, v0, x])];
  lambda]

```

■ Finding the critical energy, at which ν becomes complex

```
FindDeltac[v0_] := x /. FindRoot[Λ[0, v0, x], {x, -5, 5}, Evaluated → False]
```

■ Finding ν

```

Findnu[v0_, x_, l_] := Module[{eps, n1, xc},
  eps = 10-10;
  xc = FindDeltac[v0];
  If[OddQ[l], n1 = (l - 1) / 2 + 1, n1 = l / 2];
  If[x ≤ xc,
    If[OddQ[l], ν = ν /. FindRoot[Λ[ν, v0, x], {ν, n1 + eps, n1 + 0.25}, Evaluated → False],
      ν = ν /. FindRoot[Λ[ν, v0, x], {ν, n1 - 0.375, n1 - eps}, Evaluated → False],
      ν = ν /. FindRoot[Λ[ν, v0, x], {ν, n1 + 0.00001 * I, n1 + 100 I}, Evaluated → False];
  ν]

Q[n_] := Qbar[n, v0, x] (n + 1) ((n + 1)2 - v02)
cj[j_, n_] := Product[Q[k], {k, n, n + j - 1}]

b[j_] := If[j ≥ 0, N[(−Δ)j  $\frac{\text{Gamma}[\nu] \text{Gamma}[\nu - \nu0 + 1] \text{Gamma}[\nu + \nu0 + 1]}{\text{Gamma}[\nu + j] \text{Gamma}[\nu - \nu0 + j + 1] \text{Gamma}[\nu + \nu0 + j + 1]}$  cj[j, ν]],
  N[(−Δ)-j  $\frac{\text{Gamma}[\nu + j + 1] \text{Gamma}[\nu - \nu0 + j] \text{Gamma}[\nu + \nu0 + j]}{\text{Gamma}[\nu + 1] \text{Gamma}[\nu - \nu0] \text{Gamma}[\nu + \nu0]}$  cj[-j, -ν]]];

xc = FindDeltac[v0]
0.00932078

x
9.15783 × 10-6

ν = Findnu[v0, x, l]
-0.249844

X = Sum[(-1)m b[2 m + 1], {m, -40, 40}];
Y = Sum[(-1)m b[2 m], {m, -40, 40}];

Sum[(-1)m b[2 m + 1], {m, -50, 50}] - X
Sum[(-1)m b[2 m], {m, -50, 50}] - Y
0.
0.

α = Cos[π (ν - ν0) / 2] X - Sin[π (ν - ν0) / 2] Y;
β = Sin[π (ν - ν0) / 2] X + Cos[π (ν - ν0) / 2] Y;

fbar[r_] = Sum[b[m] √r BesselJ[ν + m, (r / β6)-2 / 2], {m, -80, 80}];
gbar[r_] = Sum[b[m] √r BesselY[ν + m, (r / β6)-2 / 2], {m, -80, 80}];

k :=  $\frac{\sqrt{2 \mu e}}{\hbar}$  * a0;

cj[40 000, -ν] - cj[20 000, -ν]
-7.42073 × 10-13

Ce[ν_] := cj[30 000, ν]

```

4 | Condonfactor_thesis.nb

```

G[v_] := Abs[Δ]^-v  $\frac{\text{Gamma}[1 + \nu 0 + \nu] \text{Gamma}[1 - \nu 0 + \nu]}{\text{Gamma}[1 - \nu]}$  Ce[v]

Zff =
  ((X^2 + Y^2) Sin[π ν])^-1 ((-1) (α Sin[π ν] - β Cos[π ν]) G[-ν] Sin[π ν - π / 4] + β G[ν] Cos[π ν - π / 4]);
Zfg = ((X^2 + Y^2) Sin[π ν])^-1
  ((-1) (α Sin[π ν] - β Cos[π ν]) G[-ν] Cos[π ν - π / 4] + β G[ν] Sin[π ν - π / 4]);
Zgf = ((X^2 + Y^2) Sin[π ν])^-1 ((-1) (β Sin[π ν] + α Cos[π ν]) G[-ν] Sin[π ν - π / 4] -
  α G[ν] Cos[π ν - π / 4]);
Zgg = ((X^2 + Y^2) Sin[π ν])^-1 ((-1) (β Sin[π ν] + α Cos[π ν]) G[-ν] Cos[π ν - π / 4] -
  α G[ν] Sin[π ν - π / 4]);

```

■ Finally, the actual functions!

```

f[r_] = (α^2 + β^2)^-1 (α fbar[r] - β gbar[r]);
g[r_] = (α^2 + β^2)^-1 (β fbar[r] + α gbar[r]);

```

■ Determination of the linear superposition from the scattering length

For s-waves.

```

abg = -0.15;

K0 = .;
K0 = K0 /. Solve[-k abg ==  $\frac{K0 Zgg - Zfg}{Zff - K0 Zgf}$ , {K0}][[1]]
-0.966138

f[1000] - K0 g[1000]
90.0642

gaonorm = FindMaximum[f[r] - K0 g[r], {r, 1000}][[1]]
91.3166

```

$$\psi_{\text{gao}}[r_] := \sqrt{\frac{2 \mu}{\pi \hbar^2 k}} (\text{f}[r] - \text{K0 g}[r]) / \text{gaonorm}$$

$\sqrt{\frac{2 \mu}{\pi \hbar^2 k}}$ is the normalization following Ciurylo et al. PRA **71**, 03 070 (R) (2005)

Excited States from the NIST-Code

s- waves

■ Condon factors

■ Wave functions

```

SetOptions[Plot, Axes → False, Frame → True,
  BaseStyle -> {FontSize → 15, FontFamily → Times},
  PlotStyle → Thick, FrameStyle → Thick];

wavefunctions1 = Import[
  "/home/iris/Uni/Mathematicaprograms/PA/wavefunctions1third
  Dr_0.0039 Re_7 Rmin_2.5.dat"];

```

These wave functions were calculated with the Code from Julienne and Tiesinga at NIST.

```

rlist1 = {};
Do[rlist1 = Append[rlist1, wavefunctions1[[ii, 1]]],
  {ii, 9 * (wavefunctions1[[1, 1]] + 1) + 2,
  10 * (wavefunctions1[[1, 1]] + 1)}

#g = Interpolation[Table[{rlist1[[ii]], #gao[rlist1[[ii]]}], {ii, 1, Length[rlist1]}]
InterpolatingFunction[{{2.50082, 3971.64}}, <>]

wavefunctions = Table[
  {}, {ii, 1,
  Floor[Length[wavefunctions1] / wavefunctions1[[1, 1]]]}]
{{}, {}, {}, {}, {}, {}, {},
  {}, {}, {}, {}, {}, {}, {}, {}, {}

Do[Do[wavefunctions[[k]] =
  Append[wavefunctions[[k]], Rest[wavefunctions1[[ii]]]],
  {ii, (k - 1) * (wavefunctions1[[1, 1]] + 1) + 2,
  k * (wavefunctions1[[1, 1]] + 1)},
  {k, 1, Length[wavefunctions]}]

Do[wavefunctions[[k]] = Transpose[wavefunctions[[k]]],
  {k, 1, Length[wavefunctions]}]

Condonlist = Table[0, {ii, 1, Length[wavefunctions]}]
{0, 0, 0, 0, 0, 0, 0, 0, 0, 0, 0, 0, 0, 0, 0, 0}

```

6 | Condonfactor_thesis.nb

```

nistwaves = Table[0, {kk, 1, Length[wavefunctions]}]
{0, 0, 0, 0, 0, 0, 0, 0, 0, 0, 0, 0, 0, 0, 0, 0}

Do[nistwaves[[k]] =
  Table[0, {ii, 1, Length[wavefunctions[[k]]}]];
Do[nistwaves[[k, ii]] = Interpolation[
  Transpose[{rlist1, wavefunctions[[k, ii]]}],
  {ii, 1, Length[wavefunctions[[k]]}],
  {k, 1, Length[wavefunctions]}]

```

■ Calculation of $\langle \psi_e | d_M | \psi_g \rangle$

```

i2 = 1/2;

eπ[f1_, F_, R_, T_, mT_, flp_, mf1_, mi2_, Rp_, mR_] :=
ClebschGordan[{F, (mf1 + mi2)}, {R, mR}, {T, mT}] ClebschGordan[{f1, mf1},
  {i2, mi2}, {F, (mf1 + mi2)}] KroneckerDelta[f1, flp] KroneckerDelta[R, Rp]

elist = {{1/2, 1, 0, 1, -1}, {1/2, 1, 2, 1, -1}, {3/2, 1, 0, 1, -1}, {3/2, 1, 2, 1, -1}, {3/2, 2, 2, 1, -1},
  {1/2, 1, 0, 1, 0}, {1/2, 1, 2, 1, 0}, {3/2, 1, 0, 1, 0}, {3/2, 1, 2, 1, 0}, {3/2, 2, 2, 1, 0},
  {1/2, 1, 0, 1, 1}, {1/2, 1, 2, 1, 1}, {3/2, 1, 0, 1, 1}, {3/2, 1, 2, 1, 1}, {3/2, 2, 2, 1, 1}};

πlist = {}; For[flk = -1/2, flk < 3/2, flk++; For[mflk = -flk - 1, mflk < flk,
  mflk++; For[mi2k = -3/2, mi2k < 1/2, mi2k++; For[Rk = -2, Rk < 2, Rk = Rk + 2;
  For[mRk = -Rk - 1, mRk < Rk, mRk++; πlist = Append[πlist, {flk, mflk, mi2k, Rk, mRk}]]]]];

eπtable = Table[eπ[{elist[[ii]], πlist[[jj]]} /. List -> Sequence],
  {ii, 1, Length[elist]}, {jj, 1, Length[πlist]}];

```

$$\pi g = \left\{ -\frac{1}{2}, \frac{1}{2}, 0, 0 \right\}$$

This is taken into account with the formula for $\pi g d \pi e$

```

πgdπe[fle_, mfle_, mi2e_, R_, mR_, q_] := KroneckerDelta[R, 0] KroneckerDelta[mR, 0]
  (ClebschGordan[{1/2, -1/2}, {1, q}, {fle, mfle}] KroneckerDelta[mi2e, 1/2] -
  ClebschGordan[{1/2, 1/2}, {1, q}, {fle, mfle}] KroneckerDelta[mi2e, -1/2])

dmolllist = FullSimplify[Table[Sum[eπtable[[ii, kk]] πgdπe[{πlist[[kk]], q} /. List -> Sequence],
  {kk, 1, Length[πlist]}, {q, -1, 1}], {ii, 1, Length[elist]}]

{-√(2/3), 0, -2/√3, 0, 0, -√(2/3), 0, -2/√3, 0, 0, -√(2/3), 0, -2/√3, 0, 0}

dmolllist =
FullSimplify[Table[Sum[eπtable[[ii, kk]] πgdπe[{πlist[[kk]], -1} /. List -> Sequence],
  {kk, 1, Length[πlist]}, {ii, 1, Length[elist]}]

{-√(2/3), 0, -2/√3, 0, 0, 0, 0, 0, 0, 0, 0, 0, 0, 0, 0}

```


8 | Condonfactor_thesis.nb

```

zerowaves = . ;

zerotable = Table[{rlist1[[ii]], 0}, {ii, 1, Length[rlist1]};

zerowaves = Interpolation[zerotable]

InterpolatingFunction[{{2.50082, 3971.64}}, <>]

zeroblock = Table[zerowaves, {n, 1, 5}];

Do[nistwavescomplete[[ii]] =
  Join[nistwaves[[ii]], zeroblock, zeroblock],
  {ii, 1, Length[nistwaves]}]

Dimensions[nistwavescomplete]
{17, 15}

```

■ Check of Normalization

```

testnorm1 = 0;

Do[testnorm1 =
  testnorm1 + NIntegrate[nistwavescomplete[[1, ii]][x]^2,
    {x, 10, 100}, WorkingPrecision → 40, PrecisionGoal → 5,
    AccuracyGoal → 5, MaxRecursion → 20] +
  NIntegrate[nistwavescomplete[[1, ii]][x]^2,
    {x, 100, 2500}], {ii, 1, 5}]

testnorm1
0.966576

testnorm = Table[0, {kk, Length[nistwaves]}]
Monitor[Do[testnorm[[kk]] = testnorm[[kk]] +
  NIntegrate[nistwavescomplete[[kk, ii]][x]^2,
    {x, 10, 100}, WorkingPrecision → 40, PrecisionGoal → 5,
    AccuracyGoal → 5, MaxRecursion → 20] + NIntegrate[
  nistwavescomplete[[kk, ii]][x]^2, {x, 100, 2500}],
  {ii, 1, 5}, {kk, 1, 17}], {ii, kk}]
{0, 0, 0, 0, 0, 0, 0, 0, 0, 0, 0, 0, 0, 0, 0, 0, 0}

testnorm
{0.966576, 0.845066, 0.844767, 0.996415, 0.994729, 0.991238, 0.987412, 0.985274, 1.00017,
  0.986199, 0.989625, 1.00016, 0.993744, 0.996686, 0.999895, 0.998765, 0.917064}

linewidthlist = Table[0, {kk, 1, Length[nistwavescomplete]}]
{0, 0, 0, 0, 0, 0, 0, 0, 0, 0, 0, 0, 0, 0, 0, 0, 0}

```

```

Monitor[Do[linewidthlist[[kk]] =
  Sum[NIntegrate[nistwavescomplete[[kk, ii]][r] lwmatrix[[ii,
    i]] nistwavescomplete[[kk, i]][r] / testnorm[[kk]],
    {r, 10, 100}, WorkingPrecision → 40, PrecisionGoal → 5,
    AccuracyGoal → 5, MaxRecursion → 20] +
  NIntegrate[nistwavescomplete[[kk, ii]][r]
    lwmatrix[[ii, i]] nistwavescomplete[[kk, i]][r] /
    testnorm[[kk]], {r, 100, 2500}],
  {ii, 1, Length[nistwavescomplete[[kk]]}],
  {i, 1, Length[nistwavescomplete[[kk]]}], {kk, 1, 15}], kk]

```

```
linewidthlist
```

```
{240.913, 100.751, 160.595, 260.71, 256.353, 251.307, 248.08, 246.255,
  89.0717, 245.006, 243.938, 96.6826, 243.279, 242.91, 101.759, 242.673, 242.482}
```

■ Optical Feshbach resonance

■ units

```

Δ = .;
Joule = 2.293713 × 1017 Hartree;
MHz = 106 / (6.57969 × 1015) Hartree;

m =  $\frac{1}{5.29177 \times 10^{-11}}$ ;
s =  $\frac{10^{17}}{2.418884}$ ;
v0 = 2.18769 × 106;
c = 299792458 / v0;
k =  $\frac{\sqrt{2 \mu e}}{\hbar} * a0$ ;
Isat = 1.3 Joule / (s m2);
Γnat = 0.08907168600514454` MHz;
ΓnatM = 0.08907168600514454`;
Γatom = 0.182 MHz;
Int = 104 Joule / (s m2);

```

■ For all states

```

Condonlist = {8.68888380093431`6, 2.1865647973381523`6,
  194302.96134921542`, 2.023001088200115`7, 3.539804326096886`7,
  7.422571629740183`7, 1.3641708156704983`8, 2.8596097811584646`8,
  6.073860461338486`8, 6.08542640003828`8, 1.4284379456676397`9,
  4.821557451076396`8, 3.5875931600950017`9, 9.263170196574196`9,
  6.032295030715225`9, 1.804050551369232`10, 4.2434644263798654`8};

Γnatlist = {240.91311096041431`, 100.75106230389939`, 160.59526272900635`,
  260.70965929151885`, 256.3526830178111`, 251.30666435584357`,
  248.07955744980563`, 246.25487758843667`, 89.07168600514454`,
  245.0058954081835`, 243.93798318985534`, 96.68256978399587`, 243.27922870116979`,
  242.90980370348677`, 101.75948426853722`, 242.6729664423148`, 242.4818068707824`};

Γnatlist = Γnatlist / 103;

```

10 | *Condonfactor_thesis.nb*

natural linewidth in MHz

```

Γstimlist[int_] := Table[π / 4 hbar Γatom2 Condonlist[[i]] int / Isat, {i, 1, 17}]

loptlist[int_] := Table[ $\frac{\Gamma\text{stimlist}[int][[i]]}{2 k \Gamma\text{natlist}[[i]] \text{ MHz}}$ , {i, 1, 17}]

loptlist[Int]
{390.421, 234.932, 13.0971, 839.979, 1494.76, 3197.27, 5952.61, 12570.5,
 7381.67, 26887.1, 63388.6, 53984.4, 159635., 412804., 641707., 804742., 18944.}

k loptlist[Int]
{0.548476, 0.33004, 0.0183993, 1.18003, 2.09988, 4.49163, 8.36241, 17.6594,
 10.37, 37.7719, 89.0504, 75.8391, 224.26, 579.921, 901.491, 1130.53, 26.6131}

aoptlist[Δ_, Intens_] := loptlist[Intens]  $\frac{\Delta \Gamma\text{natlist}}{\Delta^2 + (\Gamma\text{natlist} + \Gamma\text{stimlist}[Intens] / \text{MHz})^2 / 4}$ 

boptlist[Δ_, Intens_] := 1 / 2 loptlist[Intens]  $\frac{\Gamma\text{natlist}^2}{\Delta^2 + (\Gamma\text{natlist} + \Gamma\text{stimlist}[Intens] / \text{MHz})^2 / 4}$ 

```

■ $\sqrt{\text{SWAP}}$ gate (state at 396.5 MHz detuning → state for paper)

```

intens = 12.71 * 104 Joule / (s m2);

SetOptions[Plot, Axes → False, Frame → True,
  BaseStyle → {FontSize → 20, FontFamily → Times}, PlotStyle → Thick, FrameStyle → Thick];

Plot[{aoptlist[Δ, intens][[4]], boptlist[Δ, intens][[4]]},
  {Δ, -300 Γnatlist[[4]], 300 Γnatlist[[4]]},
  PlotStyle → {Blue, Thick}, {Red, Thick}, FrameLabel → {"Δ(MHz)", ""}]

Fidlist[Δ_] := Exp[-Abs[(π) boptlist[Δ, intens] / aoptlist[Δ, intens]]]

Plot[Fidlist[Δ][[4]], {Δ, -40 Γnatlist[[4]], 40 Γnatlist[[4]]}, FrameLabel → {"Δ(MHz)", "F"}]

TSwaplist[Δ_, int_] := 285 * 10-6 s / 2 * 100 / aoptlist[Δ, int] * 171 / 87

```

References

- [1] M. M. Boyd. *High Precision Spectroscopy of Strontium in an Optical Lattice: Towards a New Standard for Frequency and Time*. PhD thesis, University of Colorado, 2007.
- [2] S. A. Diddams, J. C. Bergquist, S. R. Jefferts, and C. W. Oates. Standards of time and frequency at the outset of the 21st century. *Science*, 306:1318, 2004.
- [3] Steven Chu. Nobel lecture: The manipulation of neutral particles. *Rev. Mod. Phys.*, 70(3):685–706, Jul 1998.
- [4] Claude N. Cohen-Tannoudji. Nobel lecture: Manipulating atoms with photons. *Rev. Mod. Phys.*, 70(3):707–719, Jul 1998.
- [5] William D. Phillips. Nobel lecture: Laser cooling and trapping of neutral atoms. *Rev. Mod. Phys.*, 70(3):721–741, Jul 1998.
- [6] Michael A. Nielsen and Isaac L. Chuang. *Quantum Computation and Quantum Information*. Cambridge University Press, 2000.
- [7] Sergey G. Porsev, Andrei Derevianko, and E. N. Fortson. Possibility of an optical clock using the $6^1s_0 \rightarrow 6^3p_0$ transition in $^{171,173}\text{Yb}$ atoms held in an optical lattice. *Phys. Rev. A*, 69(021403(R)):021403 R, February 2004.
- [8] Martin M. Boyd, Andrew D. Ludlow, Sebastian Blatt, Seth M. Foreman, Tetsuya Ido, Tanya Zelevinsky, and Jun Ye. ^{87}Sr lattice clock with inaccuracy below 10^{-15} . *Phys. Rev. Lett.*, 98(8):083002, 2007.
- [9] Ivan H. Deutsch and Poul S. Jessen. Quantum-state control in optical lattices. *Phys. Rev. A*, 57(3):1972–1986, Mar 1998.
- [10] Gavin K. Brennen, Carlton M. Caves, Poul S. Jessen, and Ivan H. Deutsch. Quantum logic gates in optical lattices. *Phys. Rev. Lett.*, 82(5):1060, February 1999.

- [11] Gavin K. Brennen and Jamie E. Williams. Entanglement dynamics in one-dimensional quantum cellular automata. *Phys. Rev. A*, 68:042311, October 2003.
- [12] T. Calarco, U. Dorner, P. S. Julienne, C. J. Williams, and P. Zoller. Quantum computations with atoms in optical lattices: Marker qubits and molecular interactions. *Phys. Rev. A*, 70(1):012306, Jul 2004.
- [13] David Hayes, Paul S. Julienne, and Ivan H. Deutsch. Quantum logic via the exchange blockade in ultracold collisions. *Phys. Rev. Lett.*, 98(7):070501, 2007.
- [14] J. Sebby-Strabley, M. Anderlini, P. S. Jessen, and J. V. Porto. Lattice of double wells for manipulating pairs of cold atoms. *Phys. Rev. A*, 73(3):033605, 2006.
- [15] Immanuel Bloch, Jean Dalibard, and Wilhelm Zwerger. Many-body physics with ultracold gases. *Rev. Mod. Phys.*, 80(3):885, 2008.
- [16] D. Jaksch, C. Bruder, J. I. Cirac, C. W. Gardiner, and Peter Zoller. Cold bosonic atoms in optical lattices. *Phys. Rev. Lett.*, 81(15):3108, October 1998.
- [17] W. Hofstetter, J. I. Cirac, P. Zoller, E. Demler, and M. D. Lukin. High-temperature superfluidity of fermionic atoms in optical lattices. *Phys. Rev. Lett.*, 89:220407, November 2002.
- [18] D. Jaksch, H.-J. Briegel, J. I. Cirac, C. W. Gardiner, and P. Zoller. Entanglement of atoms via cold controlled collisions. *Phys. Rev. Lett.*, 82(9):1975, March 1999.
- [19] Takeshi Fukuhara, Seiji Sugawa, Masahito Sugimoto, Shintaro Taie, and Yoshiro Takahashi. Mott insulator of ultracold alkaline-earth-metal-like atoms. *Phys. Rev. A*, 79(4):041604, 2009.
- [20] Robert Raussendorf. Quantum cellular automaton for universal quantum computation. *Phys. Rev. A*, 72(2):022301, 2005.
- [21] R. Raussendorf, J. Harrington, and K. Goyal. A fault-tolerant one-way quantum computer. *Annals of Physics*, 321:2242, 2006.
- [22] Andrew J. Daley, Martin M. Boyd, Jun Ye, and Peter Zoller. Quantum computing with alkaline-earth-metal atoms. *Phys. Rev. Lett.*, 101(17):170504, 2008.
- [23] L. M. K. Vandersypen and I. L. Chuang. Nmr techniques for quantum control and computation. *Rev. Mod. Phys.*, 76(4):1037–1069, Jan 2005.
- [24] Martin M. Boyd, Tanya Zelevinsky, Andrew D. Ludlow, Sebastian Blatt, Thomas Zanon-Willette, Seth M. Foreman, and Jun Ye. Nuclear spin effects in optical lattice clocks. *Phys. Rev. A*, 76(2):022510, 2007.

- [25] Z. W. Barber, C. W. Hoyt, C. W. Oates, L. Hollberg, A. V. Taichenachev, and V. I. Yudin. Direct excitation of the forbidden clock transition in neutral ^{174}Yb atoms confined to an optical lattice. *Phys. Rev. Lett.*, 96(8):083002, 2006.
- [26] Robin Santra, Ennio Arimondo, Tetsuya Ido, Chris H. Greene, and Jun Ye. High-accuracy optical clock via three-level coherence in neutral bosonic ^{88}Sr . *Phys. Rev. A*, 95(173002):173002, May 2005.
- [27] René Stock, Andrew Silberfarb, Eric L. Bolda, and Ivan H. Deutsch. Generalized pseudo-potentials for higher partial wave scattering. *Phys. Rev. Lett.*, 94:023202, January 2005.
- [28] René Stock. *Trap-induced resonances in controlled atomic collisions for quantum information processing*. PhD thesis, University of New Mexico, 2005.
- [29] Iris Reichenbach, Andrew Silberfarb, René Stock, and Ivan H. Deutsch. Quasi-hermitian pseudopotential for higher partial wave scattering. *Phys. Rev. A*, 74(4):042724, 2006.
- [30] Iris Reichenbach and Ivan H. Deutsch. Sideband cooling while preserving coherences in the nuclear spin state in group-ii-like atoms. *Phys. Rev. Lett.*, 99(12):123001, 2007.
- [31] John R. Taylor. *Scattering Theory: The Quantum Theory of Nonrelativistic Collisions*. John Wiley & Sons, Inc., New York, 1972.
- [32] Keith Burnett, Paul S. Julienne, Paul D. Lett, Eite Tiesinga, and Carl J. Williams. Quantum encounters of the cold kind. *Nature Insight - Ultracold matter*, 416(6877):225–232, March 2002.
- [33] Enrico Fermi. Sul moto dei neutroni nelle sostanze idrogenate. *La Ricerca Scientifica, Serie II, Anno VII*, II:13–52, 1936.
- [34] Eric L. Bolda, Eite Tiesinga, and P. S. Julienne. Effective-scattering-length model of ultracold atomic collisions and feshbach resonances in tight harmonic traps. *Phys. Rev. A*, 66:013403, July 2002.
- [35] Cheng Chin, Rudolf Grimm, Paul Julienne, and Eite Tiesinga. Feshbach resonances in ultracold gases. 2008.
- [36] Keith Burnett, Paul S. Julienne, Paul D. Lett, Eite Tiesinga, and Carl Williams. Quantum encounters of the cold kind. *Nature Insight - Ultracold matter*, 416(6877):225–232, March 2002.

- [37] René Stock, Ivan H. Deutsch, and Eric L. Bolda. Quantum state control via trap-induced shape resonance in ultracold atomic collisions. *Phys. Rev. Lett.*, 91:183201, October 2003.
- [38] Marco Anderlini, Patricia J. Lee, Benjamin L. Brown, Jennifer Sebby-Strabley, William D. Phillips, and J. V. Porto. Controlled exchange interaction between pairs of neutral atoms in an optical lattice. *Nature*, 448:452–456, 2007.
- [39] Kevin M. Jones, Eite Tiesinga, Paul D. Lett, and Paul S. Julienne. Ultracold photoassociation spectroscopy: Long-range molecules and atomic scattering. *Rev. Mod. Phys.*, 78(2):483, 2006.
- [40] Paul S. Julienne. Notes on photoassociation of yb and sr.
- [41] B. H. Bransden and C. J. Joachain. *Physics of Atoms and Molecules*. Pearson Education Limited, second edition, 2003.
- [42] Richard N. Zare. *Angular Momentum: Understanding Spatial Aspects in Chemistry and Physics*. John Wiley and Sons, 1988.
- [43] D. M. Brink and G. R. Satchler. *Angular Momentum*. Oxford University Press, Oxford, second edition, 1986.
- [44] Reginaldo Napolitano, John Weiner, and Paul S. Julienne. Theory of optical suppression of ultracold-collision rates by polarized light. *Phys. Rev. A*, 55(2):1191–1207, Feb 1997.
- [45] D. A. Varshalovich, A. N. Moskalev, and V. K. Khersonskii. *Quantum Theory of Angular Momentum*. World Scientific Publishing Co., 1988.
- [46] M. D. Barrett, B. DeMarco, T. Schaetz, V. Meyer, D. Leibfried, J. Britton, J. Chiaverini, W. M. Itano, B. Jelenković, J. D. Jost, C. Langer, T. Rosenband, and D. J. Wineland. Sympathetic cooling of 9be^+ and 24mg^+ for quantum logic. *Phys. Rev. A*, 68(4):042302, Oct 2003.
- [47] A. J. Daley, P. O. Fedichev, and P. Zoller. Single-atom cooling by superfluid immersion: A nondestructive method for qubits. *Phys. Rev. A*, 69(4):022306, February 2004.
- [48] F. Diedrich, J. C. Berquist, Wayne M. Itano, D. J. Wineland, F. Diedrich, J. C. Bergquist, Wayne M. Itano, and D. J. Wineland. Laser cooling to the zero-point energy of motion. *Phys. Rev. Lett.*, 62(4):403–406, Jan 1989.
- [49] Masao Takamoto, Feng-Lei Hong, Ryoichi Higashi, and Hidetoshi Katori. An optical lattice clock. *Nature*, 435:321, 2005.

- [50] Andrew D. Ludlow, Martin M. Boyd, Tanya Zelevinsky, Seth M. Foreman, Sebastian Blatt, Mark Notcutt, Tetsuya Ido, and Jun Ye. Systematic study of the ^{87}Sr clock transition in an optical lattice. *Phys. Rev. Lett.*, 96(3):033003, 2006.
- [51] C. W. Hoyt, Z. W. Barber, C. W. Oates, T. M. Fortier, S. A. Diddams, and L. Hollberg. Observation and absolute frequency measurements of the $^1s_0 - ^3p_0$ optical clock transition in ytterbium. *Phys. Rev. Lett.*, 95(083003):083003, August 2005.
- [52] Martin M. Boyd, Tanya Zelevinsky, Andrew D. Ludlow, Seth M. Foreman, Sebastian Blatt, Tetsuya Ido, and Jun Ye. Optical atomic coherence at the 1-second time scale. *Science*, 314(5804):1430–1433, 2006.
- [53] Christopher J. Foot. *Atomic Physics*. Oxford University Press, Oxford, 2004.
- [54] D. J. Wineland and Wayne M. Itano. Laser cooling of atoms. *Phys. Rev. A*, 20(4):1521–1540, Oct 1979.
- [55] D. Leibfried, R. Blatt, C. Monroe, and D. Wineland. Quantum dynamics of single trapped ions. *Rev. Mod. Phys.*, 75(1):281–324, Mar 2003.
- [56] C. Monroe, D. M. Meekhof, B. E. King, S. R. Jefferts, W. M. Itano, D. J. Wineland, and P. Gould. Resolved-sideband raman cooling of a bound atom to the 3d zero-point energy. *Phys. Rev. Lett.*, 75(22):4011–4014, Nov 1995.
- [57] H. Perrin, A. Kuhn, I. Bouchoule, and C. Salomon. Sideband cooling of neutral atoms in a far-detuned optical lattice. *EPL (Europhysics Letters)*, 42(4):395–400, 1998.
- [58] Ivan H. Deutsch. Lecture notes on quantum optics. <http://info.phys.unm.edu/deutschgroup/Classes/Phys566F08/index.htm>.
- [59] Marlan O. Scully and Mohammad S. Zubairy. *Quantum Optics*. Cambridge University Press, 1997.
- [60] U. Sterr, C. Degenhardt, H. Stoehr, Ch. Lisdat, H. Schnatz, J. Helmcke, F. Riehle, G. Wilpers, Ch. Oates, and L. Hollberg. The optical calcium frequency standards of ptb and nist. *Comptes Rendus Physique*, 5(8):845 – 855, 2004. Fundamental metrology.
- [61] E. Anne Curtis, Christopher W. Oates, and Leo Hollberg. Quenched narrow-line second- and third-stage laser cooling of 40 ca. *J. Opt. Soc. Am. B*, 20(5):977–984, 2003.
- [62] Wayne M. Itano, D. J. Heinzen, J. J. Bollinger, and D. J. Wineland. Quantum zeno effect. *Phys. Rev. A*, 41(5):2295–2300, Mar 1990.

- [63] R. W. Berends and L. Maleki. Hyperfine structure and isotope shifts of transitions in neutral and singly ionized ytterbium. *J. Opt. Soc. Am. B*, 9(8):8, March 1992.
- [64] H. Jürgen Kluge and Hatto Sauter. Levelcrossing experiments in the first excited 1p_1 states of the alkaline earths. *Z. Phys.*, 240:295, 1974.
- [65] Anders Brusch, Rodolphe Le Targat, Xavier Baillard, Mathilde Fouché, and Pierre Lemonde. Hyperpolarizability effects in a sr optical lattice clock. *Phys. Rev. Lett.*, 96(10):103003, 2006.
- [66] A. V. Gorshkov, A. M. Rey, A. J. Daley, M. M. Boyd, J. Ye, P. Zoller, and M. D. Lukin. Alkaline-earth-metal atoms as few-qubit quantum registers. *Phys. Rev. Lett.*, 102(11):110503, 2009.
- [67] Herman Feshbach. Unified theory of nuclear reactions. *Annals of Physics*, 5(4):357, 1958.
- [68] U. Fano. Effects of configuration interaction on intensities and phase shifts. *Phys. Rev.*, 124(6):1866–1878, Dec 1961.
- [69] Cindy A. Regal, Christopher Ticknor, John L. Bohn, and Deborah S. Jin. Creation of ultracold molecules from a fermi gas of atoms. *Nature*, 424(6944):47, 2003.
- [70] K.-K. Ni, S. Ospelkaus, M. H. G. de Miranda, A. Pe’er, B. Neyenhuis, J. J. Zirbel, S. Kotochigova, P. S. Julienne, D. S. Jin, and J. Ye. A high phase-space-density gas of polar molecules. *Science*, 322(5899):231–235, 2008.
- [71] D. DeMille. Quantum computation with trapped polar molecules. *Phys. Rev. Lett.*, 88(6):067901, Jan 2002.
- [72] T. Bourdel, L. Khaykovich, J. Cubizolles, J. Zhang, F. Chevy, M. Teichmann, L. Tarruell, S. J. J. M. F. Kokkelmans, and C. Salomon. Experimental study of the bec-bcs crossover region in lithium 6. *Phys. Rev. Lett.*, 93(5):050401, Jul 2004.
- [73] Stefano Giorgini, Lev P. Pitaevskii, and Sandro Stringari. Theory of ultracold atomic fermi gases. *Rev. Mod. Phys.*, 80(4):1215, 2008.
- [74] P. O. Fedichev, Yu. Kagan, G. V. Shlyapnikov, and J. T. M. Walraven. Influence of nearly resonant light on the scattering length in low-temperature atomic gases. *Phys. Rev. Lett.*, 77(14):2913–2916, Sep 1996.
- [75] John L. Bohn and P. S. Julienne. Prospects for influencing scattering lengths with far-off-resonant light. *Phys. Rev. A*, 56(2):1486–1491, Aug 1997.

- [76] F. K. Fatemi, K. M. Jones, and P. D. Lett. Observation of optically induced feshbach resonances in collisions of cold atoms. *Phys. Rev. Lett.*, 85(21):4462–4465, Nov 2000.
- [77] M. Theis, G. Thalhammer, K. Winkler, M. Hellwig, G. Ruff, R. Grimm, and J. Hecker Denschlag. Tuning the scattering length with an optically induced feshbach resonance. *Phys. Rev. Lett.*, 93(12):123001, Sep 2004.
- [78] Gregor Thalhammer, Matthias Theis, Klaus Winkler, Rudolf Grimm, and Johannes Hecker Denschlag. Inducing an optical feshbach resonance via stimulated raman coupling. *Phys. Rev. A*, 71(3):033403, 2005.
- [79] R. Ciuryło, E. Tiesinga, and P. S. Julienne. Optical tuning of the scattering length of cold alkaline-earth-metal atoms. *Phys. Rev. A*, 71(3):030701, Mar 2005.
- [80] K. Enomoto, K. Kasa, M. Kitagawa, and Y. Takahashi. Optical feshbach resonance using the intercombination transition. *Phys. Rev. Lett.*, 101(20):203201, 2008.
- [81] Katsunari Enomoto, Masaaki Kitagawa, Satoshi Tojo, and Yoshiro Takahashi. Hyperfine-structure-induced purely long-range molecules. *Phys. Rev. Lett.*, 100(12):123001, 2008.
- [82] T. Zelevinsky, M. M. Boyd, A. D. Ludlow, T. Ido, J. Ye, R. Ciuryło, P. Naidon, and P. S. Julienne. Narrow line photoassociation in an optical lattice. *Phys. Rev. Lett.*, 96(20):203201, 2006.
- [83] Y. N. Martinez de Escobar, P. G. Mickelson, M. Yan, and T. C. Killian. Tuning the elastic collision cross section with an intercombination-line optical feshbach resonance. unpublished.
- [84] John L. Bohn and P. S. Julienne. Semianalytic theory of laser-assisted resonant cold collisions. *Phys. Rev. A*, 60(1):414–425, Jul 1999.
- [85] Eite Tiesinga, Kevin M. Jones, Paul D. Lett, Udo Volz, Carl J. Williams, and Paul S. Julienne. Measurement and modeling of hyperfine- and rotation-induced state mixing in large weakly bound sodium dimers. *Phys. Rev. A*, 71(5):052703, 2005.
- [86] Bo Gao. Solutions of the schrödinger equation for an attractive $1/r^6$ potential. *Phys. Rev. A*, 58(3):1728–1734, Sep 1998.
- [87] Masaaki Kitagawa, Katsunari Enomoto, Kentaro Kasa, Yoshiro Takahashi, Roman Ciuryło, Pascal Naidon, and Paul S. Julienne. Two-color photoassociation

- spectroscopy of ytterbium atoms and the precise determinations of s-wave scattering lengths. *Phys. Rev. A*, 77(1):012719, 2008.
- [88] J. C. Light, I. P. Hamilton, and J. V. Lill. Generalized discrete variable approximation in quantum mechanics. *The Journal of Chemical Physics*, 82(3):1400–1409, 1985.
- [89] Daniel T. Colbert and William H. Miller. A novel discrete variable representation for quantum mechanical reactive scattering via the s-matrix kohn method. *J. Chem. Phys.*, 96(3):1982–1991, 1992.
- [90] René Stock and Ivan H. Deutsch. Trap-induced resonances in controlled collisions of cesium atoms. *Phys. Rev. A*, 73:032701, March 2006.